

**Dissertation**

**Mathematical Modeling of the  
Shockless Explosion Combustion**

Phillip Berndt

im August 2016 eingereicht am

Fachbereich Mathematik und Informatik  
Freie Universität Berlin

zur Erlangung des Grades eines  
Doktors der Naturwissenschaften



**Erstgutachter & Betreuer:**

Prof. Dr.-Ing. Rupert Klein

**Zweitgutachter:**

Prof. Dr.-Ing. Christian Oliver Paschereit

**Drittgutachter:**

Prof. Dr. rer. nat. Volker John

**Tag der Disputation:**

02. Dezember 2016



# Contents

<b>1. Introduction</b>	<b>1</b>
1.1. The Shockless Explosion Combustion . . . . .	4
1.2. The Reactive Euler Equations of Fluid Dynamics . . . . .	7
1.2.1. The One-Dimensional Reactive Euler Equations . . . . .	8
1.2.2. Ignition Delay Time and Excitation Time . . . . .	11
1.2.3. Lagrangian Picture . . . . .	13
1.2.4. Quasi One-Dimensional Flow . . . . .	16
<b>2. Fuel Requirements and Blend Selection</b>	<b>19</b>
2.1. Model Reduction for SEC Fuels . . . . .	20
2.2. Model for Idealized SEC Fuels . . . . .	24
2.2.1. Single-Stage Model . . . . .	25
2.2.2. Two-Stage Extension . . . . .	27
2.3. Fuel Selection for the Atmospheric SEC Test Rig . . . . .	29
2.4. Numerical Methods for the Simulation of Chemical Kinetics . . . . .	32
2.5. Intermediate Conclusion . . . . .	35
<b>3. Numerical Methods for Multi-Species Gaseous Flow</b>	<b>37</b>
3.1. Solution of the Riemann Problem for Ideal Gases . . . . .	38
3.1.1. Linearization of the Equations . . . . .	38
3.1.2. Primitive Form of the Equations . . . . .	39
3.1.3. Riemann Invariants . . . . .	40
3.1.4. Solution Strategy . . . . .	42
3.2. The HLLE Solver in Multi-Species Simulations . . . . .	43
3.2.1. Positivity . . . . .	44
3.2.2. Pressure Oscillations at Contact Discontinuities . . . . .	46
3.2.3. A Note on Larroutrou's Positivity Correction . . . . .	49
3.3. Extension of the HLLEM Solver to Ideal Gases . . . . .	50
3.3.1. HLLEM for the Single-Species Case . . . . .	52
3.3.2. Reusing the Perfect Gas HLLEM Solver . . . . .	53
3.4. The Complete SEC Solver . . . . .	54
3.4.1. Higher Order Reconstruction . . . . .	54
3.4.2. Operator Splitting . . . . .	55
3.4.3. Program Flow . . . . .	57
3.5. Validation . . . . .	58
3.5.1. Shock Tube . . . . .	58
3.5.2. Moving Contact Wave . . . . .	59

3.5.3. Advection of Smooth Data . . . . .	60
3.5.4. Vacuum Test Case . . . . .	61
3.5.5. Acoustic Test Case . . . . .	63
3.5.6. Laval Nozzle Flow . . . . .	64
3.5.7. ZND Detonations . . . . .	66
3.6. Intermediate Conclusion . . . . .	70
<b>4. Multi-Cycle Simulation of the Shockless Explosion Combustion</b>	<b>71</b>
4.1. Numerical Setup . . . . .	71
4.1.1. Boundary Conditions . . . . .	71
4.1.2. Fuel Curve Determination . . . . .	72
4.2. Results . . . . .	75
4.2.1. Atmospheric Single-Shot Ignition . . . . .	75
4.2.2. Multi-Cycle Simulation with the Single-Stage Ideal Fuel Model .	77
4.2.3. Multi-Cycle Simulation with the Two-Stage Ideal Fuel Model . .	86
4.2.4. Efficiency Limits for the Upstream Boundary Condition . . . . .	89
4.2.5. Multi-Cycle Simulation with Real Fuels . . . . .	89
4.2.6. Axial Variations of the Tube Diameter . . . . .	94
4.2.7. Fuel Injection at Multiple Axial Positions . . . . .	95
4.2.8. Multi-Dimensional Multi-Cycle Simulation . . . . .	97
4.3. Intermediate Conclusion . . . . .	99
<b>5. Concluding Remarks</b>	<b>101</b>
<b>A. Overview Over Theoretical Prerequisites</b>	<b>105</b>
A.1. Thermodynamics . . . . .	105
A.2. Finite Volume Methods . . . . .	108
<b>B. Code Documentation</b>	<b>111</b>
B.1. High-Level Usage . . . . .	111
B.2. Detailed Program Flow and Advanced Features . . . . .	112
B.2.1. MEX Interface to the Kinetics Solver . . . . .	115
B.3. PyFlamemaster Interface to the Kinetics Solver . . . . .	115
B.4. Technical Background . . . . .	116
B.4.1. Closures in MATLAB . . . . .	116
B.4.2. MPI Interface to MATLAB . . . . .	117
B.4.3. MEX Kinetics Interface . . . . .	118
<b>List of Acronyms</b>	<b>121</b>
<b>Bibliography</b>	<b>123</b>

# 1. Introduction

The fast technological and industrial development of the last decades contributes to ever increasing living standards, but it also results in an increasing energy demand. Since the early 1980s, the world total energy production has nearly doubled to  $5 \cdot 10^{20}$  J in 2012, with an increasing trend [4]. Simultaneously, climate change and peak oil raised awareness for environmental consequences of wasteful use of inefficient energy sources. Political activists call for a shift towards renewable, efficient and economical means of transportation and power generation.

A specific challenge in electrical power generation is the variable demand: In Germany, there currently is a base load of about 45 GW, with peaks going up to as much as 80 GW [32]. With some renewable energy sources, especially wind turbines, in addition, there is high volatility in the supply. It is hence necessary to have power sources that may be quickly en- and disabled to cover peak-demands. Among the conventional technologies, gas turbines play an important role in this regard: They have comparatively low investment costs, low emissions, may be powered up and down within minutes, and allow the use of various fuels. In particular, they admit the use of renewable fuel sources.

The concept of a gas turbine dates back to 1791 [7], but it was not until 1939 that the available technology allowed economical use on an industrial scale [42, 57]. Steady advancements in technology have since increased the efficiency of gas turbine systems to around 40% for single cycle application. It is generally believed nowadays that to obtain large further increments in efficiency, a conceptual change is required.

The basic principle of a traditional gas turbine is as follows: A compressor, that is, an array of fan-like airfoils, increases the pressure of air flowing in by reducing its volume. Fuel is then injected into the air and a stationary flame is established. The hot exhausts expand through, and thereby drive, a turbine, which is another array of airfoils. Turbine and compressor are connected by a shaft, so the turbine powers the compressor. By furthermore attaching, e.g., a generator to the shaft, the remainder of the released energy can be utilized. The system may be modeled and planned as being in steady-state, significantly simplifying the design process. Transient behaviour is then considered off-design, and one tries to suppress it.

Researchers from Technische Universität Berlin, Freie Universität Berlin and RWTH Aachen jointly incorporated CRC 1029, funded by the German Research Foundation (DFG), in an effort to give up on this design pattern, and instead harness non-steady characteristics to achieve a large efficiency boost. Among others, alternative, non-steady thermodynamic cycles are under investigation.

One of them is the Shockless Explosion Combustion (SEC). It offers an increased best-case efficiency, but comes at the cost of a much more fragile process. It has high demands on accuracy in terms of when and how much fuel to inject into the burner, and even if

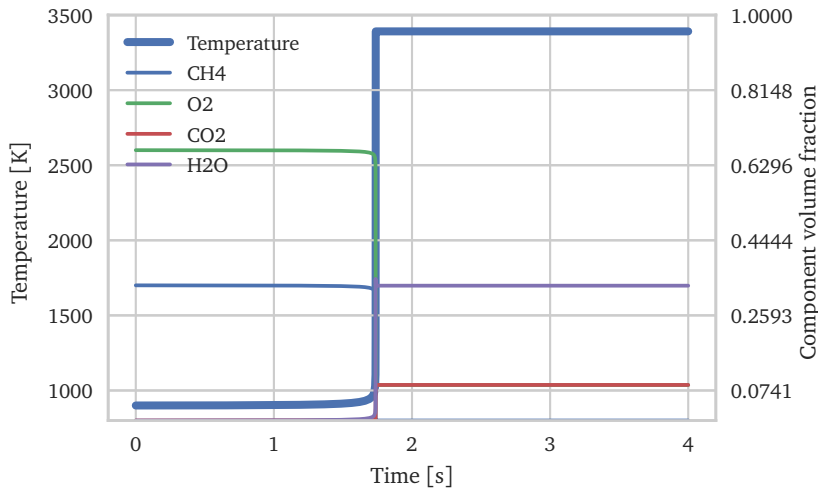


Figure 1.0.1.: Time series showing the auto-ignition of a stoichiometric methane/oxygen mixture in atmospheric pressure.

technologically these demands may be fulfilled, it is expected to require feedback control to remain operational. Subproject A03 has been concerned with the investigation of the process. The first phase of the project had two distinct foci: The qualification and quantification of the accuracy demands, and the study of means to meet them. The latter has been investigated at Technische Universität Berlin in C. Oliver Paschereit's group by Bernhard Bobusch, and later Thoralf Reichel. The research yielded promising solutions to a series of technological challenges. In particular, methods for accurate, efficient and fast mixing have been investigated. Bernhard Bobusch's dissertation [15] is centered around this part of the project. The former focus was pursued by means of a theoretical and numerical investigation of the process at Freie Universität Berlin, in Rupert Klein's group, by the present thesis's author.

A working SEC involves gas dynamics of combustible gases at temperatures close to their *auto-ignition temperature*: The chemical reactions driving combustions have reaction rates that increase with temperature and simultaneously raise temperature themselves as they progress. This makes combustion an exponential-like process, where for low temperatures, essentially no reaction takes place, for high temperatures, reactions progress very fast, and for intermediate temperatures, the reaction progresses but takes some time to reach the point where rapid progression may be observed. This point is called *ignition*, and for initial temperatures within this intermediate range, one speaks of auto-ignition. As an example, fig. 1.0.1 shows the auto-ignition of methane (CH<sub>4</sub>).

From an applied mathematician's perspective, the simulation of such flows is an interesting challenge: Within a gas that is close to auto-ignition, local errors in temperature can lead to premature, numerical ignition when they have a positive sign, or prevent ignition otherwise. Upon auto-ignition, the chemical reaction progresses sufficiently fast

---

for steep spatial gradients in temperature and pressure to appear in the model equations, a system of partial differential equations. These gradients are usually too large for numerical simulations with a reasonable grid resolution to handle. In a commonly used approximation to the underlying *Navier-Stokes equations*, namely the *Euler equations*, the gradients can even analytically evolve into discontinuities. In numerical mathematics, *shock-capturing methods* are a robust means to deal with this situation. These methods are designed to correctly handle the (near-)discontinuous case even with under-resolved grids. They introduce some amount of numerical diffusion that smoothens the discontinuities. If this artificial diffusion process mixes different gases, temperature does not remain constant in general, which is in conflict with the requirement to avoid temperature errors. A compromise must hence be tailored for simulations of the process.

From an engineering perspective, it is not less of a challenge to work with highly reactive flows. If small local errors cause problems in simulations, then small inaccuracies in measurement or control do as well cause problems in the real process. In contrast to a numerical simulation, which may be repeated over using the exact same conditions and where the entire system's state is known at each instant, experimentalists only have discrete measurements of some variables at hand, and cannot usually reproduce an experiment with the *exact* same conditions. It is hence mandatory to have a good theoretical understanding of the process.

During the work on the project, a simulation for qualitative investigation of SEC processes has been developed. A focus of the work has been to make the simulation sufficiently robust to allow it to be used by users without deep mathematical knowledge about the limitations of numerical simulations, and still produce reasonable results — it already is in active use by several projects investigating the SEC today. This required the extension and adaptation of existing numerical methods to a suitable thermodynamic representation of reactive flows and a discussion of the numerical issue introduced above. To allow to use the tool to make general statements on the process, a model for generic SEC-suitable fuels has been developed. The simulation and chemistry model have then been used to estimate requirements on real fuels and to suggest a charging strategy for the process.

This thesis aims to present all of these results. Due to the interdisciplinary nature of the project, it deals with many different areas, and it is not expected that readers have the same level of knowledge in all of them. Short, sometimes simplifying introductions will hence be given. They will hopefully suffice to follow the line of argumentation at all times. For in-depth introductions, references to introductory literature will be provided.

Structurally, the thesis is composed as follows: The second chapter is concerned with fuel choices and modeling, which thematically ranges from the engineering field of reaction kinetics to mathematical modeling. In the third chapter, numerical methods for highly reactive flows are developed. The fourth chapter applies the preceding results to obtain numerical results on the SEC, which thematically is again an engineering-oriented contribution. In the following, this chapter will introduce the SEC and the various forms of the equation system used to describe it.

## 1.1. The Shockless Explosion Combustion

The traditional working principle of a gas turbine has been laid out above. In theoretical investigations, one approximates the system by idealized *thermodynamic power cycles*: They represent the process of converting heat into useful work by a closed path in the phase space of the system, with the path being composed of actions that are easy to theoretically grasp. The phase space in thermodynamics stems from the *fundamental relation*

$$dE = T dS - p dV, \quad (1.1.1)$$

where  $E$  is the *internal energy* of the system,  $T$  is temperature,  $S$  entropy,  $p$  pressure and  $V$  the system's volume. The relation naturally arises in statistical physics, see, e.g., [49], or appendix A.1 for a brief summary. The equation is integrable for  $E$ , that is,  $E$  is a scalar potential, and any of the two variables may be used to span the system's phase space. Here,  $p$  and  $V$  will be used.

The thermodynamic cycle associated with gas turbines is the *Joule cycle*. In the left half of fig. 1.1.1, the cycle is plotted in  $p/V$  coordinates. The cycle begins in the bottom left corner and moves clockwise: In the dimensionless coordinates used for the plot, the point  $(1, 1)$  marks atmospheric conditions upon the start of the process. Idealized compression is an *isentropic* process, keeping entropy constant, because it is assumed that the compression is reversible. Under certain restrictions, lines of constant entropy are lines with  $pV^\gamma = \text{const}$ , for some constant  $\gamma$ . A steadily burning flame is modeled as an *isobaric* process, keeping pressure constant, because it is assumed that energy that would raise pressure is released on a time scale slower than that of the acoustics which, in some sense, tries to equilibrate pressure by transporting the released energy away towards regions of lower pressure. Idealized expansion is isentropic as well. The cycle is closed by isobaric heat rejection, assuming that the atmosphere is a reservoir with constant pressure. The area enclosed by the curve is the energy released by the power cycle. If one could replace the isobaric energy release of a steady flame with an *isochoric* process, one taking place at constant volume — as is the case in the right half of fig. 1.1.1 — then the amount of energy that is released increases. This observation motivates the SEC: It aims to achieve approximate Constant Volume Combustion (CVC) within a gas turbine.

The straightforward way to achieve constant volume combustion is to constrain the available volume by physical walls, as is the case in (idealized) internal combustion engines. In an open system such as a gas turbine, this is not an option. The alternative is to speed up the combustion: Above, it has been argued that a steady flame may be modeled as an isobaric process, because the time scale of energy release is slow compared to the acoustic time scale of energy transport. If energy is released on a comparable or faster time scale, then the pressure rises despite there being a volume for the gas to expand into, and in the limit of instantaneous energy release, the combustion process becomes isochoric.

An obvious limiting factor for the rate at which energy can be released is availability of combustible fuel/air mixture. By preparing a volume of premixed fuel/air, into

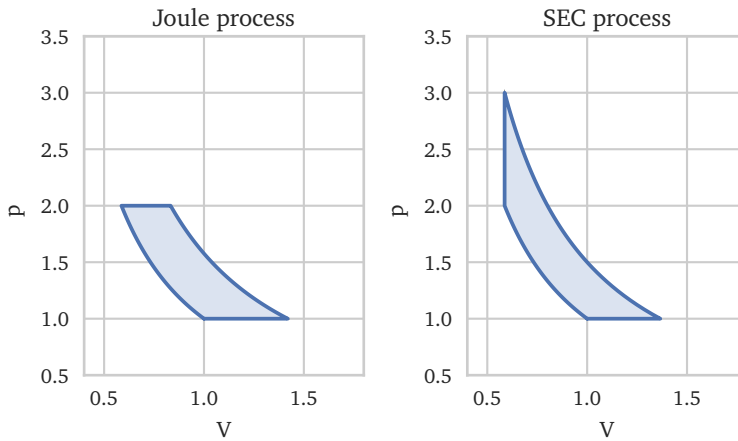


Figure 1.1.1.: Non-dimensional pV-diagrams for the Joule cycle of a traditional gas turbine and for the SEC, with the same fuel releasing  $\Delta H = 1$  in a perfect gas with  $\gamma = 1.3$ . The enclosed areas are  $\Delta E = 0.33$  for the Joule cycle and  $\Delta E = 0.39$  for the SEC.

which a combustion front can freely propagate, this limitation can be mitigated. Within such a mixture, various physical processes may govern the propagation of combustion fronts. The most common one can be observed in a *laminar flame*, where convection, especially thermal diffusion and diffusion of reactive, intermediate *radical* species from the reaction zone into fresh fuel/air mixture are locally responsible for the propagation of the flame (see, e.g., [78]). Combustion processes governed by convection are called *deflagrations*. Molecular diffusion is far too slow for the combustion to reach the pressure rising regime. In *turbulent flames*, turbulent mixing speeds up the process. It especially wrinkles and enlarges the flame surface area, resulting in faster propagation. As long as the flame propagates into the unburnt mixture at a subsonic velocity, energy released in the combustion is still transported away quickly and pressure cannot significantly rise. If propagation is sonic, however, pressure accumulates at the tip of the flame. Pressure waves raise temperature, and if the leading wave is strong enough, then the unburnt mixture no longer ignites due to heat transfer but by auto-ignition due to this pressure wave. The process is then called a *detonation*. Energy released from the reaction serves to sustain the pressure wave's strength. The leading shock wave has a pressure that is much higher than the final pressure of a CVC, and the final pressure after the combustion took place is still very high. A detonation may in this sense be regarded as approximate CVC. In the form of the Pulse Detonation Combustion (PDC) (see, e.g., [64]) it is also under investigation in CRC 1029. The PDC has two major drawbacks: The strong shock wave is undesired. For one, it puts high strain on the materials, for the other, it is associated with much kinetic energy, and it is not clear how all of it may be harnessed to drive the turbine. The other drawback is that the strong pressure wave must be created somehow. This happens through flame acceleration, which in this context is called Deflagration to Deto-

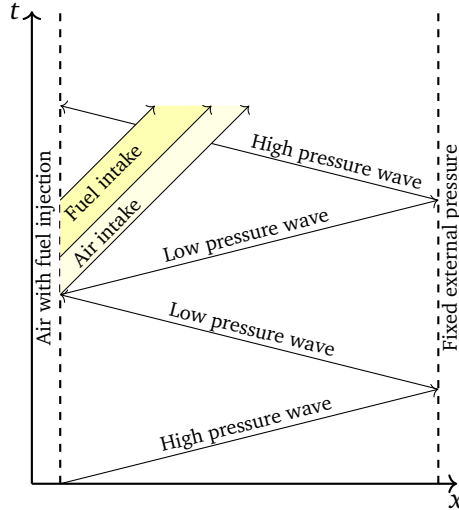


Figure 1.1.2.: Concept of the SEC process. One full cycle is shown with time in vertical direction, starting with a homogeneous ignition of the previous charge.

nation Transition (DDT). The part of the volume that is used for the DDT is combusted with lowered efficiency.

It is possible to have a high propagation velocity and still no leading shock wave: The mixture must be set up such that an “ignition wave” propagates through it faster than the shock preceding a detonation would. Ignition then takes place due to this wave, and any pressure emanating from progressing reactions can only progress into other ignited parts, but never into completely unburnt fuel. Combustion processes driven by such an ignition wave and maintaining a certain one-dimensional structure are called *weak detonations*. They generally require carefully designed experiments and do not (usually) occur in nature. One way to obtain a weak detonation is to set up an ignitable mixture in a tube that is transparent to laser light. The laser must be strong enough to ignite the mixture and set up such that the beam is guided through the mixture with appropriate speed. Rather than to induce ignition by external means, a mixture may also be set up such that it auto-ignites. A spatial gradient in the remaining time until auto-ignition then generates an ignition wave. The process then approximates a CVC. The limit case of an infinitely fast ignition wave is called a *thermal explosion*, and is a true CVC; *i.e.*, the smaller the gradient is, the better the approximation of a CVC.

The Shockless Explosion Combustion is based on this combustion concept. It incorporates it into a gas turbine by combining it with an innovative recharging concept: Pressure waves leaving the combustion tube are partially reflected at the open end. Woodwind instruments work on the same principle: Pressure waves are partially reflected, and form a standing wave in the instrument. The player supplies new energy to the wave by blowing the instrument, and energy leaves the system through the audible part of the wave that is not reflected. The reflection of a pressure wave from an open end is a low-pressure wave. Hence, in the SEC, when a pressure wave generated by a pressure-rising

combustion leaves the combustion tube towards a turbine plenum, its reflection creates a pressure gradient that sucks in fresh air that flushes exhausts from the pipe. Fuel is injected into this air to create a stratification which leads to approximately homogeneous, pressure-rising combustion. This creates another pressure wave, and the cycle repeats. Figure 1.1.2 schematically shows a full cycle of a SEC.

Ideally, the combustion should take place in resonance with the residual pressure waves. Their strength is then maximized. In thermoacoustics, the *Rijke tube* [62] is an example of a device with a related working principle.

## 1.2. The Reactive Euler Equations of Fluid Dynamics

The mathematical description of fluid dynamics stems from physical conservation principles: Consider a fixed control volume  $V$  containing a certain amount of matter, represented by its density  $\rho$ . In classical physics, mass cannot be created or destroyed, it is a conserved quantity. Changes to the total mass contained in the volume must hence stem from flux of mass through the boundaries:

$$\int_V \rho \, dx \Big|_{t_0}^{t_1} + \int_{t_0}^{t_1} \int_{\partial V} \rho u \cdot \nu \, d\omega = 0, \quad (1.2.1)$$

where  $u$  is the velocity field and  $\nu$  the outward facing surface normal. For sufficiently smooth data, the divergence theorem and a variational argument allow to rewrite this as a differential equation:

$$\frac{\partial \rho}{\partial t} + \nabla \cdot (\rho u) = 0. \quad (1.2.2)$$

This equation is the *continuity equation*. Equations of this form are said to be in *conservation form*, because they can be recast in integral form, and admit special numerical treatment that will be introduced below. The continuity equation holds for any quantity that is passively advected with the flow, such as dye in water, as well. Energy and momentum are only conserved up to change due to forces. Inclusion of pressure  $p$  and viscous stress forces leads, using the same transformations, to the *Navier-Stokes equation*

$$\frac{\partial \rho u}{\partial t} + \nabla \cdot (\rho u \otimes u + p \text{Id}) = \nabla \cdot \mathbb{S}(\mu, \nabla u), \quad (1.2.3)$$

where  $\otimes$  is the tensor product,  $\text{Id}$  the identity tensor, and  $\mathbb{S}$  a tensor representing the viscous forces that depends on velocity  $u$  and dynamic viscosity  $\mu$ . For energy, the corresponding formula is

$$\frac{\partial \rho E}{\partial t} + \nabla \cdot (u(\rho E + p)) = \nabla \cdot (\mathbb{S}(\mu, \nabla u)u), \quad (1.2.4)$$

except for a heat conduction term that has been left out for the sake of simplicity of this introduction. There are several important observations to make regarding these equations:

If pressure and density are constant, then the Navier-Stokes equation transports velocity with a speed that corresponds to the velocity field's value. Regions where velocity is large are transported faster than slow ones, further increasing velocity as high velocity regions merge with low velocity ones. A model equation for this phenomenon is *Burger's equation*,

$$\frac{\partial u}{\partial t} + \frac{\partial}{\partial x} \left( \frac{1}{2} u^2 \right) = d \frac{\partial^2 u}{\partial x^2}. \quad (1.2.5)$$

See, e.g., [53] for details. It is the simplest example of a system admitting *shock wave* formation: If the viscous term (containing second derivatives of  $u$ ) vanishes (*i.e.*,  $d = 0$ ), velocity gradients may steepen until a discontinuity arises. A meaningful solution for the differential equation does at this point no longer exist. To make sense of this, note that the natural formulation of the system is the integral equation, which continues to hold even with discontinuities in the solution. The theorems invoked in the transformation to a differential equation, however, no longer do. It is in this case necessary to use the integral formulation to obtain a solution. Interestingly, if  $d > 0$ , the viscous term prevents the velocity gradient from becoming infinite. In fact, the *Hopf-Cole transformation* allows to show that the equation is then equivalent to a linear heat equation, with solutions that are formally  $C^\infty(\mathbb{R})$  for all positive times. While this means that solutions' gradients remain finite, it does not prevent them from becoming very large in small spatial regions. If this happens, numerical solutions may still *appear* to be discontinuous if the grid resolution is too coarse to properly resolve them, and one must still revert to the integral laws to ensure that they are handled correctly.

For gases, the viscosity  $\mu$  often is very small. The *Reynolds number*

$$\text{Re} = \frac{\rho \ell u}{\mu} \quad (1.2.6)$$

does for a given domain with characteristic length  $\ell$  give the relative importance of inertial forces compared to viscous forces. In the context of turbulent combustion, it is mostly very large. It is hence customary to perform an inviscid approximation and remove the viscous term from the equations. The resulting set of equations are the *Euler equations*. From the analogy to Burger's equation, it should be clear that the equations admit shocks and discontinuous solutions. For their investigation, the integral formulation hence plays an important role.

For more detail on the derivation of the equations, see [48, 54].

### 1.2.1. The One-Dimensional Reactive Euler Equations

By augmenting the equations with transport equations, like eq. (1.2.2), for different species, and source terms that describe how chemical reactions transform the species into another, the equations become the *reactive Euler equations*. The exact formulation of the source terms will be given below; for now, they are denoted as  $\dot{Y}_{\text{chem}}$ . Throughout most of this thesis, a one-dimensional system will be regarded, under the assumption that the SEC is realized in a small-diameter duct and flow is cylindrically symmetric. In a

single spatial dimension, the augmented version of equations (1.2.2), (1.2.3) and (1.2.4) with vanishing viscosity is given by the following system:

$$\frac{\partial}{\partial t} \begin{pmatrix} \rho \\ \rho u \\ \rho E \\ \rho Y \end{pmatrix} + \frac{\partial}{\partial x} \begin{pmatrix} \rho u \\ \rho u^2 + p \\ u(\rho E + p) \\ \rho Y u \end{pmatrix} = \begin{pmatrix} 0 \\ 0 \\ 0 \\ \rho \dot{Y}_{\text{chem}} \end{pmatrix}. \quad (1.2.7)$$

As an abbreviation, the *state vector* following the time derivative operator will be denoted by  $q$ , and the *flux function* following the spatial derivative by  $f(q)$ . This system is closed by an Equation of State (EOS). Here, the ideal gas law is considered,

$$p = \rho \frac{\hat{R}}{M} T = \rho R T, \quad (1.2.8)$$

$$\rho E = \frac{1}{2} \rho u^2 + \rho e, \quad (1.2.9)$$

$$e = \int_{T_0}^T c_v(\tau, Y) d\tau + e_0(Y). \quad (1.2.10)$$

As before,  $\rho$  is mass density,  $u$  velocity,  $e$  internal and  $E$  total specific energy.  $Y$  is a vector of mass fractions with non-negative entries that sum up to one, *i.e.*, the last dimension in eq. (1.2.7) symbolically stands for arbitrary many dimensions,  $p$  is pressure,  $T$  temperature,  $c_v$  specific heat-capacity at constant volume,  $M$  the mean molar mass of the mixture and  $\hat{R}$  the ideal gas constant,  $\hat{R} = 8.314 \text{ J/mol}\cdot\text{K}$ . The specific gas constant  $\hat{R}/M$  will be denoted  $R$ . Where needed, the vector of the species' individual gas constants will be denoted  $\vec{R}$ , and respectively for other mixture averaged quantities, vector arrows will be added if the vector of the individual species' values is meant. Values for  $c_v$  and  $M$  are available in literature. Since all entries of  $Y$  add up to unity, the last one is usually not written explicitly in numerical calculations, but calculated from the others.  $e_0$  is the energy corresponding to *standard heat of formation* at  $T = T_0$ , the energy contained in the chemical bonds within the molecules, and is also available from literature. It is numerically advantageous to take the viewpoint that  $e_0$  is zero and that instead chemical reactions release or consume energy, because the formulation then ensures that species and the energy from their heat of formation cannot "move" separately.  $e_0$  will hence be omitted in discussions of the formula below, and instead, the energy equation obtains a source term representing changes due to the species' concentrations changing as reactions progress.<sup>1</sup>

The special case of constant  $c_v$  allows to derive the simplified expression

$$e = c_v T = \frac{p}{(\gamma - 1) \cdot \rho} \quad (1.2.11)$$

---

<sup>1</sup>Note that with this choice the energy  $\rho E$  is no longer the total energy of the system, but the *sensible* energy. While the total energy is a conserved quantity, the sensible energy is not. This poses a problem for finite volume discretizations, which require a conservative formulation of the equation system to ensure correct signal propagation velocities. However, the discretization of the system in chapter 3 will treat gas dynamics and the chemical source terms separately using operator splitting, and the gas dynamics part of the equation conserves the sensible energy as well as the total energy. Thus, the theory still applies.

with *isentropic exponent*  $\gamma = c_p/c_v$ , where  $c_p$  is the specific heat-capacity at constant pressure. Gases obeying this law are denoted (*calorically*) *perfect gases* here. It should be noted that some authors use a different nomenclature.

If not constant,  $c_v$  is usually given per species by a set of two fourth order polynomials interpolated from measurements, each of them valid within a specified range of temperatures. The mixture's heat capacity is then obtained by mass fraction weighted averaging. This parametrization was introduced by NASA, and the obtained polynomials are known as *NASA polynomials*.

The kinetical source term  $\dot{Y}_{\text{chem}}$  must be sufficiently smooth and chosen such that the constraint that the entries of  $Y$  add up to unity is not violated. A detailed introduction to chemical kinetics is given in [16]. Usually,  $\dot{Y}_{\text{chem}}$  is given by a system of reactions and associated reaction rates, *e.g.*,



$$r = 1.8 \cdot 10^{13} \exp\left(-\frac{17614 \text{K}}{T}\right) [\text{H}_2][\text{O}_2]^{0.5}, \quad (1.2.13)$$

which is a *global reaction* for hydrogen combustion [55]. This system contains three species, so  $Y$  has three components. If one chooses the order  $\text{H}_2$ ,  $\text{O}_2$  and  $\text{H}_2\text{O}$ , then

$$\dot{Y}_{\text{chem}} = r \cdot \begin{pmatrix} -2 M_{\text{H}_2} \\ -1 M_{\text{O}_2} \\ 2 M_{\text{H}_2\text{O}} \end{pmatrix}, \quad (1.2.14)$$

because the reaction produces two water molecules for each two molecules of hydrogen and single oxygen molecule that it consumes. The masses of the molecules are not important in this example, suffice it to say that  $\sum \dot{Y}_{\text{chem}} = 0$ . If more reactions are involved, the change rates are calculated from the sums of similar expressions. The prefactor in  $r$  is called an *Arrhenius rate*, and generally expressed as

$$A \cdot T^B \cdot \exp\left(-\frac{E_A}{RT}\right). \quad (1.2.15)$$

A simple interpretation of the rate law (1.2.13) is that it represents the probability that two molecules with sufficient energy to react meet:  $\exp(-E/RT)$  is the *Maxwell-Boltzmann distribution*, the probability density for particles to have energy  $E$  in a system with temperature  $T$ . The factor  $A$  and exponent  $B$  are empiric. More general reactions and rate laws exist. One case that will reoccur later are *third body reactions* in which two molecules can associate by passing some energy to a third molecule. This process can be pressure dependent, in which case the reaction rate equation will depend on it as well.

The combination of thermodynamic data of the individual species and reaction rate equations forms a *reaction mechanism*.

### 1.2.2. Ignition Delay Time and Excitation Time

For the SEC process, two parameters of the chemical kinetics that appear in certain asymptotic expansions are of special interest. Consider a combustion process described by a single reaction of the form as in eq. (1.2.15) with  $B = 0$ , converting fuel F to product P, with the gas being described by the perfect gas law with fixed  $\gamma$ . Assume that the difference in enthalpies of formation of both species is given by  $\Delta Q$ , that is, that the reaction releases this amount of energy per reacted amount of fuel. The dynamics of the process is then described by the equation system

$$\dot{Y} = -A \cdot \exp\left(-\frac{E_A}{RT}\right) Y, \quad (1.2.16)$$

$$T = T_0 + \frac{\Delta Q}{c_v} (Y_0 - Y). \quad (1.2.17)$$

For the following derivations, it is convenient to write the system as

$$\dot{Y} = -\tilde{A} \cdot \exp\left(\frac{E_A}{R} \left(1 - \frac{T_i}{T}\right)\right) Y, \quad (1.2.18)$$

$$T = T_0 + \frac{\Delta Q}{c_v} (Y_0 - Y), \quad (1.2.19)$$

with  $\tilde{A}$  and  $T_i$  defined such that both forms are equivalent. The equation system may be expressed as a single equation for temperature:

$$\dot{T} = \frac{\Delta Q}{c_v} \left( \tilde{A} \cdot \exp\left(\frac{E_A}{R} \left(1 - \frac{T_i}{T}\right)\right) \left(Y_0 - \frac{c_v}{\Delta Q} (T - T_0)\right) \right). \quad (1.2.20)$$

The first parameter of interest is the *auto-ignition delay time*  $\tau$ . It has been introduced as the time until ignition in the introduction, see fig. 1.0.1: For large activation energies  $E$ , solutions of the equation remain essentially constant for long times and then rapidly increase in temperature upon ignition. A careful choice of parameters allows to construct an asymptotic expansion that breaks down upon ignition, allowing to extract a formula for the auto-ignition delay time. To this end, introduce

$$\varepsilon = \frac{RT_0}{E_A T_i} \quad (1.2.21)$$

as a small dimensionless parameter and consider solutions of the form

$$T = T_0 (1 + \varepsilon z), \quad (1.2.22)$$

that is, solutions that remain close to the initial temperature  $T_0$ . By inserting this ansatz into the exponential factor in eq. (1.2.20) and performing a Taylor expansion of the function's argument in  $\varepsilon$ , one obtains

$$\exp\left(\frac{E_A}{R} \left(1 - \frac{T_i}{T}\right)\right) \approx \exp\left(\frac{E_A}{R} \left(1 - \frac{T_i}{T_0}\right)\right) \exp z, \quad (1.2.23)$$

and

$$T_0 \varepsilon \dot{z} = \frac{\Delta Q}{c_v} \tilde{A} \cdot \exp\left(\frac{E_A}{R}\left(1 - \frac{T_i}{T_0}\right)\right) \left(Y_0 - \frac{c_v}{\Delta Q} T_0 \varepsilon z\right) \exp z \quad (1.2.24)$$

for the time evolution of  $z$ . This equation may be written as

$$\dot{z} = \frac{\Delta Q}{c_v T_0} \tilde{A} \cdot \exp\left(\frac{1}{\varepsilon}\left(\frac{T_0}{T_i} - 1\right)\right) \left(\frac{Y_0}{\varepsilon} - \frac{c_v}{\Delta Q} T_0 z\right) \exp z. \quad (1.2.25)$$

Define another variable, rescaled in time,

$$\tilde{z}(\tau) = z \left( \varepsilon \exp\left(-\frac{1}{\varepsilon}\left(\frac{T_0}{T_i} - 1\right)\right) \tau \right). \quad (1.2.26)$$

For this variable,

$$\frac{\partial \tilde{z}}{\partial \tau} = \frac{\Delta Q}{c_v T_0} \tilde{A} \left( Y_0 - \varepsilon \frac{c_v}{\Delta Q} T_0 z \right) \exp z. \quad (1.2.27)$$

For  $\varepsilon \rightarrow 0$ , the linear term vanishes and, after back-substitution, the equation becomes of the form

$$\dot{z} = \underbrace{\left( \frac{E_A T_i Y_0 \tilde{A} \Delta Q}{R c_v T_0^2} \exp\left(\frac{E_A}{R}\left(1 - \frac{T_i}{T_0}\right)\right) \right)}_{=1/\tau} \exp z \quad (1.2.28)$$

with solution

$$z = \log\left(-\frac{\tau}{t - \tau}\right). \quad (1.2.29)$$

This solution has a singularity in  $t = \tau$ , defining the ignition delay time.

The second parameter of importance is the *excitation time*  $\mathcal{E}$ : It indicates the time scale on which energy is released after the ignition delay time has passed. In the SEC, it gives a measure for acceptable inaccuracies in auto-ignition delay time in a fuel stratification: If the volume with the fuel stratification ignites too early in a single hotspot, then a long excitation time gives the neighboring fuel parcels some time to auto-ignite as well, while a short one might result in a deflagrative or (strongly) detonative combustion. The right hand side of eq. (1.2.20) attains its maximum, and is in particular analytically solvable for this maximum:

$$\frac{\partial \dot{T}}{\partial T} = 0 \implies T = \frac{1}{2Rc_v} \left( -E_A T_i c_v \pm \sqrt{E_A T_i c_v (4\Delta Q R Y_0 + E_A T_i c_v + 4Rc_v)} \right). \quad (1.2.30)$$

The maximum is attained for the solution with positive sign in front of the square root. To first order, the time from ignition until the reaction reaches equilibrium is then given by the quotient of the total temperature increase and the maximal temperature derivative:

$$\begin{aligned} \mathcal{E} &= \frac{\Delta Q Y_0}{c_v} \frac{1}{\max \dot{T}} \\ &= \frac{2R\Delta Q \exp\left(\frac{E_A(-E_A T_i c_v - 2RT_i c_v + D)}{R(E_A T_i c_v - D)}\right)}{A(2R Y_0 \Delta Q + E_A T_i c_v + 2Rc_v - D)} \quad \text{with } D = \sqrt{E_A T_i c_v (4\Delta Q R Y_0 + E_A T_i c_v + 4Rc_v)}. \end{aligned} \quad (1.2.31)$$

The expression does not have much practical use, but in comparison to  $\tau$  serves to show that most times  $\mathcal{E} \ll \tau$ . It is only comparable to or larger than  $\tau$  for either small  $\Delta Q$  or small  $T_i$ . Fuels with large  $\mathcal{E}$  that admit larger inaccuracies must hence have more complex chemistry than may be described by a single, global reaction.

An alternative expression for excitation time may be derived by performing an asymptotic expansion as for the auto-ignition delay time, around the point where slightly less than half of the energy has been released, and solving the solution for a point where slightly more than half of the energy has been released. The method yields the same results for the influence of the parameters, and a comparably complex expression for  $\mathcal{E}$ .

For complex mechanisms, such asymptotic approaches do not work in general. Instead, definitions that admit numerical evaluation are required. Here, the following definitions are used:

**Auto-ignition delay time** The time at which the temperature time-derivative attains its maximal value.

**Excitation time** The time it takes for temperature to rise from

$$\left(\frac{1}{2} + \xi\right)T_0 + \left(\frac{1}{2} - \xi\right)T_\infty \quad (1.2.32)$$

to

$$\left(\frac{1}{2} - \xi\right)T_0 + \left(\frac{1}{2} + \xi\right)T_\infty, \quad (1.2.33)$$

with  $\xi = 0.35$ .

Both definitions are compatible with the ideas that yielded the two expressions (1.2.28) and (1.2.31).

### 1.2.3. Lagrangian Picture

Equation (1.2.7) is a representation of the Euler equations in the *Eulerian specification*, where the underlying conservation laws are integrated over a stationary control volume to derive the equations. It is sometimes useful to instead use control volumes that move with the fluid, because all fluid properties that are advected but not otherwise changed by the equations can then be represented exactly. This view on the fluid is called the *Lagrangian specification*. In chapter 3 it will be seen that numerical diffusion of different gases into one another creates numerical difficulties in the Eulerian equations. The Lagrangian formulation avoids them due to this property. Keeping track of particle positions however is cumbersome, especially as particles enter and leave the numerical domain. The specification is hence primarily of theoretical interest in the context of this thesis, and presented for completeness.

The *Reynolds transport theorem* describes how moving boundaries affect an integral. It enables the transition between both pictures. The derivation is presented for one dimension here, but holds in 3D space as well, see, e.g., [61, 77].

**Theorem 1.2.1** (Reynolds Transport Theorem). *For any material volume*

$$V(t) = [x_0(t), x_1(t)] \quad (1.2.34)$$

*and differentiable scalar field  $\Phi$*

$$\frac{d}{dt} \int_{x_0(t)}^{x_1(t)} \Phi \, dx = \int_{x_0(t)}^{x_1(t)} \left( \frac{\partial \Phi}{\partial t} + \frac{\partial(\Phi u)}{\partial x} \right) dx \quad (1.2.35)$$

*holds.*

*Proof.* Let

$$J = \frac{\partial x(t)}{\partial x(0)} \quad (1.2.36)$$

be the functional determinant of the transformation  $V(t) \rightarrow V(0)$ . Note that

$$\frac{dJ}{dt} = \frac{\partial u(t)}{\partial x(0)} = \frac{\partial u(t)}{\partial x(t)} \frac{\partial x(t)}{\partial x(0)} = J \frac{\partial u(t)}{\partial x(t)}, \quad (1.2.37)$$

with the convention that  $dx/dt = u$  denotes the velocity, as long as that transformation is sufficiently smooth.

In the following,  $V(t) \rightarrow V(0) \rightarrow V(t)$  is substituted to remove the time dependence from the integral boundaries. In the intermediate step the order of integral and time derivative can therefore be exchanged:

$$\frac{d}{dt} \int_{x_0(t)}^{x_1(t)} \Phi \, dx = \frac{d}{dt} \int_{x_0(0)}^{x_1(0)} \Phi J \, dx \quad (1.2.38)$$

$$= \int_{x_0(0)}^{x_1(0)} \left( \frac{d\Phi}{dt} J + \Phi J \frac{\partial u(t)}{\partial x(t)} \right) dx \quad (1.2.39)$$

$$= \int_{x_0(t)}^{x_1(t)} \left( \frac{d\Phi}{dt} + \Phi \frac{\partial u(t)}{\partial x(t)} \right) dx \quad (1.2.40)$$

$$= \int_{x_0(t)}^{x_1(t)} \left( \frac{\partial \Phi}{\partial t} + \frac{\partial(\Phi u)}{\partial x(t)} \right) dx. \quad (1.2.41)$$

In the last step, it has again been used that in  $\Phi(x(t), t)$ , the time derivative of  $x(t)$  is the velocity  $u$ . ■

By using the theorem, e.g., with the physical insight that mass is conserved, one finds that

$$0 = \int_{x_0}^{x_1} \rho \, dx = \int_{x_0}^{x_1} \left( \frac{\partial \rho}{\partial t} + \frac{\partial(\rho u)}{\partial x} \right) dx \quad (1.2.42)$$

holds for *material volumes*  $V(t) = [x_0(t), x_1(t)]$ , that is, volumes that move such that they contain the same particles at all times. Since apart from that,  $V$  is arbitrary, the integrand must vanish, giving the first equation from eq. (1.2.7):

$$\frac{\partial \rho}{\partial t} + \frac{\partial(\rho u)}{\partial x} = 0. \quad (1.2.43)$$

The insight that can be gained from this derivation is that this equation still holds if  $x$  depends on  $t$ , especially also if one chooses  $\frac{dx}{dt} = u$  with  $x(0) = \bar{x}$ , i.e., the Lagrangian specification. By this choice, the spatial partial derivative drops from the total differential of  $\rho$ ,

$$d\rho = \frac{\partial \rho}{\partial x} dx + \frac{\partial \rho}{\partial t} dt = \frac{\partial \rho}{\partial x} dx - \frac{\partial(\rho u)}{\partial x} dt = \frac{\partial \rho}{\partial x} (dx - u dt) - \rho \frac{\partial u}{\partial x} dt, \quad (1.2.44)$$

and the total time derivative simplifies to

$$\frac{d\rho}{dt} = -\rho \frac{\partial u}{\partial x}. \quad (1.2.45)$$

A variable transformation can be performed to replace the derivative for the unknown function  $x(t)$  with one for the initial condition  $\bar{x}$ . Denoting  $\rho$  at time  $t = 0$  by  $\bar{\rho}$ ,

$$\int_{x_0(0)}^{x_1(0)} \bar{\rho} d\bar{x} = \int_{x_0(t)}^{x_1(t)} \rho dx = \int_{x_0(0)}^{x_1(0)} \rho J d\bar{x}. \quad (1.2.46)$$

The left integral is the mass at time 0. The first equation relates this to the mass at time  $t$ , which must be equal, since  $[x_0, x_1]$  is a material volume and mass is conserved. Since the left and right integrals are taken over the same domain, with the same differential, and the material volume is again arbitrary,  $\bar{\rho}$  must be equal to  $\rho J$ .  $J$  is the partial derivative of a particle's position  $x$  for the initial position  $\bar{x}$ , hence

$$\rho dx = \bar{\rho} d\bar{x}. \quad (1.2.47)$$

Substitution into eq. (1.2.45) yields

$$\frac{d\rho}{dt} = -\frac{\rho^2}{\bar{\rho}_0} \frac{\partial u}{\partial \bar{x}}. \quad (1.2.48)$$

From here on,  $\bar{x}$  is then used as a coordinate that describes the fluid parcel that has been at position  $\bar{x}$  at time  $t = 0$ . By applying the same reasoning to conservation of momentum and energy, one gets to the equations

$$\frac{d\rho}{dt} + \frac{\rho^2}{\bar{\rho}_0} \frac{\partial u}{\partial \bar{x}} = 0, \quad (1.2.49)$$

$$\frac{du}{dt} + \frac{1}{\bar{\rho}_0} \frac{\partial p}{\partial \bar{x}} = 0, \quad (1.2.50)$$

$$\frac{dE}{dt} + \frac{1}{\bar{\rho}_0} \frac{\partial(pu)}{\partial \bar{x}} = 0. \quad (1.2.51)$$

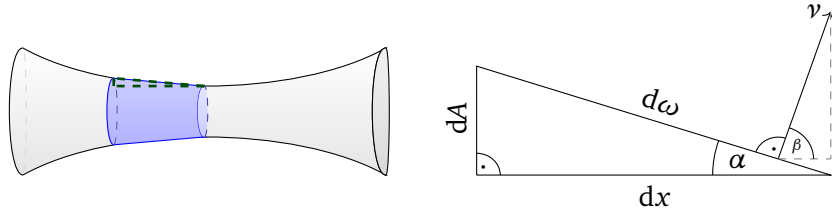


Figure 1.2.1.: Volume element for the derivation of the quasi one-dimensional equations.

The element is painted blue. The dashed triangle is enlarged on the right side. It shows that since  $\alpha = \pi/2 - \beta$ , the surface normal  $\nu$  and surface element  $d\omega$  relate to the area element  $dA$  via the equation  $dA = -\nu_x d\omega$ .

To get the second and third equation into conservation form, the substitution  $dh = \bar{\rho} dx$  must be applied to arrive at

$$\frac{d\rho}{dt} + \rho^2 \frac{\partial u}{\partial h} = 0, \quad (1.2.52)$$

$$\frac{du}{dt} + \frac{\partial p}{\partial h} = 0, \quad (1.2.53)$$

$$\frac{dE}{dt} + \frac{\partial(pu)}{\partial h} = 0. \quad (1.2.54)$$

To finally get the first equation into conservation form as well, note that

$$\frac{d}{dt} \frac{1}{\rho} = -\frac{1}{\rho^2} \frac{d\rho}{dt}. \quad (1.2.55)$$

Hence, replacing density  $\rho$  by the *specific volume*  $v = 1/\rho$  changes the first equation to the conservation equation

$$\frac{dv}{dt} - \frac{\partial u}{\partial h} = 0. \quad (1.2.56)$$

Since these equations are now in conservation form, a standard finite volume framework (see chapter 3) can be employed to solve them.

#### 1.2.4. Quasi One-Dimensional Flow

The one-dimensional equation eq. (1.2.7) models flow in a cylinder that is symmetric with respect to the axis. If the cylinder is replaced by a solid of revolution with a sufficiently smooth boundary curve, then the flow can still be approximated by a one-dimensional system. The following derivation is based on [76]; it is an iconic derivation, but easy to understand and conceptionally correct. See [66] for a more thorough disquisition.

In a solid of revolution along the  $x$  axis, if symmetry with respect to the axis is assumed, it suffices to restrict oneself to volume elements of the form

$$dV = A(x) dx \quad (1.2.57)$$

in the evaluation of integrals, where  $A(x)$  is the cross-sectional area. This expansion is used in the integral 3D balance equations, with surface normal  $\nu$ , surface element  $d\omega$ , and a control volume  $V$  that has the shape of the solid of revolution. For the mass equation,

$$0 = \frac{\partial}{\partial t} \int_V \rho \, dV + \int_{\partial V} \rho u \cdot \nu \, d\omega \quad (1.2.58)$$

$$= \frac{\partial}{\partial t} \int_V \rho A \, dx + \int_{\partial V} \rho u \cdot \nu \, d\omega \quad (1.2.59)$$

$$= \int_V \left( \frac{\partial}{\partial t} (\rho A) + \frac{\partial}{\partial x} (\rho u A) \right) dx \quad (1.2.60)$$

$$\implies \frac{\partial}{\partial t} (\rho A) + \frac{\partial}{\partial x} (\rho u A) = 0. \quad (1.2.61)$$

In the third step, the divergence theorem has been used in  $x$  direction; on the perpendicular volume boundary, *i.e.*, the walls,  $u$  vanishes in normal direction by the assumption of rigid wall boundary conditions. The derivation of the energy and species mass advection equations is analogous, and also yields the same equations as in eq. (1.2.7), but weighted by the cross sectional area. In the derivation of the momentum equation, the pressure source term does not vanish at the lateral surface. One is instead left with the equation

$$\int_V \left( \frac{\partial}{\partial t} (\rho u A) + \frac{\partial}{\partial x} (\rho u^2 A + Ap) \right) dx + \int_{\text{wall}} p \nu_x \, d\omega = 0. \quad (1.2.62)$$

Only the  $x$  component of  $\nu$  enters in the last integral because the equation concerns itself with the conservation of the  $x$  component of momentum. Application of the differential equality from fig. 1.2.1 allows to transform this to

$$\int_V \left( \frac{\partial}{\partial t} (\rho u A) + \frac{\partial}{\partial x} (\rho u^2 A + Ap) \right) dx - \int_V p \frac{dA}{dx} \, dx = 0, \quad (1.2.63)$$

which finally leads to the quasi one-dimensional reactive Euler equations:

$$\frac{\partial}{\partial t} \begin{pmatrix} \rho A \\ \rho Au \\ \rho AE \\ \rho AY \end{pmatrix}_t + \frac{\partial}{\partial x} \begin{pmatrix} \rho u A \\ \rho u^2 A + pA \\ uA(\rho E + p) \\ \rho u AY \end{pmatrix} = \begin{pmatrix} 0 \\ 0 \\ 0 \\ \rho A \dot{Y}_{\text{chem}} \end{pmatrix} + p \frac{\partial}{\partial x} \begin{pmatrix} 0 \\ A \\ 0 \\ 0 \end{pmatrix}. \quad (1.2.64)$$

With the exception of the new source term in the momentum equation, the system is structurally unchanged. This will be exploited later in the construction of the numerical solver for SEC calculations, as it allows to include support for axial variations in a program with very little effort.



## 2. Fuel Requirements and Blend Selection

The SEC relies on accurate control of the auto-ignition delay time: A volume of fuel and air must be stratified such that it combusts in a weak or developing detonation. The faster the detonation wave is, the better the approximation of a CVC. If large errors are present in a stratification, then ignition takes place in a local hotspot, resulting in a deflagrative combustion. For small errors, there is the possibility that combustion becomes strongly detonative. The preceding chapter introduced the idea of using a gradient in auto-ignition delay time in a stratification as a means to obtain a weak detonation. This gradient must be such that the point where ignition currently takes place moves faster through the stratification than pressure waves due to the energy release of the reaction do. If the gradient is too steep, then the propagation of the energy released in the combustion might couple with the propagation of the auto-ignition wave, resulting in a steepening pressure wave, until at some point, the local pressure is sufficient to drive a strong detonation. This mechanism for detonation initiation is called Shock Wave Amplification by Coherent Energy Release (SWACER) [5, 35, 52]. Both cases, gradients too steep and to shallow, lead to a loss of homogeneity.

Auto-ignition delay time is usually very sensitive *w.r.t.* mixture properties. *E.g.*, for stoichiometric Methane ( $\text{CH}_4$ ) in air at  $700^\circ \text{C}$  and 1 atm, ignition delay time changes by  $31 \text{ ms}/\text{K}$ , and by  $8.8 \text{ ms}$  per 1% deviation in equivalence ratio. Spatial gradients in a stratification that have an order of  $1 \text{ ms}/\text{m}$  suffice to produce the strong detonations that are to be avoided. Temperature must hence be known with high precision in a SEC. This is at odds with experimental reality, where controlling temperature in a multi-cycle combustion test rig to less than a few degrees Celsius is a challenging task. To ease the requirements on experimental accuracy, guest project A07 of CRC 1029<sup>1</sup> concerned itself with the development of a fuel that has only minimal dependence of auto-ignition delay time on temperature for at least a range of temperatures.

Their ansatz is based on the Negative Temperature Coefficient (NTC) behaviour of certain fuels: Whereas one would for fuels governed by the Arrhenius law (1.2.15) expect the auto-ignition delay time to shorten with increasing initial temperature, NTC fuels have a temperature range where it instead increases. By blending fuels with and without NTC behaviour, a mixture that has an auto-ignition delay time independent of initial temperature — at least inside the NTC region of the NTC fuel — can be created.

They eventually suggested to use a mixture of Dimethyl Ether (DME), dihydrogen ( $\text{H}_2$ ) and methane ( $\text{CH}_4$ ) as a gaseous fuel mixture, with equal amounts of each fuel as a rough first estimate [18]. Optimization of the ratio of the different compounds was then

---

<sup>1</sup>Prof. Pitsch, Institut für Technische Verbrennung, RWTH Aachen University

carried out on-site by the thesis's author, taking experimental constraints into account; the results will be presented in this chapter.

Another topic of interest is the continued reduction of their reaction mechanism: Ignition chemistry of the resulting fuels is complex, and involves a variety of intermediate species: While the overall temperature dependence of auto-ignition delay time is small, this effect is reached through a balance of many concurring reactions, each of which can have a strong temperature dependence. As will be explained in detail below, a sufficiently reduced mechanism with a small number of species that retains the (in-)dependence of auto-ignition delay time on temperature can therefore not be produced by standard, automated reduction techniques. Instead, detailed chemical kinetics must be used in simulations, or specialized mechanisms created. Both approaches have been pursued and will be presented in this chapter.

## 2.1. Model Reduction for SEC Fuels

The fuel project started its investigation with the reduced DME mechanism by [8], based on the comprehensive studies from [21, 31]. In [18], they extended this model to include hydrogen ( $H_2$ ) and methane ( $CH_4$ ) combustion, to a mechanism with initially 259 species. They then investigated manually some mixtures of said fuels in search of temperature regions where auto-ignition delay time, for stoichiometric mixtures at 1 bar, 10 bar, and 30 bar respectively, does not depend strongly on temperature. Once good candidates were found, the parameters were then fed into a simulation calculating the ignition delay time. In an automated optimization process, the species with the lowest impact on calculated ignition delay time were then successively removed from the mechanism until the relative error in the calculated auto-ignition delay times reached a threshold of 1 %. This yielded a smaller mechanism with 83 species. This mechanism was handed over to the author and has thereupon been further reduced.

First, in collaboration with Liming Cai from RWTH Aachen, the author removed more intermediate species that are not of importance for the NTC mechanism, but only play a role in the excitation regime of the reaction, where energy is released. This reduced the mechanism to 52 species.

The reason for the large number of species in the reduced mechanism lies in the physical mechanism enabling NTC behaviour: Figure 2.1.1 sketches the main reaction paths leading from DME to formaldehyde. In the graph, the DME descendants are drawn as skeletal formulas, with lines corresponding to bonds involving a carbon atom, and dots representing a missing hydrogen atom, thus a species with an unpaired valence electron, a *radical*. E.g., the third species down from the upper left corner is  $CH_3OCOO$ . The graph shows three distinct reaction pathways that the combustion can take. The *low temperature* branch is the overall *fastest*, but the reaction branching into the *high temperature* branch is faster than the one branching into the low temperature one once its activation energy is reached. This establishes the NTC behaviour. Since three such branches exist and at least one intermediate species per high temperature branch is required to establish the “fast transition into branch, slow progress in branch” behaviour,

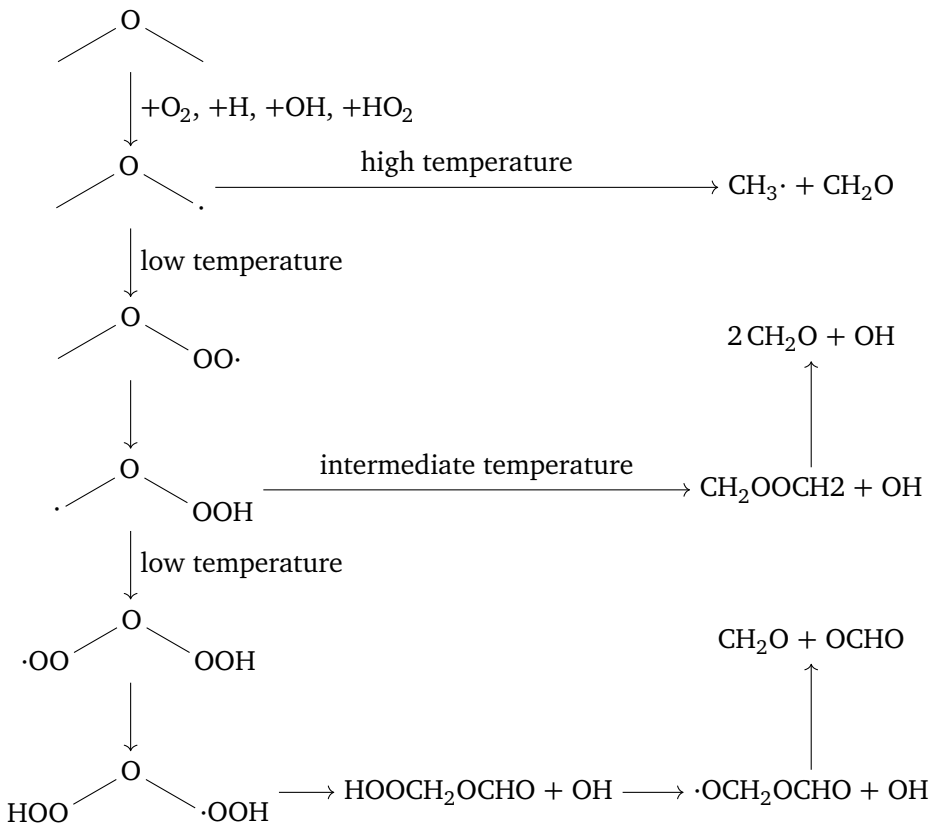


Figure 2.1.1.: Schematic reaction pathways of DME. The different paths activate at different temperatures, resulting in the NTC behaviour. Each path eventually produces formaldehyde ( $\text{CH}_2\text{O}$ ), which reacts further to  $\text{HCO} \rightarrow \text{CO} \rightarrow \text{CO}_2$  in reactions responsible for the primary heat release [21, 31].

## 2. Fuel Requirements and Blend Selection

---

Species	peak molar concentration	Species	peak molar concentration
$\text{CH}_3\text{OCH}_2\text{O}$	$1.149 \cdot 10^{-15}$	$\text{CH}^\dagger$	$3.523 \cdot 10^{-07}$
$\text{OCH}_2\text{OCHO}$	$3.070 \cdot 10^{-12}$	$\text{CH}_2\text{OH}^\dagger$	$5.930 \cdot 10^{-07}$
$\text{C}_2\text{H}_5\text{O}$	$9.573 \cdot 10^{-12}$	$\text{C}_2\text{H}_5^\dagger$	$7.603 \cdot 10^{-07}$
$\text{HOCH}_2\text{O}$	$1.093 \cdot 10^{-11}$	$\text{CH}_3\text{CO}_2^\dagger$	$1.184 \cdot 10^{-06}$
$\text{CH}_2\text{OCH}_2\text{O}_2\text{H}$	$3.919 \cdot 10^{-11}$	$\text{C}_2\text{H}_3^\dagger$	$1.228 \cdot 10^{-06}$
$\text{HO}_2\text{CH}_2\text{OCHO}$	$1.366 \cdot 10^{-10}$	$\text{T}-\text{CH}_2^\dagger$	$3.167 \cdot 10^{-06}$
$\text{CH}_3\text{OCH}_2\text{O}_2\text{H}^\dagger$	$1.646 \cdot 10^{-10}$	$\text{HCO}^\dagger$	$3.444 \cdot 10^{-06}$
$\text{O}_2\text{CH}_2\text{OCH}_2\text{O}_2\text{H}$	$2.071 \cdot 10^{-10}$	$\text{CH}_2\text{CO}^\dagger$	$3.497 \cdot 10^{-06}$
$\text{CH}_3\text{OCH}_2\text{OH}$	$2.492 \cdot 10^{-09}$	$\text{CH}_3\text{CHO}^\dagger$	$4.769 \cdot 10^{-06}$
$\text{HOCH}_2\text{OCO}^\dagger$	$6.739 \cdot 10^{-09}$	$\text{C}_3\text{H}_8^\dagger$	$5.441 \cdot 10^{-06}$
$\text{OCHO}^\dagger$	$3.447 \cdot 10^{-08}$	$\text{C}_2\text{H}_5\text{OH}^\dagger$	$1.255 \cdot 10^{-05}$
$\text{CH}_3\text{O}_2\text{H}^\dagger$	$4.290 \cdot 10^{-08}$	$\text{C}_2\text{H}_2^\dagger$	$3.686 \cdot 10^{-05}$
$\text{C}^\dagger$	$1.005 \cdot 10^{-07}$	$\text{C}_2\text{H}_6^\dagger$	$7.851 \cdot 10^{-05}$
$\text{C}_2\text{O}^\dagger$	$1.112 \cdot 10^{-07}$		

• $\dagger$ : Species is QSS in the 33 species mechanism.

Table 2.1.1.: Species with the lowest peak concentrations in the simulation of a homogeneous ignition in the SEC process using the 52 species fuel mechanism provided by RWTH Aachen.

even a toy mechanism qualitatively recreating the reaction paths cannot have less than 7 species — which does not include oxidizer and inert gases yet. The graph does not include all *chain reactions* involved, which also add to the number of species.

A technique allowing for further reduction is the Quasi Steady State (QSS) assumption: If in a reaction chain one product of a relatively slow reaction is the reactant of a relatively fast reaction, and the other reactants of that fast reaction are available in sufficient quantity at all times, it is valid to assume that the concentration of the intermediate species remains small. Since it is small, its variation will not have huge impact on the calculation, and thus it is furthermore valid to assume that it is in local equilibrium, *i.e.*, that the time derivative vanishes. The differential equation previously describing the time evolution of said species becomes an algebraic constraint that can be solved for the species' concentration. If this technique is applied to species whose reactions introduce fast time scales into the system, it can speed up calculation of a numerical solution considerably.

Tools that semi-automate the application of this technique are contained in Flamemaster [60], a chemical kinetics toolbox that, among others, can be used to convert tabulated kinetics to a C or Fortran source file for calculating the right hand side of the kinetics equation (1.2.14). The tool is able to process one QSS assumption at a time, but unable to resolve the algebraic interdependencies if more than one species is in QSS. Instead, it outputs formulae that would hold if each species was the only one which is in QSS. Thus, manual correction is required afterwards.

Since the error tolerance in ignition delay time was already exhausted, QSS could not be applied by Cai *et al.* for further reduction. Instead, reduction was performed on-site in the SEC project using more refined criteria. The author's approach was as follows:

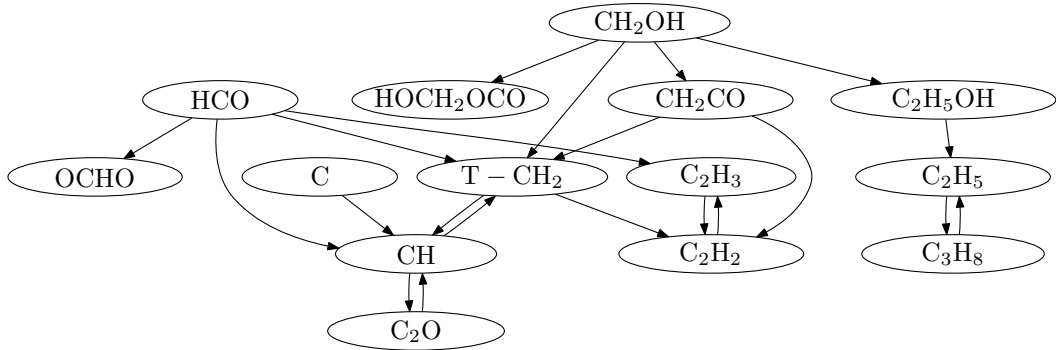


Figure 2.1.2.: Dependency graph for the QSS species in the 34 species mechanism. Edges mark the source vertex as a dependency for the target.

1. A resolved ( $\Delta x = 10^{-4}$  m) simulation of the homogeneous ignition in a SEC with the 52 species mechanism provided by the guest project was set up, and maximal concentrations of all species throughout the combustion evaluated. The species with the lowest peak values are shown in table 2.1.1.
2. For each species, individually, the QSS assumption was made and the simulation repeated, with updated initial data to account for changes in ignition delay time.
3. Multiple species for which this simulation still yielded a homogeneous explosion or at least weak detonation were then assumed to be in QSS at once. To resolve the algebraic interdependencies, a directed graph of the dependencies was computationally generated. Dijkstra's algorithm [23] was then used to derive an evaluation order for all non-cyclic parts of the graph. The cyclic parts were then solved using a computer algebra system, and the equations exported to the mechanism's C source file generated by Flamemaster.
4. Out of the mechanisms generated in the previous step, the smallest one that still yielded a homogeneous detonation or at least weak detonation was chosen, having 34 species. Figure 2.1.2 shows the relational graph of this mechanism.
5. The species where the QSS assumption failed to preserve homogeneous ignition earlier were now removed from this mechanism individually, to assess whether the assumption would hold in combination with the ones for the other species. This allowed to assume QSS for  $C_2H_6$  as well.

The resulting mechanism has 33 species and 245 reactions. In relevant regimes, it speeds up calculations by a factor of 4.8 compared to the 83 species mechanism on average, and 1.5 compared to the 52 species one. Ignition delay times in the NTC region are shown in fig. 2.1.3: They deviate by about 10% from the 83 species mechanism's values, but the error is qualitatively independent of temperature. Since experimental validation of the mechanisms for the SEC application has not been performed yet, quantitative predictions

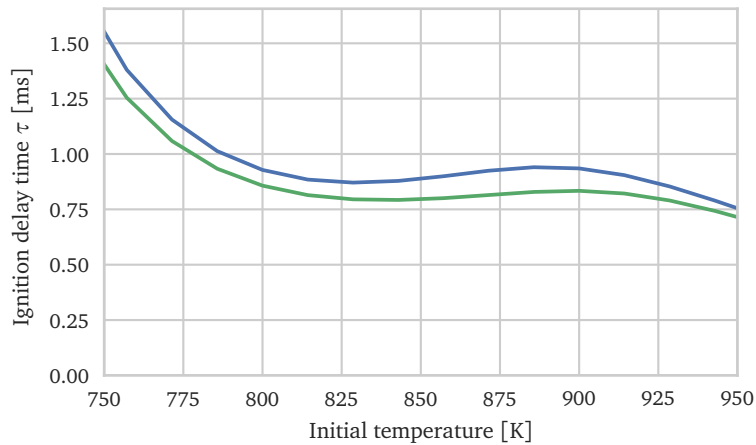


Figure 2.1.3.: Ignition delay times in the NTC region for the 83 species (blue) and reduced 32 species (green) mechanisms at  $p = 30\text{ bar}$  and stoichiometric fuel/air mixture.

are not reliable even for the 83 species mechanism. Hence, the resulting mechanism is considered a good compromise for fast numerical calculations.

Further reduction using automated, online techniques, especially *computational singular perturbation* [47], was considered, but ultimately rejected due to the unfavorable tradeoff between implementation effort and expected computation time savings in 1D simulations. In 3D, this is worth reconsideration.

## 2.2. Model for Idealized SEC Fuels

A mechanism with 33 species still means that a 34 dimensional Ordinary Differential Equation (ODE) system must be solved per computational grid cell. This is sufficient for quantitative calculations, but unsatisfactory for qualitative investigations, where one practically “plays” with the system to understand the process, and performs parameter studies that help understand the influence of the different fuel- and system parameters. It would be preferable to have a lower dimensional system.

A low-dimensional, global Arrhenius mechanism can be used for numerical simulations, but then one loses the temperature independence of auto-ignition delay time that is desired for SEC fuels: The exponential nature of chemical reactions stems from a  $\exp(-1/T)$  term in the reaction rate and reactions raising the temperature  $T$  as they progress. To make auto-ignition delay time of a single reaction independent of initial temperature necessarily means to make the reaction rate a constant. Since this obviously is not a good model for an exponential process anymore, a global mechanism will in general not have temperature-independent auto-ignition delay time. Numerically, the entire system’s state is known, so it is possible to work with such fuel models in simulations by optimizing

the stratification until the simulation yields a perfectly homogeneous ignition. The result of such an optimization has no practical implications though, as it will have very high demands on accuracy. It would hence be preferable to work with a mechanism that features the temperature independence, because then simulations give results that are of interest for real applications with SEC-capable fuels as well.

Such a mechanism has been developed and published by the author in [11]. The reasoning will be summarized in the following.

### 2.2.1. Single-Stage Model

If ignition delay time is independent of temperature, a reaction can be modeled using distinct ignition and excitation phases, governed by different sets of equations. In a reaction modeled by an Arrhenius ansatz, the reaction rate reduces to a constant if one assumes that temperature rise during the ignition phase is negligible, making the ignition process equivalent to an exponential decay. Once the fuel level becomes sufficiently low, the excitation phase begins. In physical systems with approximately time-independent ignition delay time, this process is due to concurring reactions branching into different reaction paths. In the ideal fuel model, a Heaviside function has been multiplied to an Arrhenius ansatz to qualitatively achieve the same effect for the excitation reaction: The excitation reaction rate is zero until the concentration of the decaying species falls below a given threshold. Since decay processes only asymptotically approach zero, one cannot use vanishing concentration as the activation threshold. Instead, a small, non-zero threshold has been defined. The reaction parameters of the excitation reaction were chosen such that once the reaction activates, it does so within its excitation regime, and no extra auto-ignition delay is added. To prevent numerical extinction, the Heaviside-switched reaction has been added to the auto-ignition reaction as well, as an alternative reaction path, to ensure that the decay reaction reaches equilibrium fast once the decaying variable is below the activation threshold.

Having only these two reactions makes ignition delay *completely* independent of temperature. This is undesirable, because it also prevents flame and detonation propagation. What the model should really offer is temperature independence for a certain range of temperatures, and temperature-dependent reaction rates for temperatures relevant to the propagation of combustion fronts. Another reaction path has been added to the ignition reaction to overcome this limitation. The reaction parameters were tuned to create a sharp activation barrier, with an activation energy such that ignition takes place for temperatures according to [9] to specifically allow detonations: The ZND model, which will be introduced in section 3.5.7 in detail, predicts the temperatures occurring in detonations, and the energy may be chosen such that at these temperatures, the reaction branch is active. In practice, it suffices to choose a much smaller temperature, *e.g.*, the upper end of the temperature range where auto-ignition delay time is to be independent of initial temperature.

Another final Arrhenius reaction path in the ignition reaction completes the mechanism. It is present to allow to introduce small temperature dependencies into the reaction in

Term	Description	Value
<b>Parameters responsible for the temperature-independent ignition delay:</b>		
$\lambda$	Decay rate for the fuel species $F$ , chosen such that $F$ decays from $Y_F = 1$ to $Y_F = \varepsilon$ in $\tau = 1$ .	$-\log(\varepsilon)$
$\varepsilon$	Fuel level below which the excitation reaction activates.	0.2
<b>Parameters modeling behaviour of a specific fuel:</b>		
$\vartheta_F$	Arrhenius reaction rate modeling ignition delay above the temperature-independent region.	$2 \cdot 10^{30} \exp(-33/T)$
$\vartheta_I$	Arrhenius reaction rate for the heat-releasing reaction.	$1096 \exp(-3.5/T)$
$\vartheta_T$	Arrhenius reaction rate for reintroducing temperature dependence in numerical studies.	case-dependent
$\Delta Q$	Energy release in the heat-releasing reaction.	$2.7 c_v$

Table 2.2.1.: Model parameters in the single-stage ideal fuel model, tuned to combustion of stoichiometric DME in air at 1000K at 8bar. The table has been reproduced from [11].

numerical experiments. This leads to an overall mechanism

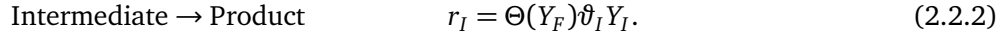
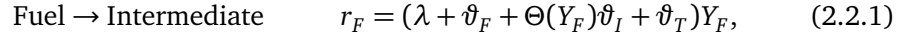


Table 2.2.1 gives an overview over the model parameters.  $\Theta$  is a Heaviside-type function given by

$$\Theta(x) = \begin{cases} 1 & \text{if } x < \varepsilon \cdot (1 - Y_P), \\ 0 & \text{else.} \end{cases} \quad (2.2.3)$$

The unusual factor in the Heaviside function is for numerical stability close to boundaries between fresh fuel and old exhausts, where premature ignition may occur otherwise due to a property of the chosen numerical scheme that will be discussed in chapter 3: It artificially smears species interfaces, creating small absolute values of  $Y_F$  at interfaces of  $Y_F$  and  $Y_P$ , that would lead to premature activation of the second reaction if the factor was not present. With real fuels, mixing of fuel and air, *i.e.*, decreasing the fuel/air equivalence ratio, would increase, rather than decrease, ignition delay time. This is therefore indeed an artifact of the model, and not an issue for the process itself.  $\varepsilon > 0$  is required because an exponential decay reaction asymptotically approaches zero, but a finite ignition delay time is desired instead — the choice of  $\varepsilon$  enters the calculation of the decay rate such that auto-ignition delay time is always  $\tau = 1$  for a reaction that starts with  $T = 1, Y_F = 1$ , making the choice for a value of  $\varepsilon$  one that is primarily of numerical nature. Here,  $\varepsilon = 0.2$  has been used.

The other variables used in the model are the mass fractions  $Y_F$  and  $Y_I$ , and

$$\vartheta_F = A_F \exp(1 - E_F/T) \quad (2.2.4)$$

is a shorthand notation for the non-dimensional Arrhenius rate with parameter index  $F$ .  $\vartheta_F$  corresponds to the high-temperature reaction that marks the end of the temperature-independent region,  $\vartheta_T$  is the reaction that allows to introduce a small temperature

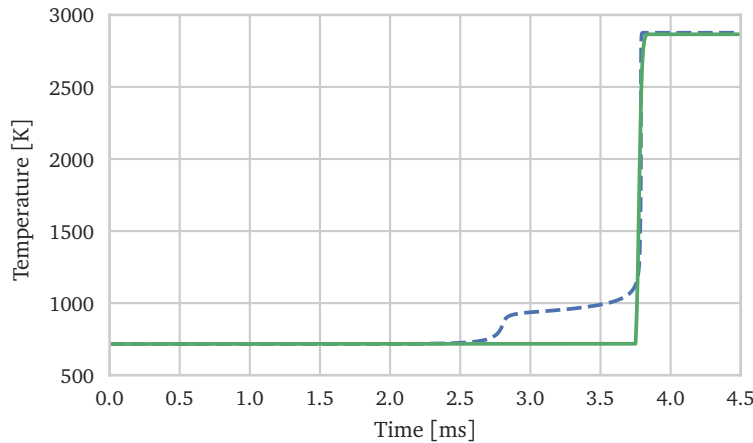


Figure 2.2.1.: Ignition of stoichiometric DME in air at 8 bar using the detailed kinetics model by [18] (dashed) compared to ignition using the single-stage model derived in section 2.2.1.

dependence into the otherwise independent region, and  $\vartheta_I$  is the fast energy releasing reaction. As the reaction parameters  $A_I = \exp(7)$  and  $E_I = 0.5$  have been chosen to achieve excitation times with a magnitude of 0.01, corresponding to  $10\ \mu\text{s}$  in dimensional quantities, that do not depend strongly on temperature, and  $A_F = \exp(70)$  to have a sharp boundary at  $E_F = 1.1$ , where quasi instantaneous combustion replaces the order unity ignition delay. This corresponds to a region of 100 K in which ignition delay times do not depend on temperature. Reaction (2.2.2) releases an amount of energy of  $\Delta Q = 2.7c_v$ . These choices make the reaction resemble the ignition behaviour of stoichiometric DME in air at these conditions.  $\vartheta_T$  is initially zero; it will be used with other values in the numerical experiments of section 4.2.2.

## 2.2.2. Two-Stage Extension

Figure 2.2.1 shows that the model from the previous section captures the auto-ignition behaviour well. It does, however, lack the *multi-stage ignition* that DME exhibits: While fuels whose ignition can be described by a single, global Arrhenius law release most of their energy in a singular, very fast event, fuels with multi-stage ignition behaviour feature multiple ignition and excitation phases following consecutively, each releasing *some* of the energy. For the SEC process, this makes a relevant difference, because if the time between the distinct excitation phases is larger than the acoustic time scale, the chemical reaction process will interact with thermodynamics, complicating the aim for homogeneous auto-ignition.

A straight-forward extension of the single-stage model from the previous section, that simply adds another pair of reactions following the same pattern, allows to include the

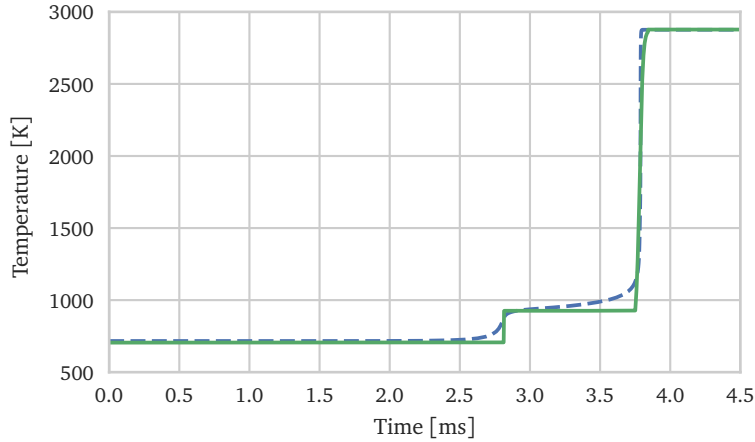
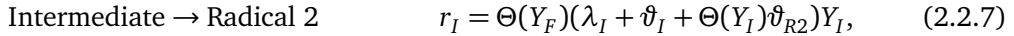
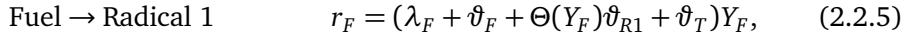


Figure 2.2.2.: Ignition of stoichiometric DME in air at 8 bar (dashed) compared to ignition using the two-stage model from section 2.2.2.

first ignition stage:



This model now has two decay constants,  $\lambda_F$  and  $\lambda_I$ , that must be chosen such that the total ignition delay time remains unchanged, and some fraction of it is spent in the first ignition stage.  $3/4\tau$  has been chosen here. Reaction (2.2.6) releases a fraction of the total energy. For this value,  $\Delta Q_{R1} = 0.15c_v$  has been chosen. Both values are in accordance with the first stage of the DME/air ignition from fig. 2.2.1.

The numerical correction factor  $(1 - Y_P)$  in the definition of the Heaviside function (2.2.3) must be individually adjusted to account for the species that occur later into the reaction.

See fig. 2.2.2 for a comparison between the reaction in this model and an elaborate DME model from [18]. It is noteworthy that tuning of the model parameters allows to quantitatively match the dependence of ignition delay time on initial temperature to the behaviour of their fuel as well, see fig. 2.2.3. Since the aim of the model is to have temperature-independent auto-ignition delay times, however, the fitted version will not be used in the following. Numerical results for both models will be presented in sections 4.2.2 and 4.2.3.

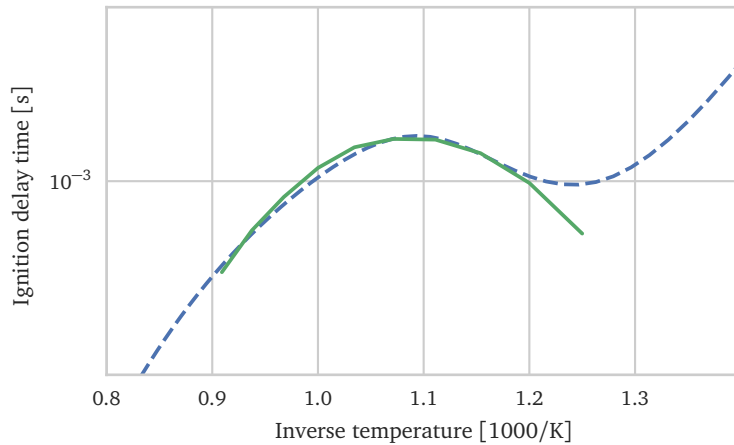


Figure 2.2.3.: Auto-ignition delay time for the fuel blend from [18] at 8 bar (dashed) compared to a fitted version of the two-stage ideal fuel model. Plot reproduced from [12].

## 2.3. Fuel Selection for the Atmospheric SEC Test Rig

The investigation by Cai *et al.* showed that fuels with ideal properties at atmospheric pressure are not available using only the mentioned compounds. At 1 bar, their suggested blend has an approximately temperature-independent ignition delay time for temperatures between 713 K and 720 K, with an absolute ignition delay time of 473 ms. With an estimated average sound speed of 800 m/s, this necessitates a SEC tube that is nearly 190 m long, an obviously impractical value. In contrast, at 30 bar, temperature independence is achieved for initial temperatures from 800 K to 880 K, with absolute values in the order of 1 ms. This facilitates a SEC tube with a length of 0.4 m. At atmospheric pressure, the mixture has further disadvantages that render it undesirable for use in a SEC: The center of the temperature range with approximately constant ignition delay time depends strongly on the equivalence ratio  $\Phi$ . At lean  $\Phi = 0.5$ , it is at 698 K, and the entire temperature region of independence does not even intersect with the one for  $\Phi = 1$ . Since the operating point must be in the temperature-independent region for all equivalence ratios used in the stratification, this means that the range of usable equivalence ratios is narrow. In this calculation, it must also be taken into account that the experiment mixes cold fuel with hot air, making the mixture's temperature depend on the equivalence ratio as well. Since lean mixtures contain less fuel, an experiment set up such that a  $\Phi = 1$  mixture reaches, e.g., 716 K would have an even higher temperature for smaller  $\Phi$ , narrowing the available range of equivalence ratios even further.

To enable optimization of the fuel under these constraints, a numerical optimization framework has been created. Its first use was to choose a fuel and operating point for an experimental setup at Technische Universität Berlin. The experiment's aim was to obtain homogeneous auto-ignition in an isolated fashion, without the resonant recharging of a

SEC. This experiment posed further constraints, that were formulated in collaboration with the experiment's designer Bernhard Bobusch<sup>2</sup>. They are as follows:

- The fuel valve facilitates a flow of 30 kg/h before choking
- A heater is used to pre-heat the air to the temperatures required for auto-ignition of the mixture. The heater requires a minimal mass flow of 25 kg/h.
- Flow velocities up to  $\text{Ma} = 1$  are feasible for the air flow.
- Air can be heated up to 1000 K.
- Fuel can be supplied at temperatures between 50°C, approximately the vaporization temperature at atmospheric pressure, and 200°C, to stay away from temperatures where DME could dissociate and thus auto-oxidize.
- The test tube is to be filled up to 40 cm with a fuel/air mixture. Configurations that allow to fill less than 10 cm are unfeasible.

As the optimization goal, the minimization of

$$\left| \frac{d\tau}{dT} \right|_{\Phi=\Phi_{\max}} + \left| \frac{d\tau}{dT} \right|_{\Phi=\Phi_{\min}} \quad (2.3.1)$$

has been chosen. The meaning of the equivalence ratios' subscripts will become clear below.

Since the parameter space is high-dimensional and is expected to have many local optima, an algorithm has been designed to sample the space efficiently:

1. Repeat the following for each  $\text{N}_2/\text{O}_2$  ratio in 1, 1.5 and 2, and each DME:H<sub>2</sub>:CH<sub>4</sub> ratio in a  $[0.5, 5]^3$  cube sampled by  $20^3$  points (with duplicates removed, *i.e.*,  $20^2$  effectively), and each equivalence ratio  $\Phi$  in  $[0.3, 1]$  sampled in steps of 0.1.
2. Search for all temperature ranges where ignition delay time depends on temperature by less than  $3 \text{ ms/K}$  that are at least 5 K wide. Repeat the following steps for all ranges that have been found.
3. Search for the leanest (lower) equivalence ratio  $\Phi_{\min}$  that is smaller than the original one but still fulfills the constraint that ignition delay time depends on temperature by less than  $3 \text{ ms/K}$  in the same temperature range, or a sub-range that is at least 5 K wide.

In this calculation, take into account that a mixture's temperature will depend on the equivalence ratio, because fuel and air have different initial temperatures. It is assumed that mixing is an isenthalpic process. The fuel's temperature is chosen *a priori* and the air temperature calculated such that the temperature of the previous step is reached for the original equivalence ratio.

---

<sup>2</sup>formerly employed at HFI, TU Berlin; currently CEO of FDX Fluid Dynamix

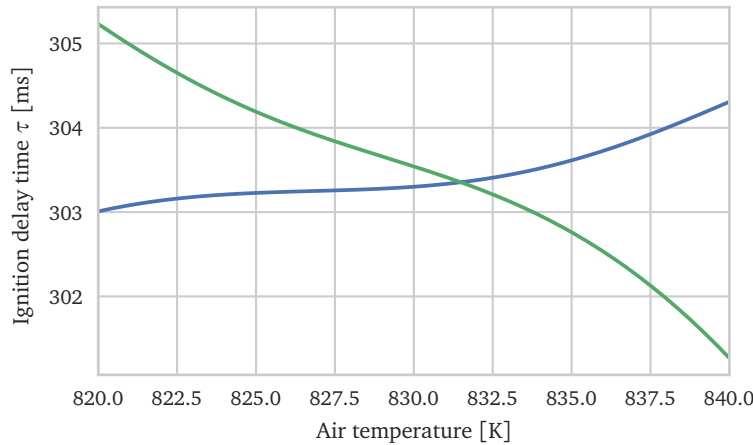


Figure 2.3.1.: Plot showing the dependence of the ignition delay time on air temperature in the prospective fuel mixture. The blue line shows ignition delay time for  $\Phi = 1.0$ , the green one shows  $\Phi = 0.88$  and has been shifted by  $-57.36\text{ ms}$  to improve visibility of the dependence on air temperature. The data has been calculated at atmospheric pressure, with a DME:H<sub>2</sub>:CH<sub>4</sub> mixture with ratios 1.11:1.50:0.29 preheated to 48° C. The charging process must occur at least with 11.5 m/s to fulfill the air flow constraint. In the whole plot range,  $d\tau/dT < 0.3\text{ ms}$  holds.

4. Using both values for  $\Phi$ , calculate minimal and maximal charging velocities and check if they violate the flow rate constraints.

The dependence is as follows:  $\Phi$  determines the amount of substance per volume of the components in the final fuel/air mixture if temperature and pressure are kept constant. These amounts must flow through the fuel valve and heater, respectively. The charging velocity determines how fast this must happen, since the volume of the desired mixture is given. Hence, constraints on the flow rate through valve and heater impose limits on the charging velocity.

5. Choose the largest velocity supported by the valve, preheater and requirement that no more than 40 cm are to be filled with fuel/air mixture. If this velocity violates the constraint that more than 10 cm are to be filled, reject the configuration.
6. Store the configuration together with the evaluated target functional for future, manual evaluation.

This produces a list of feasible configurations. It is then sorted by the target functional. A Newton iteration can finally be used to find a local optimum starting from this value.

Ignition delay times for the winner configuration from this optimization are shown in 2.3.1. The graph shows that the constraint  $d\tau/dT < 0.3\text{ ms}$  is fulfilled.

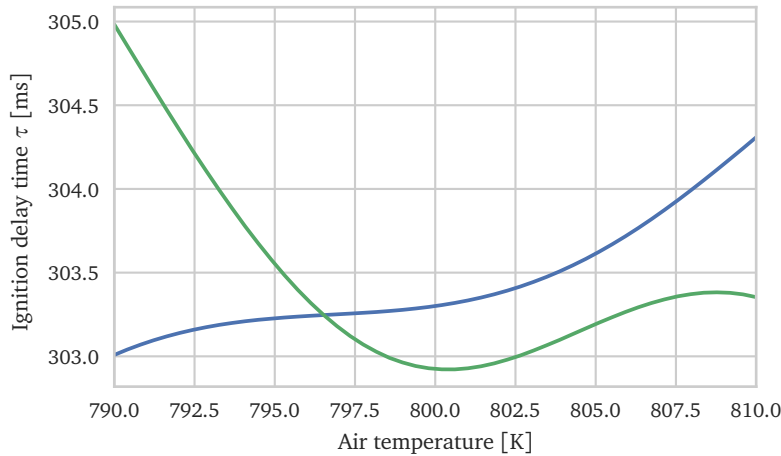


Figure 2.3.2.: Plot showing the dependence of the ignition delay time on air temperature in the prospective DME-only fuel mixture. The blue line shows ignition delay time for  $\Phi = 0.6$ , the green one shows  $\Phi = 0.5775$  and has been shifted by  $-17.8 \text{ ms}$  to improve visibility of the dependence on air temperature. Conditions are as in fig. 2.3.1.

The mixture has a strong dependence on the composition of the actual fuel, rendering its production costly compared to a single-component fuel. Additionally, the advantage in temperature independence over a single-component fuel is not very large. Therefore, a second run was conducted with DME only. Figure 2.3.2 shows ignition delay time of the winner configuration for this run.

An optimization for a fuel for the full SEC has not been conducted, but is viable as well. A new constraint must then be imposed on the minimal ignition delay time  $\tau_{\min}$ : It determines the minimal time that has to pass after the fuel/air volume has been set up until the mixture ignites. This time should either be negligibly small or close to a multiple of the acoustic eigenfrequency if the resonance effect described above is to be exploited.

## 2.4. Numerical Methods for the Simulation of Chemical Kinetics

Solution of chemical kinetics problems involves solving the mass balance ordinary differential equation (1.2.14). Depending on the nature of the problem, one of the thermodynamic potentials is conserved. In the numerical discretization of the reactive Euler equations (1.2.7), the domain will be divided into volumes of fixed size. Hence, *isochoric chemical reactors* will be considered here, *i.e.*, energy is conserved. This enters the problem as an algebraic constraint: Reaction rates depend on temperature and possibly pressure, which themselves depend on energy by the equation of state (1.2.10), which

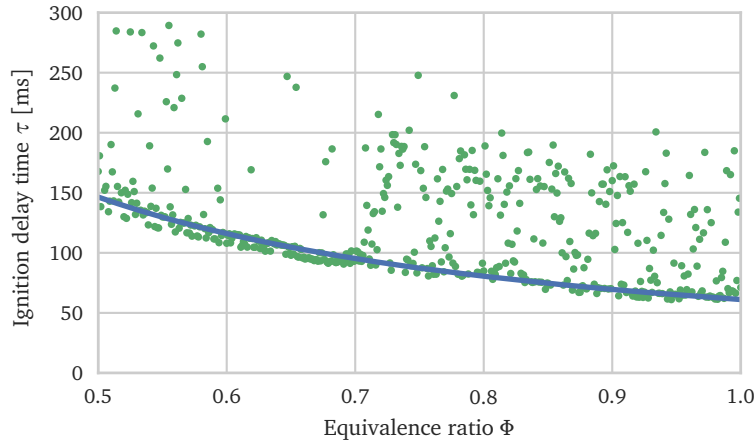


Figure 2.4.1.: Comparison of calculated ignition delay times for chemistry with nearly discontinuous right hand side using CVODE (green dots) and RADAU solver (blue line). Both calculations were set up with the same accuracy goals  $\text{tol}_{\text{rel}} = 10^{-10}$ ,  $\text{tol}_{\text{abs}} = 10^{-15}$ .

Testcase	CVODE	RADAU13	ratio
147 species DME (low prec.)	753	1986	2.64
83 spc. DME/MeOH/EtOH (low prec.)	634	1182	1.86
259 spc. DME/MeOH/EtOH (low prec.)	2208	5637	2.55
GRI 3.0 (low prec.)	331	562	1.70
147 spc. DME (high prec.)	2325	3202	1.38
83 spc. DME/MeOH/EtOH (high prec.)	1790	1656	0.93
259 spc. DME/MeOH/EtOH (high prec.)	6738	8534	1.27
GRI 3.0 (high prec.)	501	739	1.48
147 spc. DME (ultra prec.)	92406	3367	0.04
83 spc. DME/MeOH/EtOH (ultra prec.)	186110	1858	0.01
259 spc. DME/MeOH/EtOH (ultra prec.)	180196	8756	0.05
GRI 3.0 (ultra prec.)	46136	3325	0.07
Calculation of all points in fig. 2.4.1	26986	39279	1.46

Table 2.4.1.: Comparison of CVODE and RADAU solver runtime. Times are given in ms and each is the quickest of five calculations of the same ignition delay time calculation problem on a single i7 core (2.1 GHz). Low precision means  $\text{tol}_{\text{rel}} = 10^{-6}$ ,  $\text{tol}_{\text{abs}} = 10^{-12}$ , high precision means  $\text{tol}_{\text{rel}} = 10^{-10}$ ,  $\text{tol}_{\text{abs}} = 10^{-15}$ , and ultra precision  $\text{tol}_{\text{rel}} = 10^{-13}$ ,  $\text{tol}_{\text{abs}} = 10^{-15}$ . The mechanisms were chosen for their relevance in SEC simulations. CVODE outperforms RADAU most times, except if very stringent accuracy constraints are imposed.

depends on the species concentrations, which change as time evolves due to chemical reaction progress.

In a reaction mechanism, reaction equations like eq. (1.2.15) with various activation energies are usually present. The equations are hence stiff and demand for implicit solvers. Large factors preceding the exponential terms make the transition from low to high reaction rates very steep, hence, adaptive time stepping is preferable as well.

The CVODE code [20] is the de-facto standard for solving such problems. It is used, *e.g.*, in the chemical kinetics packages Cantera, Chemkin and Flamemaster. Algorithmically, its implicit solver relies on Backward Differentiation Formula (BDF) methods. They are of the form

$$\sum_{k=0}^s a_k y_{n+k} = h\beta f(t_{n+s}, y_{n+s}) \quad (2.4.1)$$

with  $\dot{y} = f(t, y)$  the problem to solve,  $t_n = nh$  discrete time, and coefficients  $a_k$  and  $\beta$  chosen appropriately to reach order  $s$ . In contrast to implicit (collocation) Runge-Kutta (RK) methods, which conceptually stem from the idea of interpolating the unknown solution forward in time with intermediate stages between the current and new time level, BDF methods reuse old time levels to determine a single point in the computational future. This allows for high orders at low computational cost, but comes at the disadvantage that they are A-stable only up to order 2. See [37] for a detailed introduction and proof. The CVODE solver adaptively switches between orders to circumvent this restriction, using higher order methods as long as the problem is well behaved.

In the mechanisms provided for the prospective SEC fuels, some reactions activate so steeply that they are numerically perceived as discontinuous jumps in the equation's right hand side. The CVODE code has stability issues in such cases, as can be seen in fig. 2.4.1: It shows random jumps in calculated ignition delay times for a problem where only the ratio of fuel (a blend of  $\text{CH}_3\text{OCH}_3/\text{CH}_4/\text{H}_2$  as suggested in [18]) to air was altered. As per suggestion by Dr. Stephan Gerber<sup>3</sup>, the Hairer/Wanner implementation of the fully implicit RADAU II A RK method [37] was investigated as an alternative. It implements the schemes up to order 13. Figure 2.4.1 also shows the results by this solver: It is able to produce stable results even for numerically ill-conditioned mechanisms. The downside is that, as table 2.4.1 shows, CVODE outperforms the RADAU solver unless particularly high accuracy goals are imposed.

As a compromise, the code introduced in this thesis supports both solvers. The RADAU solver was used for all calculations in this thesis.

It should be noted that the extrapolation methods suggested by Deuflhard for chemical kinetics in [22] have been evaluated as well and found unsuitable for this application, due to the extreme stiffness of the system. Extrapolation methods use a low-order integrator to repeatedly calculate a solution for the same initial conditions and final time, each time using smaller sub-steps, and then extrapolate towards infinitely many sub-steps, gaining a higher convergence order in the process. Spectral deferred correction [25] instead starts off with a fixed number of sub-steps, interpolates a time-dependent solution using the sub-steps as nodes, and builds a differential equation for the error of the

---

<sup>3</sup>Geophysical Fluid Dynamics group, Freie Universität Berlin

solution. This equation is solved using an ODE solver, and the error is subtracted from the solution obtained before. This procedure is repeated iteratively, until the convergence order reaches that of the interpolating polynomial. Since an implicit solver may be used, it is expected that methods of this type perform better than extrapolation methods. Due to the good performance of the RADAU solver, this conjecture has not been verified. In the context of splitting methods in section 3.4.2, this topic will be revisited.

## 2.5. Intermediate Conclusion

Fuels for the SEC process should have a region of temperatures where their auto-ignition delay time remains essentially constant. Such fuels do not admit small computational models using traditional techniques from chemical kinetics.

Using a newly developed tool that is able to investigate multiple QSS assumptions at once, it has nevertheless been possible to obtain a reduced 33 species mechanism for the fuel mixture suggested for SEC use. The key idea is to use an elementary algorithm from graph theory to automate the solution of an algebraic system that had to be solved by hand before. The technique enables automated consideration of all possible QSS assumptions where previously, only a handful of well educated guesses could be investigated in practice.

The solution of problems involving such mechanisms necessitates robust numerical schemes for stiff problems. The RADAU implementation of Hairer/Wanner has been investigated as an alternative to the de-facto standard CVODE and found suitable; in particular, it has been found that the error control of the CVODE code fails in some near-discontinuous cases that the other solver can still handle.

As an alternative to detailed mechanisms, for qualitative investigations of the process, a new approach has been devised to model fuels with temperature-independent auto-ignition delay times. It is considerably simpler and computationally much easier to solve than its traditional counterpart using plain Arrhenius (and third-body) reactions, and yet captures the auto-ignition behaviour very well. A variant of the model is able to represent two-stage ignition behaviour as well.

For atmospheric pressure investigation of homogeneous auto-ignitions, a precursor of a real SEC, an optimal fuel blend has been determined numerically. For the optimization, the essential constraints from the experiment have been identified and taken into account. It has been found that a fuel blend does not perform considerably better than single-component fuels in this situation, and that the best blends have high accuracy demands on their composition. Hence, it was eventually decided to use pure DME in the experiment. A second investigation found the ideal operating point for this fuel.



### 3. Numerical Methods for Multi-Species Gaseous Flow

The simulation of flows with complex chemical kinetics close to their auto-ignition temperature necessitates specialized numerical treatment: Since a wide range of temperatures and large number of species with equally wide ranging heat capacities are involved, it is not appropriate to approximate the fluid as a perfect gas with fixed heat capacity ratio  $\gamma$ . Instead, the ideal gas law (1.2.10) must be used.

It is well known that finite volume schemes for imperfect gases can create oscillations near contact discontinuities separating gases with different compositions (see, e.g., [1, 50, 51]). This effect is in part inevitable, unless one is willing to give up conservation, and in part due to approximate Riemann solvers miscalculating the jump across the contact wave — both cases boil down to the fact that an exchange of energy between two gases with different equations of state results in different changes in temperature and/or pressure in the two gases. This becomes an issue if the oscillations occur at a contact discontinuity with a mixture close to auto-ignition on one side. A small error in temperature can in this case lead to a purely numerical, premature ignition. If, e.g., a detonation develops from this hotspot, a large global error results, especially a large error in the observable if homogeneity of the ignition process is to be assessed.

Several techniques have been created to avoid the issue. In the early 1990s, Karni suggested in [45] to use a primitive formulation of the equations, with pressure as a state variable instead of the energy. This shifts the error from the pressure to the energy field. She then applied a correction to achieve conservation where possible. Abgrall instead stuck with the conservative formulation in [2], and suggested to shift the error from the pressure field to the mass fractions by adjusting them until the pressures of both star-states in the Riemann problem (see section 3.1 below) match. In [43], Jenny *et al.* investigated a similar direction as Karni: They were able to derive a formula for the necessary fix in the energy field for mixtures of perfect,  $\gamma$ -law gases, to prevent oscillations in pressure, and have hence been able to perform the correction in a conservative framework.

For multi-component flows of *immiscible* materials, the issue is more severe, because any numerical mixing leads to an unphysical state. It is state of the art to use a level set function to track the material interfaces [41]. Fedkiw *et al.* reused the concept for gaseous mixtures. They combined it with the idea to calculate two fluxes for each interface and perform an inconervative update where each cell is updated using the flux that would be the solution if the other had the same composition as the updated cell [29]. For the conceptual similarity to Ghost cells, they dubbed their method the *Ghost Fluid Method*. Such tracking methods are not applicable to reactive flows with detailed

chemistry, because there are no distinctive interfaces to track if the chemical composition of the gas can change continuously in space. As a workaround for this limitation, Abgrall and Karni later suggested in a joint publication [3] that the idea to calculate two fluxes can also be used independently of the interface tracking, by simply applying it to *all* cells.

The drawback of such techniques is loss of robustness. All of the above schemes do at some point either become inconervative or inconsistent, as will be demonstrated below in section 3.2. Since one of the aims of developing a simulation for the SEC was to have a code that can be handed to users unfamiliar with such limitations, robustness has been a major design factor.

This chapter is hence devoted to the development of a suitable numerical scheme for the robust simulation of the SEC. It starts with the presentation of the solution to the Riemann problem for ideal gases. Iterating away from the very robust HLLE solver [26, 39] with MUSCL reconstruction [73], it then extends results on perfect gases to ideal gas flows, and argues how the oscillatory behaviour should be dealt with. Basic familiarity of the reader with Godunov-type finite volume methods is expected within this chapter. Appendix A.2 offers a brief introduction to the topic.

## 3.1. Solution of the Riemann Problem for Ideal Gases

For any given hyperbolic system, the solution to the *Riemann problem*, that is, the initial-value problem

$$q(x)|_{t=0} = \begin{cases} q_\ell & \text{if } x < 0, \\ q_r & \text{if } x > 0, \end{cases} \quad (3.1.1)$$

is the essential building block for Godunov-type finite volume methods. If it is known, a numerical scheme can approximate the continuous domain as a series of homogeneously valued volumes, and obtain the problem's time evolution by solving the Riemann problem at each of the interfaces between the volumes and averaging over their solutions at the new time level.

In literature on numerical methods for fluid dynamics, it is customary that authors restrain themselves to presenting the perfect,  $\gamma$ -law case when it comes to solving the Riemann problem. This allows students to quickly grasp the concept, but also hides the pitfalls associated with more complicated equations of state. See, e.g., Toro's derivation in [71]. Here, his disquisition will be generalized to the ideal gas case and presented together with the necessary building blocks.

### 3.1.1. Linearization of the Equations

The solution of the Riemann problem starts out with an analysis of the linearization of the fluid dynamics part of (1.2.7) (*i.e.*, of the Euler equations without chemical source terms):

$$\frac{\partial q}{\partial t} + A \frac{\partial q}{\partial x} = 0, \quad (3.1.2)$$

$$A = \begin{pmatrix} 0 & 1 & 0 & 0 \\ -u^2 + \frac{\partial p}{\partial \rho} & (3-\gamma)u & \gamma-1 & \frac{\partial p}{\partial \rho Y} \\ u \frac{\partial p}{\partial \rho} - uH & H - (\gamma-1)u^2 & \gamma u & u \frac{\partial p}{\partial \rho Y} \\ -Yu & Y & 0 & u \end{pmatrix}, \quad (3.1.3)$$

with

$$H = \frac{\rho E + p}{\rho}, \quad (3.1.4)$$

$$\frac{\partial p}{\partial \rho} = \frac{\partial}{\partial \rho}(\rho RT) \quad (3.1.5)$$

$$= RT - RT + \frac{\rho R}{c_v} \frac{\partial e}{\partial \rho} + \rho R \left. \frac{\partial T}{\partial c_v} \right|_{e=\text{const}} \frac{\partial c_v}{\partial \rho} \quad (3.1.6)$$

$$= (\gamma - 1) \frac{1}{2} u^2 - (\gamma - 1)e + \left. \frac{\partial T}{\partial c_v} \right|_{e=\text{const}} \frac{\partial c_v}{\partial \rho} \quad (3.1.7)$$

$$= (\gamma - 1) \frac{1}{2} u^2 - (\gamma - 1)e - \frac{1}{\partial c_v / \partial T} \frac{c_v}{\rho}, \quad (3.1.8)$$

$$\frac{\partial p}{\partial \rho Y} = \vec{R}T + \left. \frac{\partial T}{\partial c_v} \right|_{e=\text{const}} \frac{\partial c_v}{\partial \rho Y} \quad (3.1.9)$$

$$= \vec{R}T + \frac{1}{\partial c_v / \partial T} \frac{\vec{c}_v}{\rho}. \quad (3.1.10)$$

Steps (3.1.8) and (3.1.10) are only valid if the heat capacities have a non-zero temperature derivative. If they do not, the corresponding terms vanish from the equation. As a reminder,  $\vec{R}$  is the vector of the species' specific gas constants, and  $\vec{c}$  the vector of specific internal energies. Only one species is shown in  $A$  for improved readability. If the matrix would contain all of them, each entry of  $\vec{R}$  would contribute to its own column. Note that to recover the perfect gas case, one has to add up the columns corresponding to the density and species' densities. The  $(\gamma - 1)e$  term from the  $\partial p / \partial \rho$  derivative and the  $\vec{R}T$  term from the  $\partial p / \partial \rho Y$  derivative then cancel.

### 3.1.2. Primitive Form of the Equations

To calculate the full eigenstructure of this system, it is convenient to switch to primitive variables. Here, the equation system reads

$$\frac{\partial}{\partial t} \begin{pmatrix} \rho \\ u \\ p \\ Y \end{pmatrix} + \begin{pmatrix} u & \rho & 0 & 0 \\ 0 & u & 1/\rho & 0 \\ 0 & \gamma p & u & 0 \\ 0 & 0 & 0 & u \end{pmatrix} \frac{\partial}{\partial x} \begin{pmatrix} \rho \\ u \\ p \\ Y \end{pmatrix} = 0, \quad (3.1.11)$$

which has a block structure, with the upper left block being exactly the same as for the single-component, perfect gas case. Hence, the eigenstructure remains unchanged — see, e.g., [53] for the primitive form of the gradient matrix in the perfect gas case — but the  $u$ -eigenvalue gains an additional eigenvector per species.

The structure of the Riemann problem's solution is therefore as follows: There are 3 distinct eigenvalues,  $u$  and  $u \pm c$ , with

$$c = \sqrt{\frac{\gamma p}{\rho}} \quad (3.1.12)$$

the local sound speed. The  $u$  eigenvalue is  $n$ -fold, where  $n$  is the number of species in the system. Each wave associated with the  $u$  eigenvalue transports one of the species. The two other eigenvalues correspond to pressure waves, as they do in the single-gas case. This agrees with the solution structure for mixtures of perfect gases [51].

### 3.1.3. Riemann Invariants

The primitive form of the equations is furthermore useful to derive the system's Riemann invariants. A Riemann invariant is a function of the state that remains unchanged through smooth waves, and hence useful in determining the solution to the Riemann problem. To find them, denote a prospective Riemann invariant for the  $i^{th}$  wave by  $\Psi^i$ . Denoting right eigenvectors of the matrix in eq. (3.1.11) with  $r_n$  and associated left eigenvectors with  $\ell_n$ ,

$$\nabla \Psi^i \cdot r_i = 0 \quad (3.1.13)$$

must hold. Since the eigenvectors form an orthogonal basis, one can write

$$\nabla \Phi^i = \sum_{j \neq i} \mu_j^i \ell_j, \quad (3.1.14)$$

to have eq. (3.1.13) automatically fulfilled. It remains to determine  $\mu_j^i$  such that the expression is integrable, *i.e.*, such that  $\Phi$  exists.

The right eigenvectors of the matrix in eq. (3.1.11) are, written as a single matrix, in order associated with the  $u - c$ ,  $u$ , and  $u + c$  eigenvalues:

$$\begin{pmatrix} -\rho/c & 1 & 0 & \rho/c \\ 1 & 0 & 0 & 1 \\ -\rho c & 0 & 0 & \rho c \\ 0 & 0 & 1 & 0 \end{pmatrix}. \quad (3.1.15)$$

The inverse of this matrix is

$$\begin{pmatrix} 0 & 1/2 & -1/2c\rho & 0 \\ 1 & 0 & -1/c^2 & 0 \\ 0 & 0 & 0 & 1 \\ 0 & 1/2 & 1/2c\rho & 0 \end{pmatrix}. \quad (3.1.16)$$

The equations (3.1.14) for the  $\mu_j^i$  therefore read:

$$\nabla \Psi^1 = \mu_2^1 d\rho + \mu_4^1 \frac{1}{2} du + \left( \mu_4^1 \frac{1}{2c\rho} - \mu_2^1 \frac{1}{c^2} \right) dp + \mu_3^1 dY, \quad (3.1.17)$$

$$\nabla \Psi^2 = (\mu_1^2 + \mu_4^2) \frac{1}{2} du + (\mu_4^2 - \mu_1^2) \frac{1}{2c\rho} dp + \mu_3^2 dY, \quad (3.1.18)$$

$$\nabla \Psi^3 = \mu_2^3 d\rho + (\mu_1^3 + \mu_4^3) \frac{1}{2} du + \left( (\mu_4^3 - \mu_1^3) \frac{1}{2c\rho} - \mu_2^3 \frac{1}{c^2} \right) dp, \quad (3.1.19)$$

$$\nabla \Psi^4 = \mu_2^4 d\rho + \mu_1^3 \frac{1}{2} du + \left( -\mu_1^4 \frac{1}{2c\rho} - \mu_2^4 \frac{1}{c^2} \right) dp + \mu_3^4 dY. \quad (3.1.20)$$

Choices leaving only one differential are obvious solutions: Choose  $\mu_1 = \mu_2 = \mu_4 = 0$ ,  $\mu_3 = 1$  to see that  $Y$  is a Riemann invariant for the 1<sup>st</sup>, 2<sup>nd</sup> and 4<sup>th</sup> wave. The choice  $\mu_1 = \pm \mu_4$ ,  $\mu_2 = \mu_3 = 0$  yields  $u$  and  $p$  as invariants of the 2<sup>nd</sup> and 3<sup>rd</sup> wave.

The remaining invariants are nontrivial. For any but the 2<sup>nd</sup> wave, if  $\gamma$  is constant,

$$d\rho - \frac{1}{c^2} dp = d\rho - \frac{\rho}{\gamma p} dp \quad (3.1.21)$$

$$= \frac{\rho}{\gamma} \left( \gamma \frac{d\rho}{\rho} - \frac{dp}{p} \right) \quad (3.1.22)$$

$$= -\frac{\rho}{\gamma} d \log \left( \frac{p}{\rho^\gamma} \right), \quad (3.1.23)$$

which makes  $p/\rho^\gamma$  a Riemann invariant of these waves; for non-constant  $\gamma$ , such a closed expression is not available, but the invariant can still be identified as a function of entropy alone: From the fundamental relation of thermodynamics in its formulation for ideal gases,

$$T dS - p dV = 1/\gamma T dS + 1/\gamma V dp \quad (3.1.24)$$

$$\Rightarrow dS = -c_v \left( \gamma \frac{d\rho}{\rho} - \frac{dp}{p} \right), \quad (3.1.25)$$

which is (up to a factor that can be moved into  $\mu$ ) the same differential as in eq. (3.1.22). For perfect gases, the differential relation from eq. (3.1.22) can be used to derive  $u \pm 2c/(\gamma-1)$  respectively as another Riemann invariant of the 1<sup>st</sup> and 4<sup>th</sup> wave. This result does not hold for ideal gases, because its derivation requires that a closed expression for the other invariant (*i.e.*, entropy) is available. What is available though, is the differential equation

$$du + \frac{1}{c\rho} dp = du + \sqrt{\frac{1}{\gamma p \rho}} dp = du + \sqrt{\frac{1}{\gamma p \rho}} \frac{\gamma p}{\rho} d\rho. \quad (3.1.26)$$

This equation can be integrated to numerically determine, given either pressure or the velocity, the value of the other variable through a 1-wave or 4-wave.

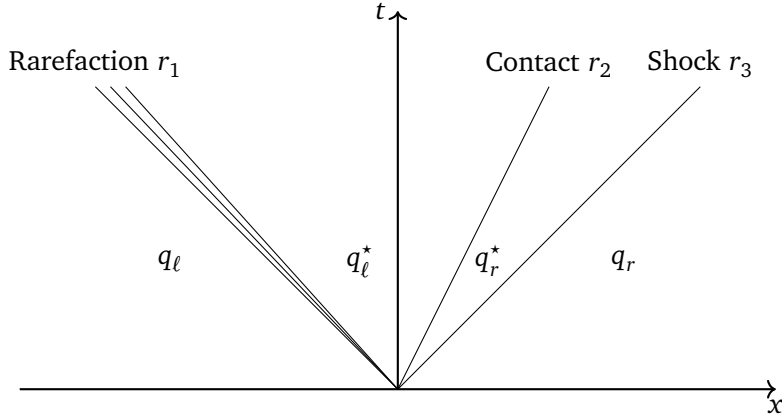


Figure 3.1.1.: Typical wave structure of the solution to the Riemann problem for the Euler equations.

### 3.1.4. Solution Strategy

Since the additional waves due to the individual species' mass transport coincide with the central wave, the Riemann problem's solution structure remains unchanged from the case of a single, perfect gas: As depicted in fig. 3.1.1, there still is a fan enclosed by two pressure waves, which can either be shock waves or smooth rarefactions depending on the problem. A central wave separates two gases at different temperatures but equal pressure and velocity, only that now also the composition may differ through this wave, and this wave alone, due to the additional degrees of freedom. It is hence feasible to use the same solution strategy as [71] suggests to use for perfect gases:

Assume that the pressure inside the fan,  $p^*$ , is given. Consider a shock wave like  $r_3$  in the figure. By formulating the Euler equations in a reference frame moving with the shock, i.e., speed  $s_{r_3}$ , such that the time derivatives vanish (in a vicinity of the shock and for small times), jump conditions for energy and momentum through the shock may be derived<sup>1</sup>: The *Hugoniot* energy equation

$$\frac{1}{2}(p^* + p_r)\left(\frac{1}{\rho^*} - \frac{1}{\rho_r}\right) + e_r^* - e_r = 0 \quad (3.1.27)$$

can be solved numerically to find the density  $\rho^*$ . The *Rayleigh line*

$$p^* = p_r - \rho_r^2(u_r - s_{r_3})^2\left(\frac{1}{\rho_r^*} - \frac{1}{\rho_r}\right) \quad (3.1.28)$$

then fixes the wave speed  $s_{r_3}$  and central velocity  $u^* = \rho_r(u_r - s_{r_3})/\rho^* + s_{r_3}$ .

For rarefaction waves like  $r_1$ , density  $q_\ell^*$  and velocity  $u^*$  can be calculated using relations (3.1.26) and (3.1.22), by integrating from  $p_\ell$  to  $p^*$ . Since the rarefaction is smooth, signal velocities are simply  $u_\ell - c_\ell$  and  $u^* - c_\ell^*$ , respectively at either end of the rarefaction

---

<sup>1</sup>Section 3.5.7 features more details on the shock relations in the context of detonation waves.

fan. Inside,  $x/t = u - c$  must hold. Solving this equation and eq. (3.1.26) simultaneously yields the inner structure of a rarefaction.

Shocks decreasing pressure and rarefactions increasing pressure are not allowed [53, chapter 14]: One can calculate directly that a pressure decreasing shock would decrease entropy in violation of the second law of thermodynamics. In a pressure increasing rarefaction, the star-side of the fan would move outwards faster than the outer end, which does not make physical sense and leads to discontinuous solutions.

If the star pressure  $p^*$  is therefore smaller than the pressure on the other side of a wave, said wave must be a rarefaction, otherwise it is a shock. This allows, given  $p^*$ , to decide which set of formulae to use to calculate the star states.

By application of the preceding argument, it is possible to calculate for both  $r_1$  and  $r_3$  the star velocity  $u^*$  given the pressure  $p^*$ . Since it is known that  $r_2$  preserves both velocity and pressure, the correct pressure can be found by numerically solving for a pressure that yields the same  $u^*$  for both waves. The solvability of the equations is discussed in [53]. The author's argument is valid for ideal gases as well. In particular, he discusses the case of vacuum generation inside the fan, which requires special treatment, but is of no concern here, because the approximate Riemann solver discussed in the next section is designed to avoid it.

The solution strategy already yields the densities within the star region as well. It is known that the mass fractions change only through the  $r_2$  wave. To complete the solution of the Riemann problem, only the speed of the central wave  $s_{r_2}$  remains to be determined. As in the perfect gas case, it must be equal to  $u^*$ , since by eq. (3.1.15) the  $r_2$  wave is linearly degenerate and any other value would hence be contradictory.

In summary, the ideal gas case still allows to solve the Riemann problem exactly, but a numerical realization requires, in most cases, two nested invocations of Newton solvers: One to solve for  $p^*$ , and another one to obtain  $u^*$  from the  $p^*$  candidate for (each of) the shock wave(s). Compared to the perfect gas case, it is hence considerably more expensive to obtain an exact solution to the Riemann problem.

## 3.2. The HLLE Solver in Multi-Species Simulations

The HLLE approximate Riemann solver, named after its inventors Harten, Lax, van Leer [39] and Einfeldt [26], is based on the idea to reduce the solution to the Riemann problem to the two outermost waves. If estimates for the speeds of said waves are available, denoted  $b_\ell$  and  $b_r$  in the following, then a single intermediate state can be derived from the conservation law. Only the case  $b_\ell < 0 < b_r$  is considered, because otherwise, the exact flux can be obtained easily: If  $b_\ell > 0$ , then the flow is supersonic and  $f(q_l)$  is the exact flux, and if  $b_r < 0$ , then  $f(q_r)$  is the exact solution. Again, only the fluid dynamical part of eq. (1.2.7) is considered. Integration of the system over a time step  $\Delta t$  and a volume  $\Delta x$  centered at the cell interface for which the Riemann problem is to be solved, with  $\Delta t$  assumed to be sufficiently small for the Courant-Friedrichs-Lowy (CFL)

condition to be fulfilled, yields

$$q^* = \frac{f(q_\ell) - f(q_r) + b_r q_r - b_\ell q_\ell}{b_r - b_\ell} \quad (3.2.1)$$

for the central state. In a second step, another integral is taken, this time with a volume that spans half a cell, such that the flux through the cell interface appears in the integral. The resulting equation can be solved for the flux at the cell interface  $f^*$ , resulting in the approximate flux

$$f^* = \frac{b_r f(q_\ell) - b_\ell f(q_r) + b_\ell b_r (q_r - q_\ell)}{b_r - b_\ell}. \quad (3.2.2)$$

Einfeldt showed that good choices for the wave speed estimates are

$$b_\ell = \min \{u_{\text{roe}} - c_{\text{roe}}, u_\ell - \beta c_\ell\}, \quad b_r = \max \{u_{\text{roe}} + c_{\text{roe}}, u_r + \beta c_r\}, \quad (3.2.3)$$

with  $u_{\text{roe}}$  the Roe average [63]

$$u_{\text{roe}} = \frac{\sqrt{\rho_\ell} u_\ell + \sqrt{\rho_r} u_r}{\sqrt{\rho_\ell} + \sqrt{\rho_r}} \quad (3.2.4)$$

and  $c_{\text{roe}}$  the sound speed of the Roe averaged state, for which he has suggested

$$c_{\text{roe}}^2 \approx \frac{\sqrt{\rho_\ell} c_\ell^2 + \sqrt{\rho_r} c_r^2}{\sqrt{\rho_\ell} + \sqrt{\rho_r}} + \frac{\sqrt{\rho_\ell} \sqrt{\rho_r}}{2(\sqrt{\rho_\ell} + \sqrt{\rho_r})^2} (u_r - u_\ell)^2 \quad (3.2.5)$$

as an approximation for the ideal gas case.  $\beta$  is 1 in the original HLLE scheme [26]. In [28], the authors showed that this scheme is positive for perfect gases, *i.e.*, ensures that density and pressure remain non-negative (and in this case, in fact, positive). They furthermore proved that for perfect gases the choice

$$\beta = \sqrt{\frac{\gamma - 1}{2\gamma}} \quad (3.2.6)$$

suffices to ensure positivity. Smaller choices of  $\beta$  reduce the numerical dissipation near rarefaction waves and are hence favorable.

### 3.2.1. Positivity

The positivity result for perfect gases does not readily generalize to the ideal gas case. For super sonic flow, the HLLE solver yields the exact flux. Therefore, only the case  $b_\ell < 0 < b_r$  will be considered.

The update step of the HLLE solver can be interpreted as a convex combination of the old time level with the  $q^*$  state within the Riemann solution's fan. It hence suffices to show that the  $q^*$  state is positive (provided that  $q_\ell$  and  $q_r$  were) to show overall positivity. For density, Einfeldt's proof holds for ideal gases as well: By eq. (3.2.1),

$$\rho^* = \frac{(u_\ell - b_\ell)\rho_\ell + (b_r - u_r)\rho_r}{b_r - b_\ell} \geq \frac{\beta c_\ell \rho_\ell + \beta c_r \rho_r}{b_r - b_\ell} > 0. \quad (3.2.7)$$

This readily generalizes to any advected quantity, as this thesis' author showed in [10]. Positivity of the mass fractions is hence guaranteed as well.

Positivity of pressure, on the other hand, is not. It suffices to show positivity of internal specific energy  $e$ , since the heat capacity  $c_v$  is positive,  $e$  is a function of  $T$ , and the ideal gas relation  $p = \rho RT$  holds. By definition,

$$e^* = \frac{(\rho E)^*}{\rho^*} - \frac{1}{2} \left( \frac{(\rho u)^*}{\rho^*} \right)^2. \quad (3.2.8)$$

By plugging in the definition of the star states, eq. (3.2.1), one arrives at a lengthy expression which must be proved non-negative. Since the star state depends on the flux, pressure enters into this equation, and differences of terms depending on pressure and terms depending on internal energy must be balanced. For ideal gases, the relation between energy and pressure has no closed expression, so no closed expression for the ideal choice of  $\beta$  can be expected — contrary to the perfect gas case, where eq. (3.2.6) is sharp. It is still possible to establish a bound guaranteeing positivity though: Since

$$e = \int c_v \, dT > T \min_T c_v \quad (3.2.9)$$

holds, and

$$\gamma = \frac{c_v + R}{c_v} \quad (3.2.10)$$

is a decreasing function in  $c_v$ , equally

$$e > \frac{p}{\rho(\gamma_{\max} - 1)} \quad (3.2.11)$$

holds. The right hand side of this inequality is the energy equation of a perfect gas with  $\gamma = \gamma_{\max}$ , for which Einfeldt's proof holds. The reasoning then is as follows:

It must be shown that eq. (3.2.8) is positive. As in Einfeldt's proof, define

$$a_\ell = u_\ell - b_\ell, \quad a_r = b_r - u_r. \quad (3.2.12)$$

Equation (3.2.8) can then be written as

$$(\rho e)^* \geq a_\ell (\rho E)_\ell + u_\ell p_\ell + a_r (\rho E)_r - u_r p_r - \frac{(a_r \rho_r u_r + a_\ell \rho_\ell u_\ell + p_\ell - p_r)^2}{2(a_r \rho_r + a_\ell \rho_\ell)} \quad (3.2.13)$$

$$\begin{aligned} &\geq \frac{a_\ell p_\ell + a_r p_r}{\gamma_{\max} - 1} + \frac{1}{2} a_\ell \rho_\ell u_\ell^2 + u_\ell p_\ell + \frac{1}{2} a_r \rho_r u_r^2 - u_r p_r \\ &\quad - \frac{(a_r \rho_r u_r + a_\ell \rho_\ell u_\ell + p_\ell - p_r)^2}{2(a_r \rho_r + a_\ell \rho_\ell)}. \end{aligned} \quad (3.2.14)$$

Multiplication by the positive denominator gives

$$\begin{aligned} & \frac{a_\ell p_\ell + a_r p_r}{\gamma_{\max} - 1} (a_r \rho_r + a_\ell \rho_\ell) + u_\ell p_\ell a_r \rho_r + u_\ell p_\ell a_\ell \rho_\ell - u_r p_r a_r \rho_r - u_r p_r a_\ell \rho_\ell \\ & - \frac{1}{2} (a_r \rho_r u_r)^2 - \frac{1}{2} (a_\ell \rho_\ell u_\ell)^2 - \frac{1}{2} (p_\ell - p_r)^2 + \frac{1}{2} a_\ell a_r \rho_\ell \rho_r (u_r - u_\ell)^2 \\ & + \frac{1}{2} a_\ell^2 \rho_\ell^2 u_\ell^2 + \frac{1}{2} a_r^2 \rho_r^2 u_r^2 - (p_\ell - p_r)(a_r \rho_r u_r + a_\ell \rho_\ell u_\ell) \end{aligned} \quad (3.2.15)$$

$$\begin{aligned} & = \frac{a_\ell p_\ell + a_r p_r}{\gamma_{\max} - 1} (a_r \rho_r + a_\ell \rho_\ell) + \frac{1}{2} a_\ell a_r \rho_\ell \rho_r (u_r - u_\ell)^2 \\ & - (a_r \rho_r p_\ell + a_\ell \rho_\ell p_r)(u_r - u_\ell) - \frac{1}{2} (p_\ell - p_r)^2. \end{aligned} \quad (3.2.16)$$

Expression (3.2.16) is equivalent to the expression Einfeldt arrives at in [28, p. 294, eq. (A8)] in his perfect gas derivation for two dimensions. He shows that for this expression to be positive,

$$a_\ell^2 \geq \frac{\gamma_{\max} - 1}{2\gamma_{\max}} \tilde{c}_\ell^2, \quad a_r^2 \geq \frac{\gamma_{\max} - 1}{2\gamma_{\max}} \tilde{c}_r^2 \quad (3.2.17)$$

must be fulfilled, with

$$\tilde{c} = \sqrt{\frac{\gamma_{\max} p}{\rho}} \geq \sqrt{\frac{\gamma p}{\rho}} = c. \quad (3.2.18)$$

This makes

$$\beta = \sqrt{\frac{\gamma_{\max} - 1}{2 \max\{\gamma_\ell, \gamma_r\}}} \quad (3.2.19)$$

a viable choice for  $\beta$  in the ideal gas case. If  $\gamma_{\max}$  is unknown, a general upper bound can be used at the cost of higher numerical diffusion, e.g.,

$$\beta = \sqrt{\frac{1}{2 \max\{\gamma_\ell, \gamma_r\}}} \quad (3.2.20)$$

or even  $\beta = 1/2$  if  $\gamma$  is not readily available at all, which still is an improvement over the original choice of  $\beta = 1$ .

### 3.2.2. Pressure Oscillations at Contact Discontinuities

Consider the Riemann problem

$$q(x)|_{t=0} = \begin{cases} (p = p_0, u = u_0, T = T_\ell, Y = Y_\ell) & \text{for } x < 0, \\ (p = p_0, u = u_0, T = T_r, Y = Y_r) & \text{for } x > 0. \end{cases} \quad (3.2.21)$$

According to section 3.1, the exact solution to this problem consists of a single contact wave with velocity  $u_0$ . Unless the CFL number is chosen such that one time step advects the wave front exactly one cell ahead, a Godunov type conservative scheme must

necessarily project the solution within the cell containing the discontinuity down to a single state by forming the appropriate convex combination of the left and right state. For convex combinations of states, the following theorem, which has been published in [10], holds:

**Theorem 3.2.1.** *Let  $(\alpha_i)$  label the coefficients of a linear combination of states represented by the conserved quantities. Furthermore assume that the states have a common velocity.*

1. *The combined state preserves temperature equilibria.*
2. *For initially equal pressures  $p_0$ , the combined state has a pressure of*

$$p = \sum_i \alpha_i \rho_i R_i T = p_0 \sum_i \alpha_i \frac{T}{T_i}. \quad (3.2.22)$$

*In particular, if the states are in temperature equilibrium and the combination is convex, the pressure is maintained.*

*Proof of theorem 3.2.1.* Denote the different state variables going into the linear combination with subscript indexes and use superscript indexes for the different mass fractions  $Y^j$ . For the final state, the subscript is omitted. First, assume that  $T_i = T_0$  for all states  $i$ . For the internal energy

$$\rho e = \rho \int^T c_v(\tau) d\tau = \rho \sum_j Y^j \int^T c_v^j(\tau) d\tau = \sum_i \alpha_i \rho_i \int^T c_{v,i}(\tau) d\tau \quad (3.2.23)$$

holds. Note that the upper integral bound is the final temperature  $T$  and not the states' temperature  $T_i$ . Since different velocities are not considered, the internal energy is a conserved quantity, so

$$\sum_i \alpha_i \rho_i \int^T c_{v,i}(\tau) d\tau = \sum_i \alpha_i \rho_i e_i \quad (3.2.24)$$

must hold for any choice of  $\alpha_i$ . Consequently, the integrals on the left-hand side must be equal to the corresponding energies  $e_i$ . Finally, since energy is an injective function of  $T$ ,  $T = T_0$ . For the pressure relations, assume  $p_i = p_0$  for all  $i$ . By applying the ideal gas law,  $p = \rho RT$ ,

$$\begin{aligned} p &= \left( \sum_i \alpha_i \rho_i \right) \left( \hat{R} \sum_j \frac{1}{M^j} \frac{\sum_i \alpha_i \rho_i Y_i^j}{\sum_i \alpha_i \rho_i} \right) T = \left( \hat{R} \sum_j \frac{1}{M^j} \sum_i \alpha_i \rho_i Y_i^j \right) T \\ &= \left( \hat{R} \sum_i \sum_j \frac{\alpha_i \rho_i X_i^j}{M_i} \right) T = \sum_i \alpha_i \rho_i R_i T = \sum_i \alpha_i p_i \frac{T}{T_i}. \end{aligned} \quad (3.2.25)$$

In the last equation,  $\hat{R}$  denotes the universal gas constant,  $X^j$  the mole fractions,  $M^j$  the species' molar masses, and  $M_i$  the mean molar mass of the  $i^{\text{th}}$  state. The expression is already in the form stated in the theorem. If  $T_i = T$  for all  $i$  the fraction cancels and the final claim is established. ■

From theorem 3.2.1, one immediately sees that a numerical scheme solving the Riemann problem (3.2.21) will in general produce states with pressures deviating from initial pressure  $p_0$ , because it diffuses the solution within each cell to a single state by means of convex combinations.

In [10], a thought experiment shows that this effect is not purely an artifact from numerical diffusion, but that physical diffusion disturbs pressure equilibria as well: Assume that the Riemann problem eq. (3.2.21) is set up in a closed, physical domain, and choose a coordinate system such that the contact discontinuity is stationary. Thermal and species diffusion eventually equilibrate the whole volume to a single state. Assume that the contact discontinuity is located a fraction of  $\alpha$  into the volume. Thermodynamics allows to split the equilibration into two processes: First, each gas isothermally expands to the whole domain. By Boyle's law, the final pressures are  $p_\ell = p_0\alpha$  and  $p_r = p_0(1-\alpha)$ . The sum of the partial pressures equals the original pressure  $p_0$ , as one would expect from Dalton's law. In the second step, the temperatures isochorically equilibrate. By the ideal gas law,  $\Delta p_i = \rho_i R_i \Delta T_i$ . The pressure remains constant if, and only if,

$$\rho_\ell R_\ell \Delta T_\ell = -\rho_r R_r \Delta T_r. \quad (3.2.26)$$

For the equilibration, on the other hand,

$$\rho_\ell c_{v,\ell}(T_\ell) dT_\ell = -\rho_r c_{v,r}(T_r) dT_r \quad (3.2.27)$$

holds. The pressure is therefore in general not maintained, but will change due to thermal equilibration.

Pressure oscillations and numerical diffusion are hence linked. The question of how to prevent oscillations while maintaining conservation and consistency therefore boils down to the question of how to preserve sharp contact discontinuities in Godunov-type numerical schemes.

This question has been discussed in depth by the community, and it has in particular been found that lack of numerical diffusion leads to unstable codes [34, 70, 74]. There is an intuitive explanation for this: As has been stated in the introduction, it is known that the diffusion term in the Navier-Stokes equations smoothens solutions, which in the first place allows to consider them as solutions to the differential equation rather than of an underlying integral equation with a wider solution space. Although this is not generally proven, existence and uniqueness of strong solutions is a safe working assumption for the Navier-Stokes equations with non-vanishing viscosity. Gradients in the solution may however be so steep that coarsely resolved numerical solutions might still appear discontinuous. If the overall timescales allow to neglect diffusion in the whole problem and the Euler equations are used, then this is no longer a purely numerical issue that can be resolved using higher resolutions, but solutions can actually become discontinuous, and are no longer unique. One then has to define the unique, physical solution as the solution corresponding to that of the Navier-Stokes equations in the vanishing viscosity limit, and can only state that all solutions of an approximating sequence would (probably) be smooth. Numerical schemes which at some point of their derivation use differentiability of the solution — which is the case for all schemes that are of higher than first order

— do then naturally become unstable, because they assume that a derivative does exist where it actually does not. For the Euler equations, this accumulates in the following observation:

*By introducing numerical diffusion to the solution of the equations, one no longer solves the Euler equations, but actually a set of Navier-Stokes equations with a problem-dependent diffusion coefficient, ensuring that the numerical solutions remain sufficiently smooth.*

In [27], Einfeldt states that a related physical insight has been his motivation for the HLLE(M) solver:

The HLLE solver is based on the assumptions that a shear and contact discontinuity in the Riemann solution is a mathematical inadequate approximation and must be replaced by a transition layer.

In fact, in combination with the original HLLE paper [26], the calculations from section 3.2.1 can be interpreted to serve the purpose of determining how much diffusion exactly is required for the scheme to be guaranteed to produce stable results. Einfeldt has been able to produce a sharp bound for perfect gases, this thesis managed to provide an estimate for ideal gases.

In the context of his HLLE solver, it is hence sensible to accept pressure oscillations in solutions for eq. (3.2.21), and instead question whether initial data that produces them is physically reasonable. This is supported by the conclusion of the discussion of pressure oscillations in [10], where it has been noted that an expansion of eq. (3.2.22) in the specific gas constants results in

$$p = p_0 + \mathcal{O} \left( \sum_i R_i - R \right), \quad (3.2.28)$$

i.e., that the oscillations only occur close to contact discontinuities, and weaken when a contact discontinuity becomes increasingly smeared. A numerical experiment in section 3.5.3 will demonstrate this using advection of a contact wave as an example.

In summary, since pressure oscillations can not be removed without loss of robustness, which has been a major design goal for the SEC solver, and since pressure oscillations are a self-weakening phenomenon, it has been decided not to address the issue and stick with the unmodified HLLE solver.

### 3.2.3. A Note on Larroutrou's Positivity Correction

In [50], Larroutrou addresses the issue of positivity of mass fractions for Godunov-type numerical schemes. He shows that the multicomponent Roe solver is not guaranteed to preserve positivity of the mass fractions and suggests, as a general approach applicable to any Godunov-type scheme, to enforce the relation

$$f_Y(\mathcal{W}(0)) = f_\rho(\mathcal{W}(0)) \cdot \begin{cases} Y_\ell & \text{if } f_\rho(\mathcal{W}(0)) > 0, \\ Y_r & \text{if } f_\rho(\mathcal{W}(0)) < 0, \end{cases} \quad (3.2.29)$$

where by  $\mathcal{W}$  he denotes the solution to the Riemann problem. This relation is valid for the exact solution to the Riemann problem, and by replacing the numerical species mass fluxes with fluxes according to this formula, any scheme that preserves density positivity obviously also preserves positivity of mass fractions.

It has been shown in section 3.2.1 that the HLLE solver already is positivity preserving, so this issue does not affect the solver. If this fact is not known, however, the similarity of the HLLE solver to Roe's solver [26] and Larroutuou's choice of words make it tempting to use his approach for the HLLE solver as well.

The author showed in [10] that this makes the pressure oscillation issue worse, and is hence not advisable for HLL-type solvers: By theorem 3.2.1, the HLLE solver is capable of maintaining pressure equilibria at stationary contact discontinuities if temperatures and pressure are equal on both sides of the discontinuity. Larroutuou's correction replaces the species (diffusion) flux with upwinding, and since the energy flux is not adjusted accordingly, the equilibrium is disturbed and pressure oscillations arise as the species diffuse.

It is the lack of an energy flux adjustment which disturbs (temperature) equilibria, not the replacement of diffusion with upwinding: Einfeldt, in his stability analysis, writes the HLLE flux as

$$\frac{1}{2}(f(q_\ell) + f(q_r) - Q(q_r - q_\ell)), \quad (3.2.30)$$

with a suitable numerical viscosity matrix  $Q$ , *i.e.*, as a variant of the Lax-Friedrichs method [53] with reduced numerical diffusion. Using this formulation and applying Larroutuou's correction exclusively to the flux average does stabilize stationary contact discontinuities — but only because the species fluxes vanish anyway. At moving discontinuities, the issue persists.

Consequently, this argument applies in general to all solvers that do not yield the exact flux at interfaces: Larroutuou's correction decouples the fluxes of energy and species, hence changes how the energy flux affects temperature and pressure, and hence disturbs temperature equilibria.

### 3.3. Extension of the HLLEM Solver to Ideal Gases

Using the idea quoted above, namely that contact discontinuities don't physically exist, but should be replaced by a transition layer, Einfeldt extended the HLLE solver with a linear approximation to the contact discontinuity: In his extension, one uses the left eigenvector of the perfect gas Euler equation's gradient matrix corresponding to the contact wave,

$$\ell_2 = \begin{pmatrix} 1 - \frac{\gamma-1}{2} \frac{\bar{u}^2}{\bar{c}^2} \\ (\gamma-1) \frac{\bar{u}}{\bar{c}^2} \\ \frac{1-\gamma}{\bar{c}^2} \end{pmatrix} \quad (3.3.1)$$

to project the jump  $(q_r - q_\ell)$  onto the corresponding right eigenvector

$$r_2 = \begin{pmatrix} 1 \\ u \\ \frac{1}{2}u^2 \end{pmatrix}, \quad (3.3.2)$$

and then inserts the wave as a linear growth into the star region, scaled such that the total growth from left to right inside the region corresponds to the jump through the approximated wave and aligned such that the total integral over the star region does not change, *i.e.*, that the conservation law still holds:

$$\omega = \begin{cases} q_\ell & \text{for } x/t < b^\ell, \\ q^* + \delta(x - \bar{u}t)(\ell_2 \cdot (q_r - q_\ell)) r_2 & \text{for } b^\ell < x/t < b^r, \\ q_r & \text{for } b^r < x/t. \end{cases} \quad (3.3.3)$$

In the formulae,  $\bar{u}$  and  $\bar{c}$  are approximations to velocity and sound speed in the star section based on the numerical signal velocities,

$$\bar{u} = \frac{b_r + b_\ell}{2}, \quad (3.3.4)$$

$$\bar{c} = \frac{b_r - b_\ell}{2}, \quad (3.3.5)$$

and  $\delta$  is a constant for which Einfeldt derived the expression

$$\delta = \frac{1}{\Delta t} \frac{1}{\bar{c} + |\bar{u}|} \quad (3.3.6)$$

in a stability discussion. Eventually, one arrives at the formula

$$f^* = \frac{b_r f(q_\ell) - b_\ell f(q_r) + b_\ell b_r (q_r - q_\ell)}{b_r - b_\ell} - b_\ell b_r \frac{1}{2(\bar{c} + |\bar{u}|)} (\ell_2 \cdot (q_r - q_\ell)) r_2 \quad (3.3.7)$$

for the updated numerical flux. Details of the derivation can be found in [26].

Einfeldt's argument for the choice of  $\delta$  does not use specifics of the perfect gas case and applies to the ideal gas case as well. The projection must however be adapted. The eigenspace associated with the  $u$  eigenvalue of gradient matrix  $A$  in conservation form (eq. (3.3.10)) is spanned by the vectors

$$\begin{pmatrix} 1 \\ u \\ -\frac{1}{\gamma-1} \partial p / \partial \rho + u^2 \\ 0 \end{pmatrix} \text{ and } \begin{pmatrix} 1 \\ u \\ 0 \\ \frac{1}{\partial p / \partial \rho Y} (-\partial p / \partial \rho + u^2(\gamma-1)) \end{pmatrix}, \quad (3.3.8)$$

with corresponding left eigenvectors

$$\begin{pmatrix} u^2 - H \\ -u \\ 1 \\ 0 \end{pmatrix} \text{ and } \begin{pmatrix} -Y \\ 0 \\ 0 \\ 1 \end{pmatrix}. \quad (3.3.9)$$

In both equations (3.3.8) and (3.3.9), the second vector symbolically represents one vector per species; each one is non-zero in exactly one of the dimensions associated with the species mass fractions. Since the construction of the HLLEM solver ensures conservation and the fix does not affect the signal speeds, the primitive formulation from eq. (3.1.15) may be used as well to calculate the correct projection. This removes the computational effort of calculating the  $p$  derivatives, but requires to convert the projection to conservation form, which is computationally expensive as well.

In contrast to Einfeldt's perfect gas variant, the eigenspace depends on the thermodynamic state, not the numerical signal velocities alone. There are two obvious choices for the state at which to evaluate the eigenvectors: The first option is to use the upwind state, with the upwinding direction given by the sign of the mass flux in the HLLE solver, which is already known at the point where this correction is calculated. The other option is to use  $q^*$ . This does not pose additional calculation overhead, because  $q^*$  is required anyway to ensure positivity:

It has been shown in section 3.2.1 that  $q^*$  is positive, and it is known that a convex combination of positive states preserves positivity. In general, however, the introduction of the smeared contact wave into the star region breaks positivity. To retain it, the slope of the smeared wave must be limited such that the boundaries of the star region in eq. (3.3.3) remain positive. Since the  $Y$  components in eq. (3.3.8) are not available analytically in general, this must be done numerically.

Either choice offers an improvement over the uncorrected HLLE solver in regions of smooth flow. At contact discontinuities, however, the scheme suffers from the same issues as have been discussed in section 3.2.3 on Larrouturou's correction: Since the eigenvectors used for the projection in general cannot represent the jump in the internal energy correctly, the changes in species and energy do not match, and the correction therefore introduces temperature and pressure oscillations, rendering the straightforward extension of the HLLEM solver to the ideal gas case impractical for the SEC use case. In the following, two alternatives will be presented.

### 3.3.1. HLLEM for the Single-Species Case

An obvious solution to the issue is to use the HLLEM solver only in regions of small concentration gradients. With this ansatz, under the assumption that small changes in concentration have negligible effect on the energy, a simplified set of eigenvectors may be used:

For single component, ideal gas systems, the gradient matrix in the linearization from eq. (3.3.10) reduces to

$$A = \begin{pmatrix} 0 & 1 & 0 \\ -u^2 + \partial p / \partial \rho & (3-\gamma)u & \gamma-1 \\ u \partial p / \partial \rho - uH & H - (\gamma-1)u^2 & \gamma u \end{pmatrix}, \quad (3.3.10)$$

with

$$\frac{\partial p}{\partial \rho} = (\gamma - 1) \frac{1}{2} u^2 - (\gamma - 1) e + RT. \quad (3.3.11)$$

Associated with the  $u$  eigenvalue are eigenvectors

$$\ell_2 = \begin{pmatrix} -H + u^2 \\ -u \\ 1 \end{pmatrix} \quad (3.3.12)$$

and

$$r_r = \begin{pmatrix} 1 \\ u \\ u^2 - \frac{1}{\gamma-1} \frac{\partial p}{\partial \rho} \end{pmatrix} = \begin{pmatrix} 1 \\ u \\ \frac{1}{2} u^2 + \frac{RT}{\gamma-1} - e \end{pmatrix}. \quad (3.3.13)$$

This is almost the perfect gas case, the only difference is the term

$$RT - (\gamma - 1) e \quad (3.3.14)$$

quantifying how much the equation of state differs from a perfect gas equation.

The considerations for the state at which the eigenvectors should be evaluated that have been made above apply to this case as well.

### 3.3.2. Reusing the Perfect Gas HLLEM Solver

The HLLEM-solver variant from section 3.3.1 is valid in regions of smooth concentrations. In the context of the SEC simulation, it is an option to furthermore assume that in regions where concentrations are smooth, temperature changes are moderate as well: Steep temperature changes are associated with either strong pressure waves or under-resolved auto-ignition waves. The former occur at detonation fronts which are a sign of failure in SEC simulations anyway, the latter have steep concentration changes as well. Moderate temperature changes leave the isentropic exponent  $\gamma$  unchanged, and so the perfect gas case derived by Einfeldt may be used as an approximation: If the difference in  $\gamma$  between left and right states and  $q^*$  is small, then the solution to the local Riemann problem is close to the solution for the perfect gas case. This holds even if the concentrations differ. Hence, it is feasible to calculate the projection as

$$\ell_2 \cdot \begin{pmatrix} \rho_r - \rho_\ell \\ (\rho u)_r - (\rho u)_\ell \\ \frac{p_r - p_\ell}{\gamma^* - 1} + \frac{1}{2} \rho_r u_r^2 - \frac{1}{2} \rho_\ell u_\ell^2 \end{pmatrix} \begin{pmatrix} r_2 \\ Y^* \end{pmatrix} \quad (3.3.15)$$

with Einfeldt's eigenvectors  $\ell_2$  and  $r_2$  from eq. (3.3.1) and eq. (3.3.2).

## 3.4. The Complete SEC Solver

The choice of a suitable integrator for chemical kinetics has been discussed in section 2.4. A numerical scheme for the fluid dynamics part of the equation has been devised in this chapter. To combine both into a complete, second-order accurate solver, only minor details are missing:

### 3.4.1. Higher Order Reconstruction

The Godunov-type method derived above is a first-order method. To achieve second order, a MUSCL-Hancock scheme [72, 73] (short for *Monotonic Upstream-Centered Scheme for Conservation Laws*) is employed: The zeroth order approximation to the states at cell boundaries that enter the Riemann problem is replaced by a spatio-temporal linear interpolation, where time derivatives are evaluated by transforming them to spatial derivatives using the differential equation. To avoid oscillations near discontinuities, the slope of the interpolation is limited by comparing adjacent slopes using a *limiter*. This ansatz is well established in the community and so only implementation details specific to the present use case will be presented here. For a thorough introduction, see [71, chap. 14.4].

Reconstruction variables have been chosen based on the required computational effort: It is inexpensive to evaluate the energy equation (1.2.10), but a Newton solver is in general required to solve the inverse relation for temperature. Therefore, the primitive variables  $p$ ,  $u$ ,  $T$  and  $Y$  are used for reconstruction. Another advantage of this choice is that measures to prevent oscillations in discontinuous regions affect the temperature field directly. The temporal derivatives of the primitive variables can be expressed in terms of spatial derivatives as

$$\frac{\partial p}{\partial t} = -RT \left( u \frac{\partial \rho}{\partial x} + \rho \frac{\partial u}{\partial x} \right) + \rho R \frac{\partial T}{\partial t} + \rho T \frac{\partial R}{\partial t}, \quad (3.4.1)$$

$$\frac{\partial u}{\partial t} = -u \frac{\partial u}{\partial x} - \frac{1}{\rho} \frac{\partial p}{\partial x}, \quad (3.4.2)$$

$$\frac{\partial T}{\partial t} = \frac{1}{\rho c_v} \left( -p \frac{\partial u}{\partial x} - \rho u c_v \frac{\partial T}{\partial x} - \frac{1}{2} u \frac{\partial p}{\partial x} \right), \quad (3.4.3)$$

$$\frac{\partial Y}{\partial t} = -u \frac{\partial Y}{\partial x}, \quad (3.4.4)$$

with

$$\frac{\partial \rho}{\partial x} = \frac{1}{RT} \frac{\partial p}{\partial x} - \frac{p}{RT^2} \frac{\partial T}{\partial x} - \rho M \sum_i \frac{1}{M_i} \frac{\partial Y_i}{\partial x}, \quad (3.4.5)$$

$$\frac{\partial R}{\partial t} = \hat{R} \sum_i \frac{1}{M_i} \frac{\partial Y_i}{\partial t}. \quad (3.4.6)$$

The reconstructed slopes are limited using the Monotonized Central-Difference (MC) limiter (e.g., [53]).

For higher orders, ENO reconstruction [40] is implemented up to fourth order. ENO is short for *Essentially Non-Oscillatory Scheme*. The basic idea of this reconstruction method is to interpolate using multiple different stencils of varying size, and use the one that gives the smoothest interpolant.

Since the MC limiter is *total variation diminishing*, it is likely that positivity is preserved in the second-order scheme. Still, note that the proof of positivity in section 3.2.1 formally only holds for the first-order scheme.

### 3.4.2. Operator Splitting

To integrate the two solvers — one for gas dynamics, one for chemical kinetics — into a single code, *Strang splitting* [69] has been employed. This fractional step method numerically solves differential equations of the form

$$\frac{\partial x}{\partial t} = \mathbf{A}(x) + \mathbf{B}(x) \quad (3.4.7)$$

by evaluating

$$x_{n+1} := \Phi^A\left(\frac{\Delta t}{2}\right)\Phi^B(\Delta t)\Phi^A\left(\frac{\Delta t}{2}\right)x_n, \quad (3.4.8)$$

where  $\Phi^A$  is any second-order accurate numerical scheme solving the subproblem  $\partial x / \partial t = \mathbf{A}(x)$ , and  $\Phi^B$  respectively. Strang proved the validity and second-order accuracy of his approach by Taylor-expanding the solution to the original problem,

$$x(t) = x(0) + t(\mathbf{A}(x) + \mathbf{B}(x)) + \frac{t^2}{2}(\nabla \mathbf{A}(x) + \nabla \mathbf{B}(x)) \cdot (\mathbf{A}(x) + \mathbf{B}(x)) + \mathcal{O}(t^3), \quad (3.4.9)$$

and comparing coefficients with the expansion of his scheme,

$$x_{n+1} = \Phi^A\left(\frac{\Delta t}{2}\right)\Phi^B(\Delta t)\left(x_n + \frac{\Delta t}{2}\mathbf{A}(x_n) + \frac{\Delta t^2}{8}\nabla \mathbf{A}(x_n) \cdot \mathbf{A}(x_n) + \mathcal{O}(\Delta t^3)\right) \quad (3.4.10)$$

$$\begin{aligned} &= \Phi^A\left(\frac{\Delta t}{2}\right)\left(x_n + \Delta t \frac{\mathbf{A}(x) + 2\mathbf{B}(x)}{2} + \frac{\Delta t^2}{8}(\nabla \mathbf{A}(x) \cdot \mathbf{A}(x) + \right. \\ &\quad \left. 4\nabla \mathbf{B}(x) \cdot (\mathbf{A}(x) + \mathbf{B}(x))) + \mathcal{O}(\Delta t^3)\right), \end{aligned} \quad (3.4.11)$$

finding that the expressions match to second order.

Derivations of higher order splitting schemes in the literature usually invoke “heavy machinery”: E.g., [80] uses the *Baker–Campbell–Hausdorff formula* from Lie algebra theory, [36] discusses *Butcher series trees* from the analysis of Runge–Kutta methods. It is noteworthy that Strang’s simple analysis method can be used to provide further results as well: By performing Strang’s calculation using variable coefficients, it can be shown that Strang splitting is the *only* second-order accurate scheme among all schemes of the form

$$x_{n+1} = \Phi^A(\alpha_1 \Delta t)\Phi^B(\beta_1 \Delta t)\Phi^A(\alpha_2 \Delta t)x_n. \quad (3.4.12)$$

The solution strategy for obtaining the correct values for the coefficients  $\alpha_i$  and  $\beta_i$  is to work from low to high order, *i.e.*, first fix the coefficients such that the Taylor expansions of eq. (3.4.9) and eq. (3.4.12) agree to first order, and then use the remaining degree of freedom to ensure second order accuracy.

The same ansatz works in general for higher orders by Taylor-expanding the ansatz

$$x_{n+1} = \left( \prod_i^N \Phi^A(\alpha_i \Delta t) \Phi^B(\beta_i \Delta t) \right) x_n, \quad (3.4.13)$$

and successively fixing the coefficients as above. Using a computer algebra system, the thesis' author found the coefficients

$$\alpha_1 = 1, \quad \beta_1 = -\frac{1}{24}, \quad (3.4.14)$$

$$\alpha_2 = -\frac{2}{3}, \quad \beta_2 = \frac{18}{24}, \quad (3.4.15)$$

$$\alpha_3 = \frac{2}{3}, \quad \beta_3 = \frac{7}{24} \quad (3.4.16)$$

for a fourth-order accurate scheme, and the coefficients

$$\alpha_1 = \frac{2^{\frac{2}{3}}}{12} + \frac{\sqrt[3]{2}}{6} + \frac{1}{3}, \quad \beta_1 = \frac{2^{\frac{2}{3}}}{6} + \frac{\sqrt[3]{2}}{3} + \frac{2}{3}, \quad (3.4.17)$$

$$\alpha_2 = -\frac{\sqrt[3]{2}}{6} - \frac{2^{\frac{2}{3}}}{12} + \frac{1}{6}, \quad \beta_2 = -\frac{2\sqrt[3]{2}}{3} - \frac{2^{\frac{2}{3}}}{3} - \frac{1}{3}, \quad (3.4.18)$$

$$\alpha_3 = -\frac{\sqrt[3]{2}}{6} - \frac{2^{\frac{2}{3}}}{12} + \frac{1}{6}, \quad \beta_3 = \frac{2^{\frac{2}{3}}}{6} + \frac{\sqrt[3]{2}}{3} + \frac{2}{3}, \quad (3.4.19)$$

$$\alpha_4 = \frac{2^{\frac{2}{3}}}{12} + \frac{\sqrt[3]{2}}{6} + \frac{1}{3}, \quad \beta_4 = 0 \quad (3.4.20)$$

for a fifth-order accurate scheme. Higher orders contain too many terms to be treated in this fashion using current hardware. Both schemes involve negative time steps. In [56], it is shown that this is generally the case for higher order splitting methods, and that the negative timesteps degrade the scheme's stability properties. Additionally, while the methods are formally of high order, the error in practice exceeds the Strang splitting error unless impractically small time steps are used. Other means to achieve higher order, such as extrapolation methods [22] or deferred correction methods (*e.g.*, [25]), should therefore be preferred.

An application of this idea is employed in the 2D/3D extension of the SEC simulation. It uses operator splitting to solve each dimension separately using the theory developed above. Following the arguments from this section, extrapolation is employed if higher than second order in time is desired: The code in each time step first solves the problem for a full time step  $\Delta t$  given by the CFL condition. It then solves the *same* problem again multiple times, using time steps of at most  $\Delta t/n$ , with increasing  $n$ . The solution is then extrapolated towards  $n \rightarrow \infty$ , which formally gives a higher order approximation. It is

noteworthy that while this approach is well suited for spatial splitting, splitting of fluid dynamics and chemical kinetics does not work well with extrapolation due to the explicit nature of extrapolation and stiffness of most problems from chemical kinetics. Deferred correction, on the other hand, achieves the higher order by formulating an expression for the error as an ODE, solving it and then updating the approximation using the error term. This admits the use of implicit methods and is hence better suited for this application.

### 3.4.3. Program Flow

The complete algorithm is as follows:

1. Apply problem specific boundary conditions by adding ghost cells.
2. Estimate an appropriate time step size  $\Delta t$  using the CFL condition and, optionally, the states' reaction rates.
3. Invoke the chemical kinetics solver:
  - a) Solve the energy equation eq. (1.2.10) for temperature using a Newton solver.
  - b) Advance the chemical kinetics system  $\partial Y / \partial t = \dot{Y}_{\text{chem}}$  by  $\Delta t/2$  using RADAU15, as per the argument of section 2.4. The equation system is a Differential Algebraic System (DAE), conserving the total energy including the enthalpy of formation  $e_0(Y)$ . The required temperature change for energy conservation can be calculated explicitly, resulting in another equation for  $\partial T / \partial t$ .
  - c) Compute the updated energy using eq. (1.2.10).
  - d) Compute the updated pressure using the equation of state eq. (1.2.8).
4. (*optional*) In the quasi-1D case with axial variations as introduced in section 1.2.4, multiply the stored states by the associated volume's cross-sectional area and advance the source-term equation by  $\Delta t/2$  using a second-order solver. The required derivatives are available using the same technique as has been used for reconstruction in section 3.4.1.
5. For each spatial dimension, with the order of the steps permuted after each time step to achieve Strang splitting, consider the 1D subproblem and repeat:
  - a) Reconstruct limited cell boundary states using the spatio-temporal reconstruction from section 3.4.1.
  - b) Compute inter-cell fluxes using the ideal-gas HLLEM scheme from section 3.3; if the selected variant of the scheme requires to know  $q^*$ , then this involves another computation of the primitive variables using a Newton solver.
  - c) Update the states to the  $\Delta t$  time level.
  - d) (*optional*) If more than one spatial dimension is present, update the primitive variables by solving the energy equation eq. (1.2.10).

6. (optional) If axial variations as introduced in section 1.2.4 are present, advance the source-term equation by another  $\Delta t/2$  step and divide by the cross-sectional area again.
7. Perform another  $\Delta t/2$  time step using the chemical kinetics solver.

Appendix B gives an introduction to the actual implementation, which differs slightly in detail.

## 3.5. Validation

To show that the approach is valid, in this section, various test cases are discussed. They were selected based on the possible issues that have been identified above and should cover all aspects relevant to one-dimensional SEC simulations.

### 3.5.1. Shock Tube

For the Riemann problem from section 3.1, an analytical solution is known. Since its solution is one of the building blocks of the solver, it presents a good test case to evaluate the quality of the approximate Riemann solver, reconstruction, and limiting. Sod introduced this test case in 1978 for perfect gases [68], and it has since become one of the essential test cases for every numerical scheme in computational fluid dynamics. In [3], the authors introduced a multi-species variant of the test to demonstrate that their in conservative scheme for perfect gas mixtures outperforms a Roe solver with Superbee limiter. They note:

Results by the conservative scheme [...] are oscillatory near the contact, and while they eventually converge to zero with mesh refinement, they do so very slowly. Note also that increasing the order of accuracy of the scheme does not improve the quality of the results of the conservative scheme.

An ideal gas variant of their test case is the Riemann problem

$$q_\ell = (T = 300 \text{ K}, p = 10 \text{ bar}, Y = \text{N}_2, u = 0), \quad (3.5.1)$$

$$q_r = (T = 345 \text{ K}, p = 1 \text{ bar}, Y = \text{Ar}, u = 0). \quad (3.5.2)$$

At the given temperature, the associated isentropic exponents  $\gamma$  are 1.4 for the Nitrogen and 1.66 for the Argon. The original test uses 1.4 and 1.6, respectively. The original study states that 200 grid points and a CFL number of 0.8 were used. Given their results, this translates to 0.1 ms simulation time at 1 mm grid resolution. Their choice of CFL number is reused as well, though this choice is not expected to work in general with the present scheme.

In fig. 3.5.1, it can be seen that the scheme does not exhibit the issues observed in the other study. This confirms the insight from section 3.2.2: Pressure oscillations naturally occur at sharp contact discontinuities with shock-capturing schemes. A scheme that

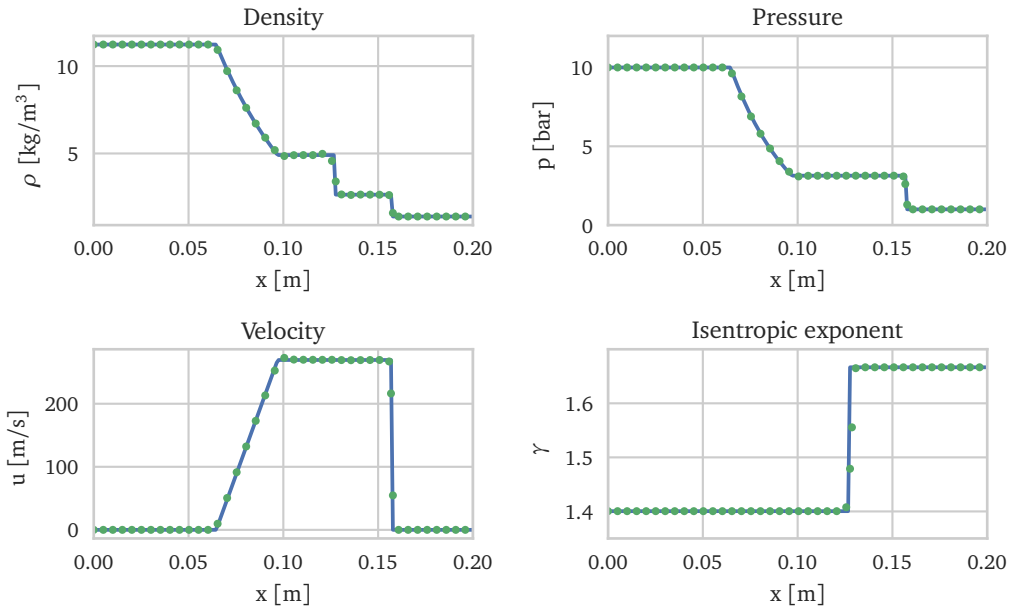


Figure 3.5.1.: Multi-species shock tube test case with HLLEM solver from section 3.3.1, MC limiter and MUSCL reconstruction. The blue, solid line is the exact solution, the data points show the numerical solution.

quickly diffuses the discontinuity introduces less oscillations. The HLLEM solver with MC limiter does just that. The Roe solver used by the cited study, on the other hand, tries to maintain the contact wave. The use of the Superbee limiter does even steepen smeared out regions again [53, sec. 6.9], and thereby ensures that the problem persists.

### 3.5.2. Moving Contact Wave

The study [3] has a second interesting test case in the light of the discussed pressure oscillations: They simulate a contact wave separating two gases at different densities  $\rho_\ell = 0.1$ ,  $\rho_r = 1$ , with isentropic exponents  $\gamma_\ell = 1.4$ ,  $\gamma_r = 1.6$  and moving right with a Mach number of  $M = 0.85$  if calculated with respect to the right gas.<sup>2</sup>

From the discussion of the test case in section 3.2.2 it is to be expected that a simulation with numerical diffusion creates an initial pressure peak close to

$$p_\infty = \frac{(\gamma_\ell - 1)^{-1} + (\gamma_r - 1)^{-1}}{2} \left( \frac{\rho_\ell \gamma_\ell + \rho_r \gamma_r}{\rho_\ell + \rho_r} - 1 \right) p_0 \approx 1.45 p_0, \quad (3.5.3)$$

the pressure equilibrium at  $t = \infty$  if the system had diffusion. This pressure peak is expected to quickly diminish into a weak shock. It is the point of this test case to show

<sup>2</sup>Their description of the test case and their plots do not match. This test case follows their calculation, not their description.

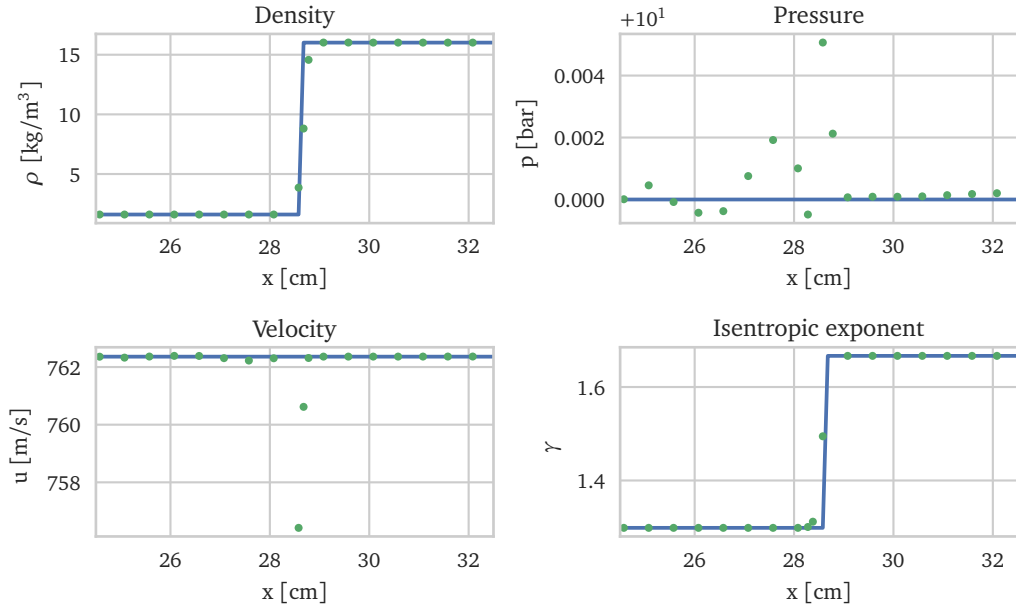


Figure 3.5.2.: Multi-species moving contact wave test case with HLLEM solver from section 3.3.1, MC limiter and MUSCL reconstruction. The blue, solid line is the exact solution, the data points show the numerical solution.

that these pressure oscillations, which are of the same magnitude as the ones [3] finds for conservative solvers at short times and which produce the predicted peak pressure, do indeed become increasingly negligible for larger times. Hence, the simulation was conducted for 5 times their simulation time. In fig. 3.5.5, a close-up view on the contact wave is shown 780 time steps into the simulation. The wave clearly moves with the right velocity, and while pressure oscillations are still present, they are limited to an acceptable relative error of  $6 \cdot 10^{-4}$ . As a consequence, a small local velocity error is present as well.

The initial shock (not visible in the plot) does at this point still have a magnitude of 0.4 bar, rendering it the worst source of error. Since it occurs only for discontinuous initial conditions though, and not if the transition is smooth, it is an acceptable trade-off to leave it unfixed.

### 3.5.3. Advection of Smooth Data

To further substantiate the claim that pressure peaks resulting from contact waves as in section 3.5.2 are small enough to ignore them for the purposes of this solver, consider the advection problem for three 3000 K peaks within a 300 K  $\text{N}_2$  mixture at 1 bar pressure. This temperature difference corresponds to the jump in the previous example. The first peak has a continuous triangular shape, the center is a discontinuous plateau, where the largest errors are to be expected, and the third one is a smoothed plateau with contin-

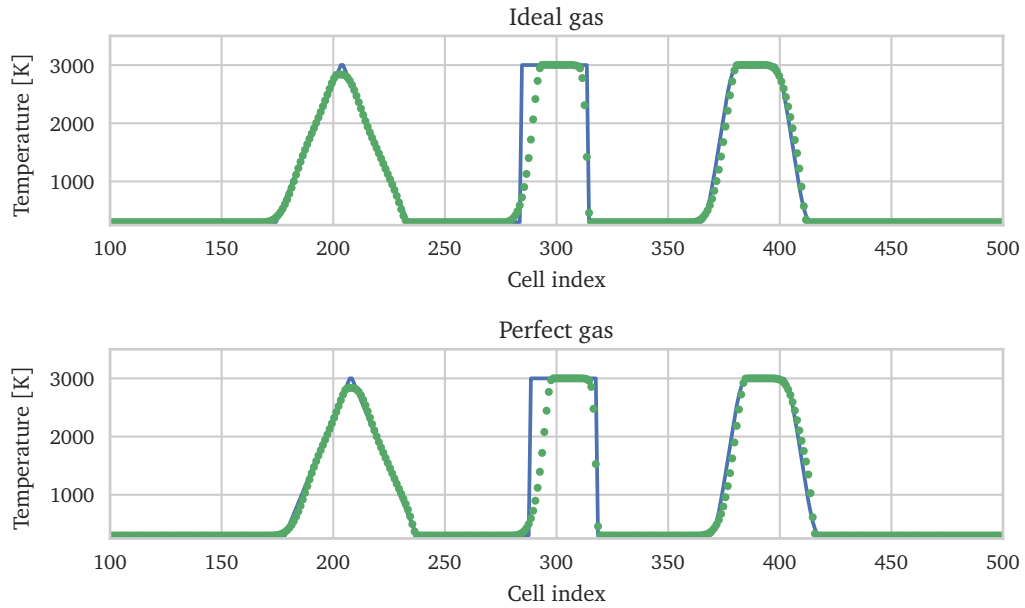


Figure 3.5.3.: Advection problem for ideal and perfect gases compared after 2000 time steps.

uous first derivative. Figure 3.5.3 compares the temperature profiles of the simulation with an ideal gas equation of state and the perfect gas approximation at  $cfl = 0.5$  after 2000 time steps. No qualitative difference can be observed between ideal and perfect gas case, so the pressure fluctuations in the ideal gas case do indeed not pose a problem.

The asymmetry in the solution comes from an interaction of the contact wave approximation in the HLLEM solver with the MC limiter. If the unmodified HLLE scheme or a more diffusive limiter like the minmod function is used, then the result is symmetric. However, the contact wave is smeared just like it would be in the first order scheme, and such smearing of waves is accepted in the present scheme. The end that is not smeared does not pose an issue either, because the code disables the correction if the gases differ too much in their composition and temperature oscillations could occur. The asymmetry itself is not considered a problem. Still, this phenomenon is worth further investigation, because if it yields a way to restore symmetry in favor of the solution that is less smeared, then the resulting scheme would have increased accuracy.

### 3.5.4. Vacuum Test Case

In section 3.2.1, it has been shown that the ideal-gas HLLEM solver ensures positivity, and should therefore be able to handle vacuum-generating problems by adding just the right amount of diffusion for density and pressure to remain positive.

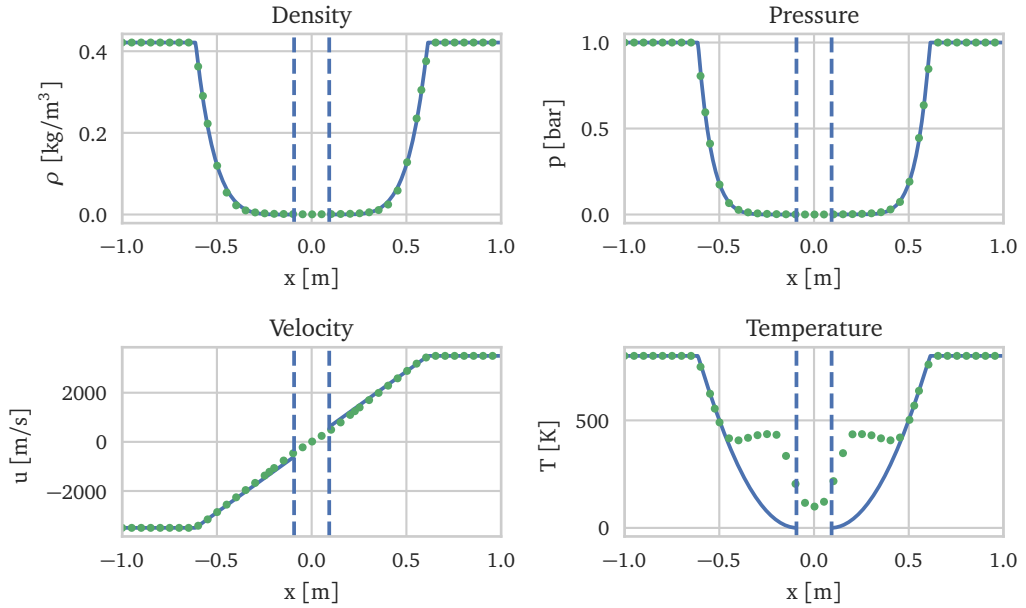


Figure 3.5.4.: Solution for a Riemann problem generating vacuum. The blue line is the exact solution, with the dashed vertical line marking the boundary of the vacuum zone. The green dots are the numerical solution.

In [71], the author describes how to calculate the solution to the vacuum generating Riemann problem: He proves that a vacuum region cannot be adjacent to a shock. Hence, the problem must have a two-rarefaction solution. Both rarefaction waves eventually reach zero pressure towards the center. Using the Riemann invariant (3.1.26), a corresponding velocity can be determined, and this velocity determines the speed with which the vacuum region expands. For perfect gases, the invariant admits an explicit expression. Using it, the inequality

$$\frac{2c_\ell}{\gamma-1} + \frac{2c_r}{\gamma-1} \leq u_r - u_\ell \quad (3.5.4)$$

can be derived as a condition for a vacuum generating Riemann problem.

For  $\text{N}_2$  at 800 K and 1 bar, by this formula, a velocity difference of 6310 m/s is sufficient for vacuum creation. To be on the safe side,

$$u_\ell = -3500 \text{ m/s}, \quad u_r = 3500 \text{ m/s} \quad (3.5.5)$$

were chosen here. Figure 3.5.4 shows that the code handles the test case like it would handle a near-vacuum case, with the velocity field being that of two touching rarefaction fans. The erroneous temperature in the lower right plot is a visible artifact of the correction term (3.2.19): The correction prevents a numerical vacuum state, and the accuracy of the choice of  $\gamma_{\max}$  determines how close to zero energy a state may be. In this test case,  $\gamma_{\max} = 1.7$  was used. For  $\gamma_{\max} = 1.5$ ,  $T_{\min} \approx 50$  K. The theoretical bound

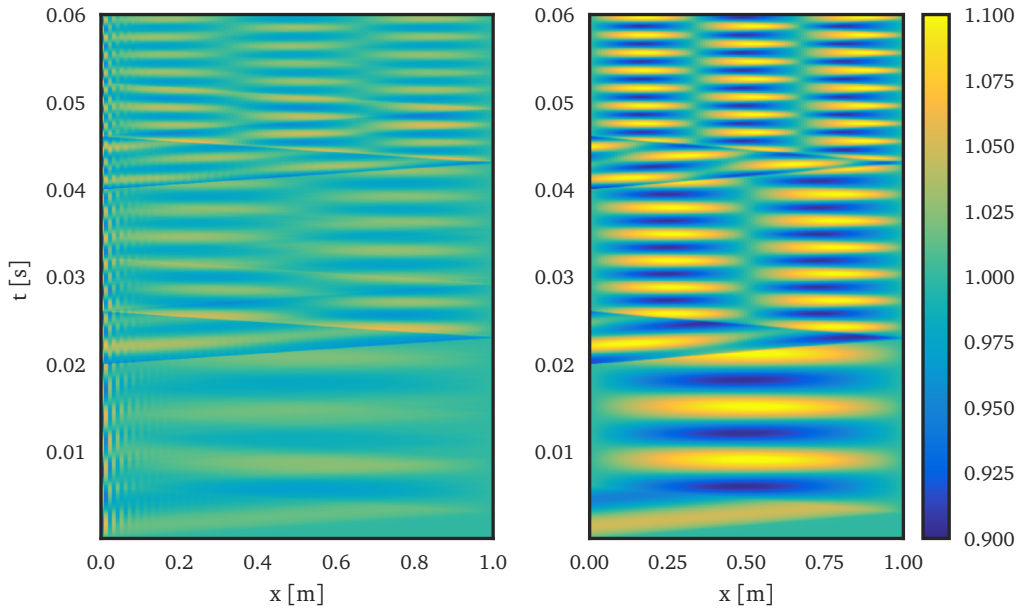


Figure 3.5.5.: Pressure streak-plot of forced oscillation in a pipe open at one end. The left simulation used the original HLLEM solver, the right one the modified, ideal gas HLLEM variant from section 3.3.2. Both plots share the same colormap.

for this example is  $\gamma_{\max} = 1.4005$ . This choice creates states that are too noisy for the Newton solver for the temperature/energy relation (1.2.10) though. The temperature error inside the rarefaction stems from the error at the solution's center.

### 3.5.5. Acoustic Test Case

Consider a clarinet, that is, a pipe with an open end and one where oscillations are enforced. If the excitation occurs at an eigenfrequency of the pipe, a standing wave is to be expected. If additionally the excitation is sufficiently strong, the jump between the numerical ghost cell enforcing the boundary condition and the first interior cell is sufficiently large for projection errors in the HLLEM scheme to be expected. This makes this a good test case to show the issues of the uncorrected variant of the scheme, and that the fixes suggested in section 3.3 work.

In the calculation, a 1 m domain with a resolution of 1 cm was set up filled with O<sub>2</sub> at 300 K and 1 bar. At its left end, excitation with  $\pm 0.1$  bar was enforced, starting with the first eigenmode, with the frequency doubling every 20 ms.

Figure 3.5.5 compares the pressure fields of both simulations. The unmodified scheme exhibits oscillations at the forced end that significantly weaken the amplitude of the standing waves. All three of the suggested corrections, *i.e.*, upstream and star-region based

calculation of ideal-gas eigenvectors and proper perfect gas approximation, qualitatively produce the right plot without spurious oscillations.

### 3.5.6. Laval Nozzle Flow

The SEC simulation supports the quasi-1D formulation (1.2.64) of the reactive Euler system. A simple test for the adequacy of the operator splitting approach to axial variations is the simulation of choked flow through a convergent-divergent nozzle: For simplicity of this derivation, consider a gas obeying the perfect gas equation. Assume that a fixed upstream state with pressure  $p_u$  and enthalpy  $h_u$ , a downstream pressure  $p_d$ , and cross sectional area  $A(x)$  are given. Under the assumption that flow through the duct is isentropic, [6] derives

$$M_d^2 = \frac{2}{\gamma - 1} \left( \left( \frac{p_u}{p_d} \right)^{\frac{\gamma-1}{\gamma}} - 1 \right), \quad (3.5.6)$$

$$\dot{m} = \frac{\gamma p_u M_d}{\sqrt{(\gamma - 1) h_u}} \left( 1 + \frac{\gamma - 1}{2} M_d^2 \right)^{-\frac{\gamma+1}{2(\gamma-1)}} A_d \quad (3.5.7)$$

for the mass flow  $\dot{m}$ . For fixed  $p_u$ ,  $\dot{m}$  approaches a constant value as  $p_d \rightarrow p_c$ , for a specific limiting pressure  $p_c > 0$ . For pressures  $p_d \leq p_c$ , the mass flow remains constant, and locally  $M = 1$  at the throat. Such flows are called *choked*. Behind the throat, the flow becomes supersonic. As  $p_d$  further decreases, a stationary shock forms that returns the flow to subsonic velocities. The author of [6] argues that the total pressure ratio between up- and downstream must be due to this shock, and that therefore the total pressure ratio for the shock is known. From this, the local Mach number upstream from the shock can be obtained using shock relations. Results are available pre-calculated in literature in the form of *Normal shock tables*. Via the mass flow equation above, from this the cross sectional area at the shock can be obtained, and thus its position relative to the throat.

In the simulation,  $\gamma = 1.4$ ,  $p_u = 2$ ,  $p_d = 1$  and  $\rho_u = 0.0077$  were used, the density being the dimensionless pendant to  $O_2$ 's density at room temperature. The duct geometry is sketched in fig. 3.5.6. The above formulae predict that under these conditions, the flow is choked and a normal shock is positioned at  $x = 1.954$ . The simulation started off with  $p = p_d$  everywhere, and upstream conditions imposed via a fixed-state boundary condition. The calculation was then run with a resolution of  $\Delta x = 10^{-2}$  and  $cfl = 0.5$  until a numerical steady-state was reached. Figure 3.5.6 shows that the steady-state solution qualitatively agrees with the prediction.  $M = 1$  holds at the throat. The shock is positioned slightly off, at  $x = 1.83$ . This is due to the operator splitting approach favoring a numerical rather than the exact equilibrium. For  $cfl = 0.05$ , it has the correct position.

Qualitative behaviour of axial variations is hence well represented by the implementation, while to obtain quantitatively good results, small time steps or (splitting) methods of higher order are required; see section 3.4.2.

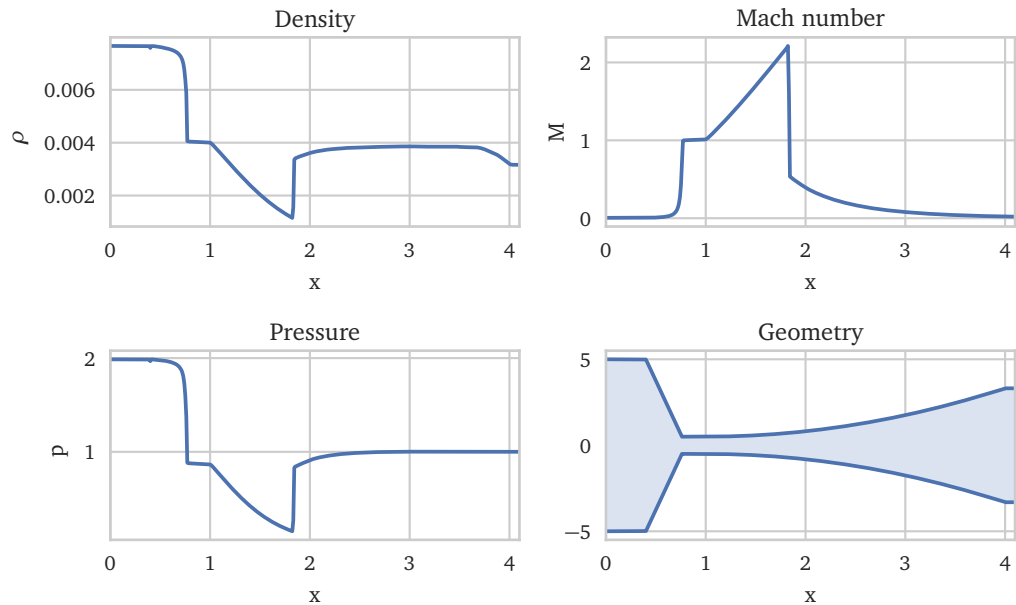


Figure 3.5.6.: Choked flow through a de Laval nozzle.

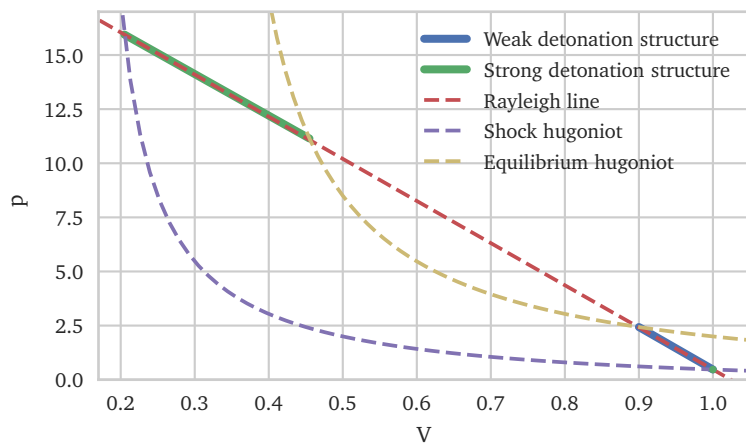


Figure 3.5.7.: Exemplary pressure/volume diagram for ZND detonations.

### 3.5.7. ZND Detonations

Detonations are explosions driven by a leading shock wave. They have been introduced in chapter 1 as a means to approximate CVC. From a theoretical viewpoint, their existence is justified by the ZND model, named after Yakov Borisovich Zel'dovich [82], John von Neumann [58], and Werner Döring [24], who independently proposed the model during World War 2 as an extension to an earlier model by David Chapman and Émile Jouguet. It enables calculation of the detailed structure of a detonation in a single dimension: The authors argue that in a coordinate system moving with the shock's velocity, a stable detonation is a stationary structure. This structure can be obtained as a solution for the stationary equations. For any detonation, a downstream state  $q_d$  for the detonation to travel into must be given. Furthermore, suppose for now that the shock speed  $u_s$  is known and define  $\tilde{u} = u - u_s$ . By eq. (1.2.7), for stationary solutions in the moving reference frame,

$$\frac{\partial}{\partial x} (\rho \tilde{u}) = 0, \quad (3.5.8)$$

$$\frac{\partial}{\partial x} (\rho \tilde{u}^2 + p) = 0, \quad (3.5.9)$$

$$\frac{\partial}{\partial x} (\tilde{u} (\rho E + p)) = 0, \quad (3.5.10)$$

$$\frac{\partial}{\partial x} (\rho Y \tilde{u}) = \rho \dot{Y}_{\text{chem}} \quad (3.5.11)$$

holds. Integration of these steady-state equations between two arbitrary points gives equations relating admissible jumps in the conserved quantities. In this context, the set of admissible jumps in momentum is called the *Rayleigh line* (after John William Strutt, 3<sup>rd</sup> Baron Rayleigh), which indeed is a line with a slope depending on the shock speed. The admissible jumps in energy are given by the *Hugoniot* (after Pierre-Henri Hugoniot). Two distinct integration bounds are of interest: The jump from the downstream state into the unreacted, post-shock *von Neumann* state, and the jump from the downstream state into the reacted, equilibrium *Chapman-Jouguet (CJ)* state. Since both conditions must hold for all flow, the structure of a detonation can be obtained by calculating intersections between downstream state, Rayleigh line and both Hugoniot curves. Figure 3.5.7 shows an example of a non-dimensional  $p/V$  diagram containing these lines for a detonation originating in the point (1, 1).

Note that the theory and plot do not only explain/contain strong detonations, but also the structure of a weak detonation that occurs in a SEC: It is the solution with a vanishing shock, directly connecting initial and equilibrium state through the Rayleigh line.

Computationally, to obtain the structure of a strong detonation, the jump conditions are only required to obtain the post-shock state  $q_u$  from  $q_d$ . From  $q_u$ , equations (3.5.8) to (3.5.11) may then be directly integrated towards equilibrium  $q_\infty$ . By translating back to the original reference frame, one finally obtains initial data which should, up to translation, be invariant under a numerical simulation of the reactive Euler equations.

A detonation hence poses another good challenge for operator splitting, only this time

not for integration of the geometric source term, but for integration of the chemical kinetics source term.

Since flow upstream from  $q_u$  is smooth, it is convenient to switch to a different coordinate system for determining the initial data. From equations (3.5.8) to (3.5.11), one can readily derive

$$\frac{\partial \rho}{\partial x} = \frac{1}{u^2} \frac{\partial p}{\partial x}, \quad (3.5.12)$$

$$\frac{\partial u}{\partial x} = -\frac{1}{\rho u} \frac{\partial p}{\partial x}, \quad (3.5.13)$$

$$\frac{\partial Y}{\partial x} = \dot{Y}_{\text{chem}}. \quad (3.5.14)$$

By a lengthy transformation of the energy equation, furthermore,

$$\frac{\partial p}{\partial x} = \frac{\sum_i ((\rho u T \hat{R} + u c_v p \hat{R}/R^2)^{1/\tilde{M}_i} - \rho u (\vec{h}_0)_i) \frac{\partial Y_i}{\partial x}}{\rho u c_v (1/\rho - p/(\rho u)^2)^{1/R} - p/(\rho u)}, \quad (3.5.15)$$

with species molar masses vector  $\vec{M}$  and enthalpies of formation vector  $\vec{h}_0$ , i.e., the sum is taken over all species in the system. The advantage of this formulation is that only two equations, the one for pressure and the one for the mass fractions, have to be numerically integrated, while the other variables can be evaluated using the jump conditions.

For the shock speed  $u_s$ , Chapman [19] and Jouguet [44] observed that the shock conditions impose a lower bound for admissible speeds, below which the conditions cannot be fulfilled from  $q_d$  to  $q_\infty$ . This limit velocity is called the *CJ detonation velocity*  $u_{\text{cj}}$ . The existence of a limit velocity is also visible in fig. 3.5.7, if one keeps in mind that the slope of the Rayleigh line depends on the shock speed: Below a certain slope, Rayleigh line and equilibrium Hugoniot do not meet anymore. Chapman and Jouguet argue that  $u_{\text{cj}}$  must be the “preferred” velocity of detonations. This becomes evident if one calculates the equilibrium velocity  $\tilde{u}_\infty$  relative to the shock: If  $u = u_{\text{cj}}$ , the velocity eventually becomes sonic and therefore isolates the lead shock from pressure waves emanating from somewhere further upstream. For larger shock speeds, on the other hand, relative equilibrium velocity is subsonic, and the system decays to the CJ detonation. In the test case of this section, this condition was used to determine  $u_s$  numerically, by means of an interval search algorithm solving  $\tilde{u}_\infty(u_s) = c_\infty$ . More elaborate algorithms outperforming this simple one exist, see [65]. For more details on ZND theory and the CJ condition, see, e.g., [30].

For the simulation,

$$q_d = (T = 550 \text{ K}, p = 7 \text{ bar}, \text{stoichiometric H}_2 \text{ in air}) \quad (3.5.16)$$

was chosen, and the hydrogen combustion model by [17] was used. The code determines the corresponding CJ velocity as  $1992.5 \text{ m/s}$ , which is slightly too large. This is due to error tolerances; with more stringent bounds, it arrives at  $1989.4 \text{ m/s}$  with an error in  $(\tilde{u}_\infty - c_\infty)$  of  $-37 \text{ m/s}$ . Due to the operator splitting, the simulation favors a numerical

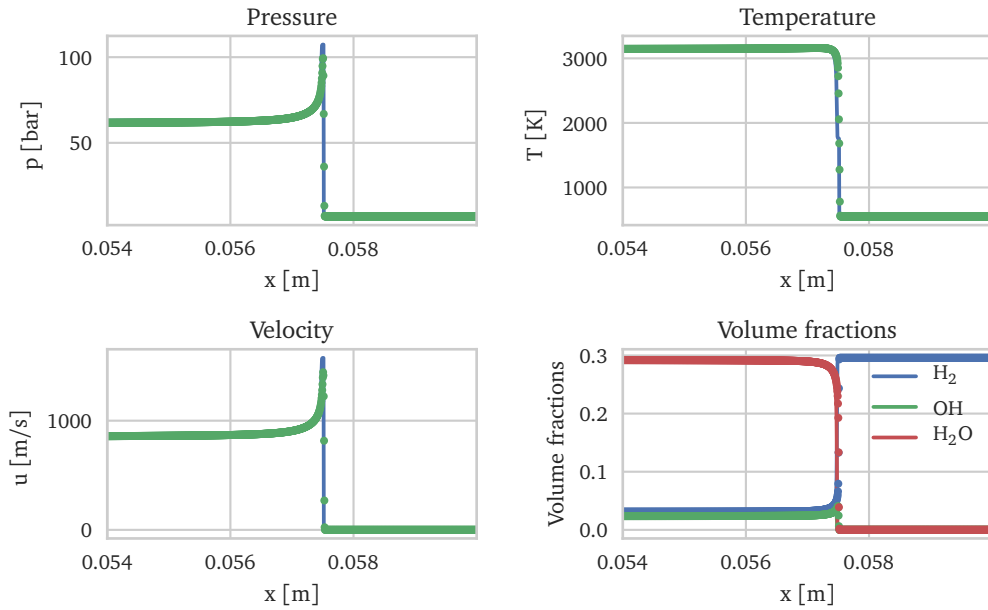


Figure 3.5.8.: Resolved ZND detonation after 20000 time steps. The straight lines show the predicted, circles the numerical solution.

CJ velocity that lies between the two, traveling with 1990 m/s. This velocity was used in this test, to allow better comparison between predicted and actual solution.

For reference, NASA's *Chemical Equilibrium with Applications* tool, a well tested code for thermodynamic calculations, determines  $u_{\text{cj}} = 1980 \text{ m/s}$ . This is most likely due to the simulation using a different thermodynamic database than NASA's tool. E.g., with Berkeley's GRI mechanism [67], the code estimates  $u_{\text{cj}} = 1984 \text{ m/s}$ .

The simulation was run with a resolution that resolves the leading shock ( $\Delta x = 5 \mu\text{m}$ ) for 20000 time steps, corresponding to roughly  $t = 30 \mu\text{s}$ . Figure 3.5.8 shows excellent agreement between predicted solution and simulation.

Another validation of the code using detonations has been performed by [38] in a bachelor's thesis for the PDC experiment in CRC 1029. The author obtained a detonation by using initial data containing a hotspot and running the simulation until a stable detonation had formed. He then compared a simulation of the time evolution of the detonation with the numerical results by [81]. Figure 3.5.9 shows that the propagation velocity of the detonation is in excellent agreement with the reference data. Individual emission levels deviate; the author attributes this to the use of a different reaction mechanism. Furthermore, [33] used a similar technique to simulate detonations using the code, with plausible results.

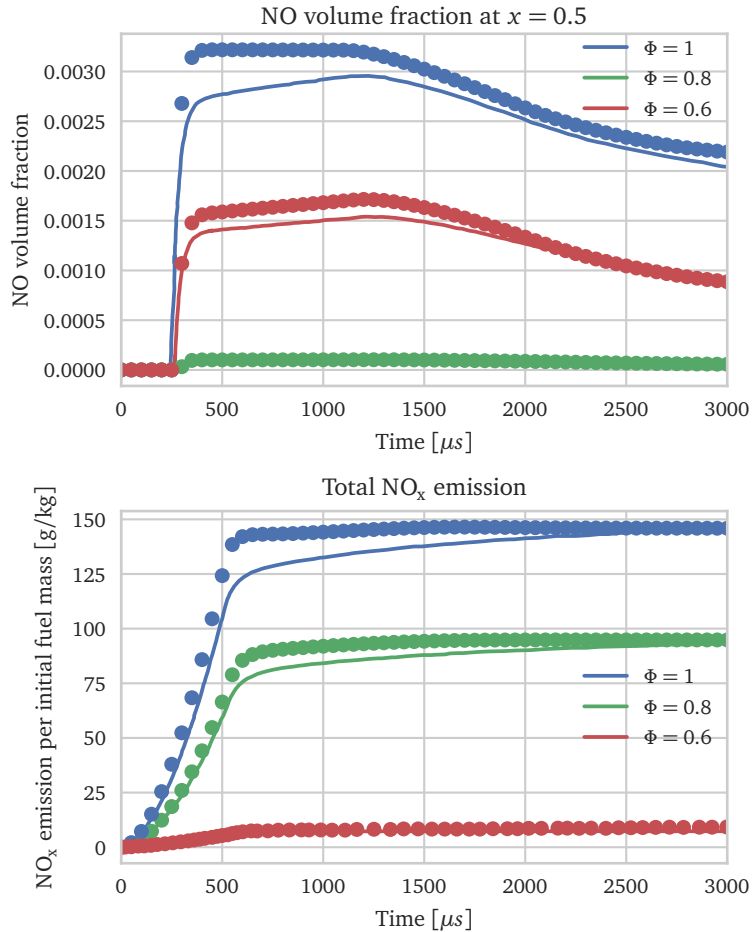


Figure 3.5.9.: NO<sub>x</sub> emission in a detonation. Solid lines are from the reference study [81], data points from the simulation using the SEC code. Figure reproduced from [38] courtesy of Niclas Hanraths.

### 3.6. Intermediate Conclusion

Common literature presents the construction of Riemann solvers for the Euler equations either for perfect gases, or for the most general equations of state, that cover ideal gases as a special case, but are conceptually hard to understand. This chapter filled the gap by giving a rigorous solution for the ideal gas case.

Suitability of the HLLE solver for SEC simulations has been discussed. In particular, the appearance of unphysical pressure oscillations at contact discontinuities has been investigated. Earlier publications regarded the oscillations as a numerical artifact that must be suppressed to obtain better solutions. Here, it has been shown that pressure oscillations naturally occur in physical diffusion processes. It has been argued that in the creation of robust solvers, one should not focus on obtaining the exact solution to the Euler equations, but instead accept and use the fact that due to numerical diffusion one actually solves a Navier-Stokes equation with unknown but small diffusion coefficient. Solutions to this equation are sufficiently close to the Euler system's solution, but also sufficiently smooth for the numerical scheme to give correct results. The HLLEM solver is based on this insight. Consequently, any attempt to fix the solver to suppress pressure oscillations would likely compromise its robustness. Still, contact discontinuities do create unphysical pressure oscillations that compromise the solution as well. It has been argued that the issue is less severe than it first appears: Only true contact discontinuities create pressure oscillations; smooth transitions do not. It has been shown that pressure oscillations do diminish quickly if one allows contact discontinuities to diffuse, instead of trying to maintain them, keeping the overall error small. This result is in striking analogy with the single-component, perfect gas case, where it is consensus that a compromise between maintenance of discontinuities and robustness must be found. *E.g.*, [34] showed that for a broad class of schemes the properties of preservation of stationary contact discontinuities and positivity are mutually exclusive.

Positivity of the HLLE solver has been established for the ideal gas case, and bounds for positivity preserving signal velocities have been derived. They are not as sharp as the ones Einfeldt and Munz found for the perfect gas case, but still an improvement over the simple choices in the original HLLE publication. Surprisingly, despite widespread use of the solver, to the author's knowledge, no earlier publication seems to have been devoted to this cause. A possible exception is [75], which is only available in Chinese.

The HLLEM solver, which restores an approximation to the contact wave in the Riemann problem, has been extended to the ideal gas case. Several alternative means to calculate the approximation have been discussed.

The SEC simulation code has been introduced, combining all of the results into a robust solver. Various test cases proved its ability to handle all situations relevant to SEC simulations: Smooth multi-component flow, dam-breaking problems and acoustics in the presence of an ideal-gas EOS. The coupling of fluid dynamics and chemical kinetics has been validated using a ZND detonation, and the coupling of the system with a geometric source term using a simulation of choked nozzle flow. In summary, it has been found that the code is well suited for the present use case.

# 4. Multi-Cycle Simulation of the Shockless Explosion Combustion

The *Shockless Explosion Combustion* is a thermodynamic cycle for achieving approximately constant volume combustion in a gas turbine. Its basic principle of operation has been introduced in section 1.1. This chapter concerns itself with numerical results on the feasibility and limits of a practical SEC: Can a SEC be achieved at all, and how close to a thermal explosion may the process be expected to get? Are there distinct limits for admissible errors in process control that still yield a SEC; that is, are the technical challenges quantifiable? How far may a real fuel deviate from the ideal model derived in section 2.2 without rendering the process infeasible in practice?

These questions have been partially addressed in earlier joint publications [10–12, 14, 15, 33, 79]. Advancements in the numerical simulation and understanding of the process allow to refine some of these results. Others admit significant extension. Parts of the chapter will hence, in content, reproduce these results.

The chapter furthermore gives preliminary results on promising extensions of the SEC concept. Before answering any of these questions, the specifics of SEC-simulations using the code developed in chapter 3 and concepts common to all simulations will be discussed briefly.

## 4.1. Numerical Setup

### 4.1.1. Boundary Conditions

The simulation of the one-dimensional SEC process restricts itself to the simulation of the flow and combustion after mixing within the combustion tube. It therefore neglects the question how a mixture of sufficient quality may be obtained, and how pressure waves can be prevented from travelling upstream into the compressor plenum. It is assumed that for both questions, answers resulting in perfect efficiency exist, that is, that the upstream domain boundary behaves like a solid wall for upstream-travelling pressure waves, and that a given mixture can be instantaneously provided at the inlet.

For practical applications, [13] suggests to use a fluidic diode to restrict upstream flow, and a fluidic oscillator for mixing. For the diode design used in the associated experiments, efficiencies are currently known neither for reflection of pressure waves nor for admission of flow downstream into the tube. Hence, a more elaborate model for the inlet condition would currently not quantitatively improve the results of the present study. As for the efficiency of the fluidic oscillator for mixing, blending has been assessed in [15] and it has been found that excellent quality can be achieved 5 cm downstream

from the inlet. Since a SEC may be realized by omitting charging this region with fuel, *i.e.*, stopping the charging process such that upon ignition, the whole stratification travelled sufficiently far downstream for all fuel to be well mixed, the instantaneous mixing ansatz is deemed sufficient for the time being.

The actual boundary conditions in simulations are implemented using ghost cells as follows: If the pressure at the upstream end of the computational domain exceeds a prescribed compressor plenum pressure, a rigid wall slip condition is applied, *i.e.*, a ghost cell that is a copy of the first cell with changed sign in the momentum coordinate is added. The solution to the associated Riemann problem between ghost cell and first interior cell has zero mass flux through the interface, enforcing the boundary condition. If pressure is below the prescribed value, the adiabatic expansion of the plenum state to inner pressure conditions is calculated and used as a ghost cell. Specifically, this means that pressure is expanded isentropically and total enthalpy is kept constant by converting excess internal energy into kinetic energy [6]. Blending is modeled by giving the plenum a time-dependent, instantaneously adjustable mixture composition. The state that is expanded to inner pressure at the boundary hence depends on time.

At the downstream end, the duct instantaneously opens into another plenum with fixed pressure. Since the jump in cross-sectional area is discontinuous, the boundary state cannot be modeled using an adiabatic expansion. Instead, it is assumed that the velocity in axial direction remains constant, while pressure is still isentropically expanded to its plenum value: Because at the end of the pipe, pressure can dissipate in all three spatial directions, only a fraction of the generated momentum points in axial direction, and vice versa for compression. This reasoning suggests to take between 0 and  $1/3$  of the enthalpy difference between inner state and expanded state and convert it into additional momentum in axial direction.

For validation of the ansatz, a simulation of a typical SEC pressure wave has been conducted: A tube sealed at the left end was set up to initially have (dimensionless) pressure  $p = 2$  within its first 40% and pressure  $p = 1$  in the 60% closer to the right end. For the right end, the expansion boundary condition was used, with a prescribed outer pressure of  $p = 1$ . Pressure and velocity were sampled just upstream from the tube's end. A second simulation was then run, this time in 2D, with a sufficiently large plenum (150 cells) attached to the right end of the tube. Figure 4.1.1 shows good qualitative agreement between both simulations; especially, pressure falls below the initial value at similar times. The model is thus deemed sufficient for the qualitative investigations at hand. For quantitative calculations, though, the model might need improvement, especially because of the different magnitudes of the suction wave.

### 4.1.2. Fuel Curve Determination

The most important ingredient to any SEC calculation is the determination of a suitable fuel curve, that is, the amount of fuel that needs to be injected as a function of time. The goal is to stratify fuel and air in such a way that the whole charge auto-ignites homogeneously such that auto-ignition delay time  $\tau$  is at each instant constant within the charge.

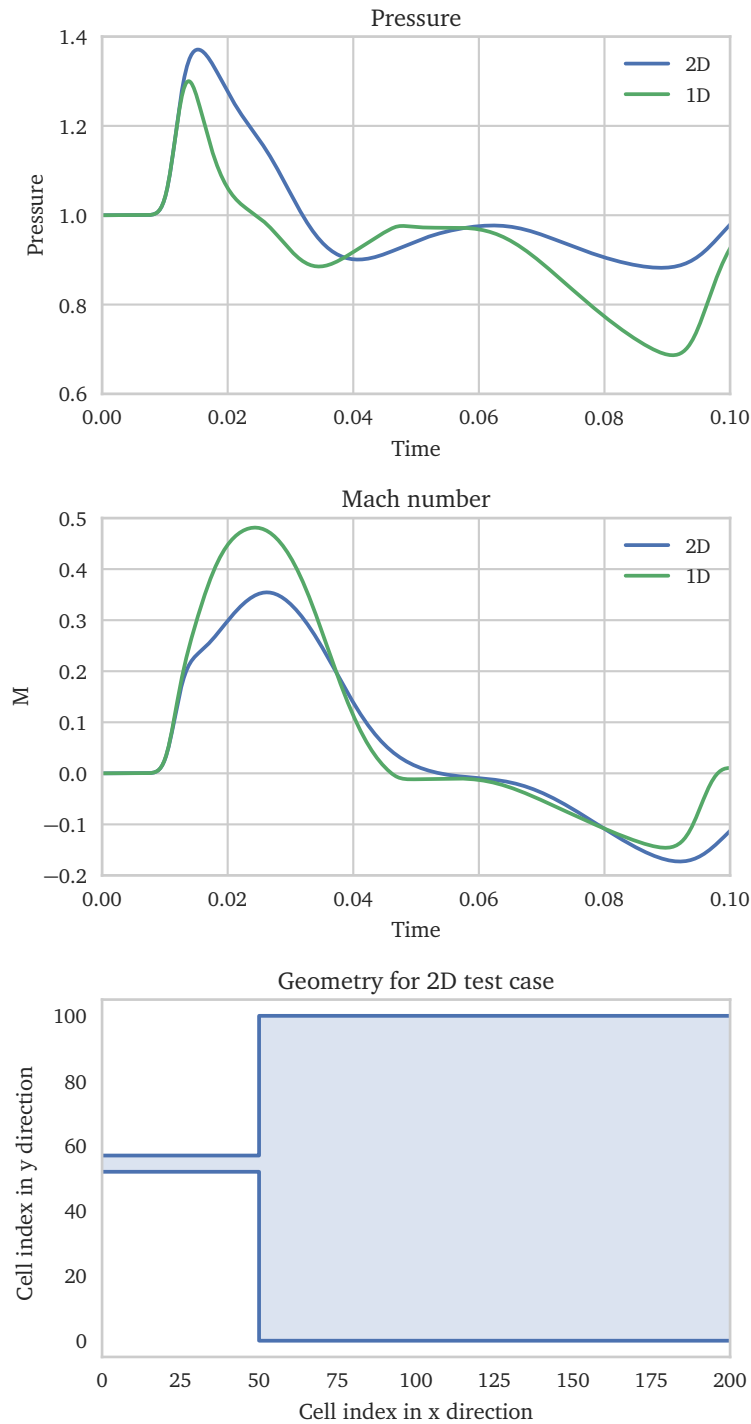


Figure 4.1.1.: Dimensionless pressure and Mach number at the pipe's outlet for the simulation of a pressure wave typical for SEC simulations leaving the tube. Comparison between 1D model for downstream boundary and a 2D simulation.

Consider the case where initially, pressure and velocity are constant throughout the domain, and the overall time until auto-ignition is sufficiently low to neglect diffusion. Since in ignition processes, pressure remains essentially constant before auto-ignition, the Euler equations only advect the fuel/air charge without deforming or mixing it. Until ignition, each point within the fuel stratification may hence be regarded as an autonomous system whose time evolution is uniquely defined by its initial conditions. That is,

$$\tau = \tau_0 - t_{\text{res}}, \quad (4.1.1)$$

with  $\tau_0$  the initial ignition delay time and  $t_{\text{res}}$  the individual residence time in the tube. To create a suitable fuel stratification in this configuration, it suffices to fix a point in time  $t_{\text{ign}}$  where ignition is desired, and, while setting up the stratification, at each instant choose  $\tau_0 = t_{\text{ign}} - t$ .

This raises the question how  $\tau_0$  may be “chosen”. In general,  $\tau_0 = \tau_0(p, T, Y)$ . In practice, these parameters cannot be influenced freely: In the compressor plenum, air at a given temperature is available, into which an adjustable amount of fuel at another temperature may be mixed at the inlet. The amount of fuel entering the system hence is the only available parameter. If the mixing process is modeled as an isenthalpic process, then  $T$  and  $Y$  may be calculated given the amount of fuel. In particular, this uniquely fixes the fuel/air equivalence ratio  $\Phi$ . Hence, with air and fuel temperatures given, it is a reasonable choice to regard the auto-ignition delay time as  $\tau_0 = \tau_0(\Phi)$ .

Practical limits for the range of  $\Phi$  impose maximal and minimal ignition delay times  $\tau_{\max}$  and  $\tau_{\min}$ : For  $\Phi \ll 1$ , the energy release becomes negligible and ignition delay time hence meaningless. For  $\Phi > 1$ , parts of the fuel cannot react due to a lack of oxidizer, which is obviously undesirable.

Regard the time at which charging starts as  $t = 0$ . Then  $t_{\text{ign}}$  may be chosen such that

$$\tau_{\min} < t_{\text{ign}} < \tau_{\max}. \quad (4.1.2)$$

The maximal admissible time usable for charging is  $t_{\text{ign}} - \tau_{\min}$ , and after charging is completed, it is necessary to wait for  $\Delta t = \tau_{\min}$  until ignition. To achieve acoustic resonance,

$$t_{\text{ign}} = \frac{2\ell}{c_{\text{avg}}} \quad (4.1.3)$$

should be chosen, with  $\ell$  the length of the pipe and  $c_{\text{avg}}$  average sound speed. The fuel and its temperature must then be selected such that the constraint (4.1.2) is fulfilled.

Obtaining the fuel curve itself is then a matter of inverting the relation between  $\Phi$  and  $\tau_0$ : At each instant, the inlet must provide a mixture with

$$\Phi = \Phi(\tau_0) = \Phi(t_{\text{ign}} - t). \quad (4.1.4)$$

In general,  $\tau_0(\Phi)$  and its inverse must be evaluated numerically. How the condition on  $\Phi$  translates to mass flows through a fuel valve has been discussed in section 2.3.

The assumption of constant charging velocity and constant pressure does not hold in practice. Figure 4.1.2 shows how the Mach number at the inlet varies in a dimensionless

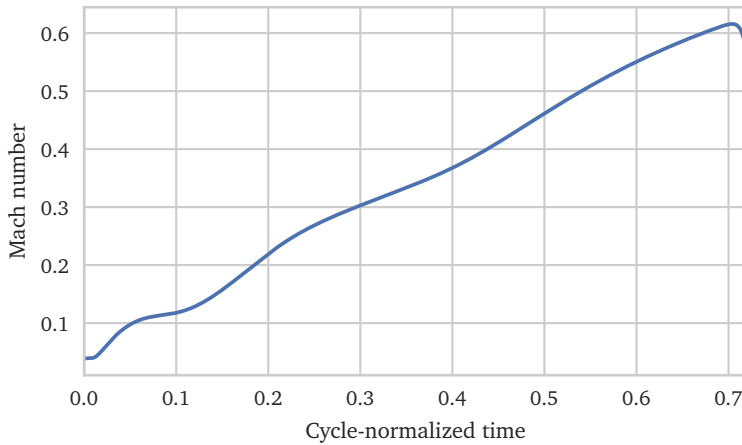


Figure 4.1.2.: Typical Mach numbers while charging a SEC. Data has been sampled 5% into the tube, from the start of the charging process until ignition.

SEC, using the ideal fuel model derived in section 2.2. If the changes are sufficiently smooth, then this primarily affects assembly of the mixture: To reach a given equivalence ratio, fuel mass flow must be adjusted to match a fraction of the air mass flow, which depends on the charging velocity. As long as the velocity is known, its dependence on time can easily be included in the calculation. Since the one-dimensional simulation does not include mixing but instead uses a premixed boundary condition, this issue does not affect it.

If the changes in velocity are not smooth and in particular strong shocks occur, then the assumption that each point within the fuel stratification may be regarded as independent of the others does no longer hold and the charging strategy fails. In the present simulations, this is not an issue: Particular strong shocks do only occur if a SEC ignition fails, and in such situations, the simulation can simply be adjusted to avoid the issue in the first place. For practical applications, process control must be used to return the system to working SEC conditions upon failure.

## 4.2. Results

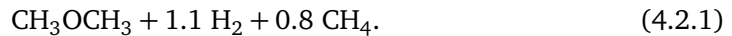
### 4.2.1. Atmospheric Single-Shot Ignition

In parallel to its theoretical investigation, the SEC was to be realized in an experiment at atmospheric pressure and a temperature of about 800K. It was soon found that fuels do in this regime have auto-ignition delay times in the order of 100 ms. A resonant SEC requires that auto-ignition delay time and acoustic timescale have the same order of magnitude. Since the sound speed is about 500 m/s, an experiment would require a tube that is at least 25 m long. With the contemplated fuel from chapter 2, it would even have to be 190 m long. This is obviously impractical. It was therefore decided to instead

aim for a single homogeneous auto-ignition in the first experimental investigation: An air flow is enforced in the test tube, fuel is injected to create a stratification, the flow is stopped, one waits until the residence time has passed, and then the quality of the mixture is assessed based on the homogeneity of the auto-ignition.

This experiment is an interesting test case for simulations as well: For real fuels, the charging concept from section 4.1.2 typically requires some fine-tuning until homogeneity is reached. It hence does not suffice to run *one* simulation, but instead *several* must be conducted until a working SEC simulation is established. As has been elaborated in section 2.1, current prospective SEC fuels come with large mechanisms of at least some dozens of species. This makes optimization of the stratification in a SEC impractical even in 1D. While it is possible to reduce the computational burden by choosing a lower resolution, one then also loses the ability to distinguish between partial and full detonation formation due to the SWACER-mechanism, which is undesirable as well. The simulation of a single shot allows to assess the critical charging process in an isolated fashion. Also, it gives insight into the required stratification quality given the prospective fuel and fuel model.

In [14], the quality of mixtures created using a fluidic mixing device designed for the SEC has been assessed. In the paper, mixtures of inert fluids were created and mixture quality assessed in discrete measurement planes downstream from the mixture apparatus. The experimental investigation yielded a standard deviation of  $\sigma = 2.424 \cdot 10^{-3}$  in equivalence ratio on a characteristic length scale of 9.7 mm, originating from the measurement plane placement. A numerical study investigated whether errors of this magnitude in the fuel/air stratification would still result in a homogeneous combustion in an experiment at 3 bar pressure. The simulation used the SEC fuel proposed by [18], which is a blend composed of



At the time when the paper was written, the reduced mechanisms discussed in chapter 2 were not yet available, and hence the initial one had to be used. Even the simulation of a single ignition takes several processor days to compute with it.

Hence, the computation was restricted to the simulation of a few milliseconds before and after ignition: Assuming a constant charging velocity, chosen such that the maximal range of possible ignition delay times is used up just as the domain is completely filled with fuel/air mixture, and neglecting two-stage ignition behaviour for the time being, the final stratification before ignition may be pre-calculated. By adding stochastic, Gaussian distributed noise to the equivalence ratio in the stratification at this point and then running a simulation until ignition, it can be assessed whether the noise suffices to significantly disturb the homogeneous combustion. The characteristic length scale of the noise can be incorporated by choosing noise values at discrete intervals and applying linear interpolation in between.

In the paper, a number of such simulations were conducted, including the case of extremal noise, that is, high noise values ( $3\sigma$ ) with alternating sign on each interpolation node. The study found that extremal  $3\sigma$  noise levels are too high to ensure a

homogeneous combustion, but that it remains homogeneous for noise within a  $2\sigma$  neighbourhood.

Since then, the simulation software, available mechanisms and understanding of the process have advanced, encouraging to repeat the calculation. The stratification in the study presented here deviates from the one in the original simulation: It now takes the equivalence ratio dependence of temperature (discussed in section 2.3) into account, assuming that air is supplied at 910 K and fuel at 200°C. Furthermore, since the 34 species mechanism from chapter 2 is available nowadays, it is no longer required to pre-calculate the kinetics until a point close to ignition, and hence it is no longer necessary to make the assumption that two-stage behaviour is negligible. Two new simulations were conducted:

The first one is an updated variant of the simulation from the paper. It is assumed that charging still happens sufficiently fast to be completed before the first stage ignites, *i.e.*, that the stratified state can still be pre-calculated analytically, and that the simulation may be started at this point. The simulation then includes the first ignition stage and its effects. In this situation, the naïve stratification from section 4.1.2 leads to a detonation even when no noise is applied. Numerical optimization may however be used to optimize it to retain homogeneity.

Such an optimized curve has been the basis for the experiment. Noise was added to it in the fashion described above. Figure 4.2.1 (a) shows that the peak pressure is 20 bar and that the ignition wave moves with 2350 m/s. A CJ-detonation would have 22 bar CJ pressure and move at 1992 m/s. The leading van Neumann pressure peak would have up to 45 bar if resolved. The simulation hence shows a weak detonation.

The second simulation considers the case where charging is not sufficiently fast to ignore flow/reaction interaction during first-stage ignition. It assumes a constant charging velocity of 11.25 m/s, such that upon ignition, exactly 40 cm of the simulation domain are filled with the stratified mixture. Flow is imposed as a left boundary condition, and fuel injection is modeled as described in the beginning of the chapter, following the same fuel curve as above. No perturbation is applied for this test case. When the stratification is completed, the boundary condition is immediately switched to a rigid wall slip condition.

The first stage ignites after 6 ms ( $\approx 7$  cm into the tube) and increases pressure by 0.3 bar. Figure 4.2.1 (b) shows a close-up on the second stage ignition of this simulation. The combustion propagates with about 1500 m/s. It is hence now no longer a weak detonation, but instead most probably a developing detonation. Also, ignition takes place nearly 50 ms later than predicted. This might be due to the varying temperature due to the pressure waves from first stage ignition altering the reaction paths and thus auto-ignition delay times. In any case, the simulation shows that the time-dependent fuel injection should for multi-stage fuels take the dynamics during the charging process into account.

### 4.2.2. Multi-Cycle Simulation with the Single-Stage Ideal Fuel Model

SEC fuels must admit accurate control over auto-ignition delay time even if the conditions within the combustion tube are only known approximately. One way to achieve this is

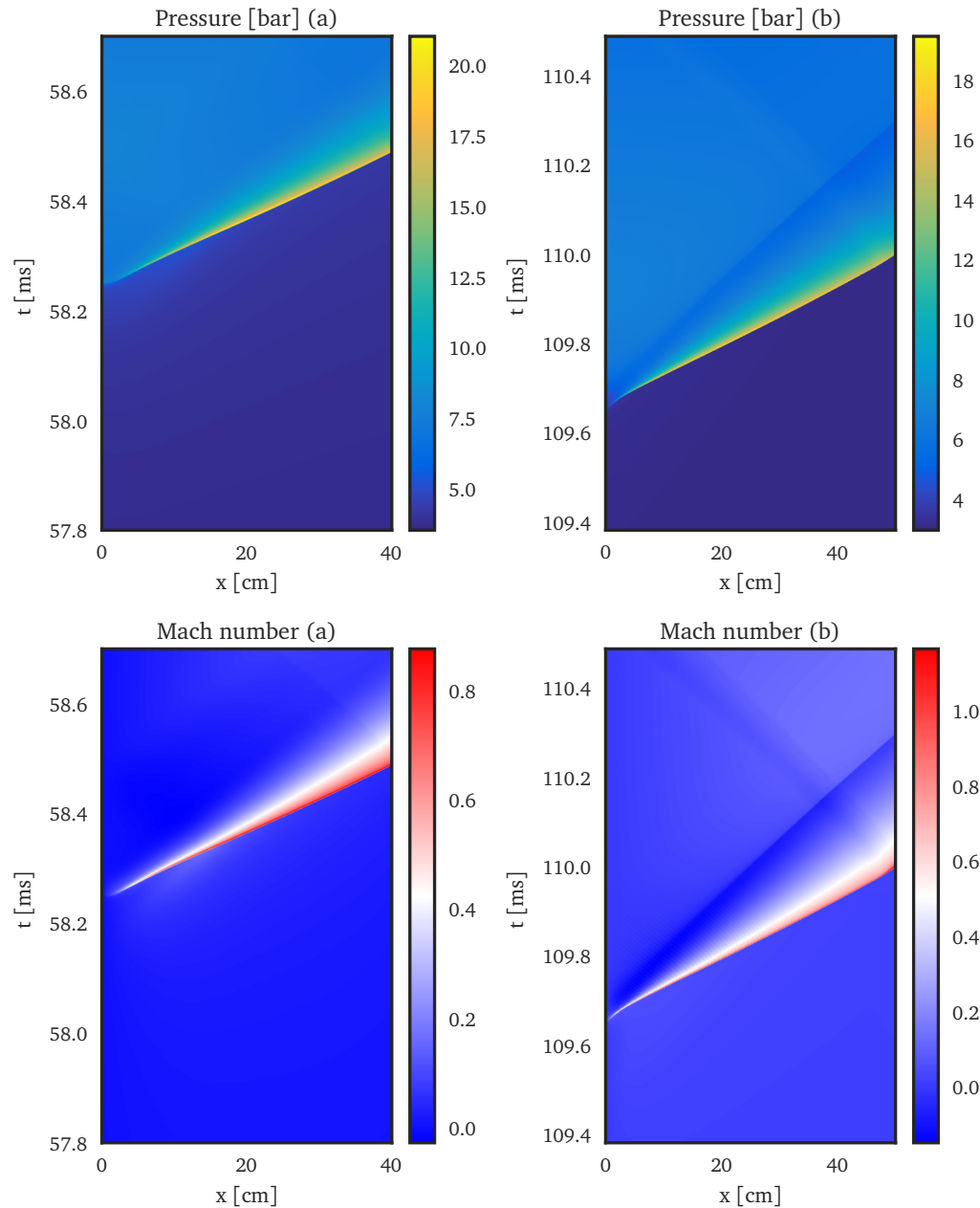


Figure 4.2.1.: Ignition of stratified SEC-fuel mixtures. (a) Mixture with extremal  $3\sigma$  inhomogeneities in the ideal  $\Phi$ -stratification assuming that the stratification is completed before the first stage ignites. (b) Simulation of the ignition of an unperturbed mixture including the creation of the stratification. The stratification is created at a velocity where the first stage ignites before particles reach their final position in the stratification, such that the pressure rise alters the stratification.

to tailor fuels such that they have the property that their auto-ignition delay time varies only by few milliseconds over a large range of temperatures. This way, temperature within the combustion tube does not need to be known exactly, and the problem of creating a proper stratification reduces to ensuring sufficiently good mixture quality. In section 2.2, an idealized fuel model for fuels with this property has been introduced: It features an auto-ignition delay time that is completely independent of temperature within a given temperature range. In the associated publication [11], several studies have been performed to assess which general results can be derived from this model and how much another fuel may deviate from the model's idealized behaviour without harming the process. This section reproduces these results.

### Unperturbed Simulation

The most straightforward test case is the simulation of a multi-cycle SEC. The charging concept from section 4.1.2 may be applied to the model from equations (2.2.1)-(2.2.2) as follows: The decay rate constant

$$\lambda = -\log(\varepsilon) \quad (4.2.2)$$

is given as part of the model. If an auto-ignition delay time of  $\tau \in (0, 1]$  is desired,  $Y_F$  must hence be initially

$$Y_{F,\text{initial}}(\tau) = \varepsilon \exp(\lambda \tau). \quad (4.2.3)$$

This means that if fuel is to be injected into the combustion tube at all, then a mass fraction ratio of

$$Y = \{\text{Intermediate} = 1 - Y_{F,\text{initial}}(\tau), \text{Fuel} = Y_{F,\text{initial}}(\tau)\} \quad (4.2.4)$$

must be set as the instantaneous boundary condition.

For the experiment, the stratification from section 4.1.2 was produced as follows: The time  $t_0$  when the upstream valve opened was recorded. Fuel was injected at each instant such that

$$\tau = \tau_{\max} - (t - t_0). \quad (4.2.5)$$

To separate hot exhausts from fresh gas, fuel injection did not start right away, but only when  $(t - t_0) > t_{\text{buffer}}$ .  $t_{\text{buffer}} = 0.5$  has experimentally proven to be a robust choice. The pipe was chosen to have length  $x = 1$ . This necessitated to use  $\tau_{\max} = 0.77$  to ensure resonant behaviour, given the (computed) average sound speed of 1.7 in the pipe.

Figure 4.2.2 shows streak plots of the simulation. Up to the time resolution of the plots, ignition is perfectly homogeneous. The different cycles are almost identical, only the reflection of the pressure wave from the downstream end varies slightly. It is an interesting observation that the cycle length is  $\Delta t = 1.58 \approx 2\tau$ , i.e., close to the second harmonic of the expected resonance time. The reason for this becomes clear when one inspects an isolated cycle. The cycle generated by the initial conditions of the simulation, namely a perfectly homogeneous ignition, which has been stripped from fig. 4.2.2, can be seen in fig. 4.2.3: The leading pressure wave, originating from the right end of the

ignited volume, already generates a reflection that is sufficient to initiate charging. A second strong wave is present in the system, following right behind the first one. The interaction of the two waves makes the process more complex than predicted by the basic model. It is noteworthy that this behaviour is weakened if the stratification is such that the mixture does not ignite homogeneously, but in a unidirectional (weak) detonation. In the H<sub>2</sub>-experiment from section 4.2.5, which features weak detonations, it cannot be observed at all.

### Admissible Temperature Dependence

The temperature field in fig. 4.2.2 shows that the temperature in the stratified mixture fluctuates by about 0.05 before ignition, corresponding to 50 K in dimensional units. This confirms the assumption that a SEC fuel should have essentially constant auto-ignition delay times over a range of at least 100K.

The reaction describing the auto-ignition delay time, eq. (2.2.1), has an additional Arrhenius term  $\vartheta_T$ , that was initially set to zero, but present to allow to quantify the notion of “essentially constant”. By setting  $A_T = 1$  to keep the overall temperature dependence small, and choosing a positive activation energy  $E_T$ , a non-zero  $\partial\tau/\partial T$  gradient may be added to the chemistry. To observe its effects, the SEC simulation was run repeatedly with different values for  $E_T$ , and peak pressure (exemplary at  $x = 0.01$ ) was measured for each value. Figure 4.2.4 shows the results. Larger dependencies do indeed lead to detonations, with a significant pressure rise for  $\partial\tau/\partial T \geq 0.4$ , corresponding to 0.4  $\mu\text{s}/\text{K}$  in dimensional quantities. Note that 0.4  $\mu\text{s}$  is in the order of the excitation time scale, which supports the hypothesis from the introduction, stating that its magnitude might be relevant to the robustness and error tolerance of the process.

### Stratification Error Tolerance

The mixture in the experiment has been set up such that right before ignition,  $\partial\tau/\partial x \approx 0$  in the stratification. In a real-world scenario, the stratification cannot be expected to be this good. Instead, it will always have some inhomogeneities. This experiment investigated the case where  $\partial\tau/\partial x = \text{const} > 0$ . It is not only the simplest case of inhomogeneities in this setting that can systematically lead to detonative combustion, but also one that is closely related to the SWACER mechanism and deflagration to detonation transition. For general fuels, it has been investigated thoroughly in [35]. The paper establishes a relation between the auto-ignition delay time gradient’s magnitude and the sound speed in the unburnt mixture and identifies ranges of the ratio of the two with different combustion modes: Small ratios lead to weak detonations, intermediate ones to developing detonations, and very large ratios to deflagrative combustion. The present study compared the results for the ideal fuel model with their findings.

To create a mixture with an approximately constant spatial auto-ignition delay time gradient, a linear factor was introduced into the fuel curve (4.2.5), such that

$$\tau = \tau_{\max} - (1 + \xi)t + t_0. \quad (4.2.6)$$

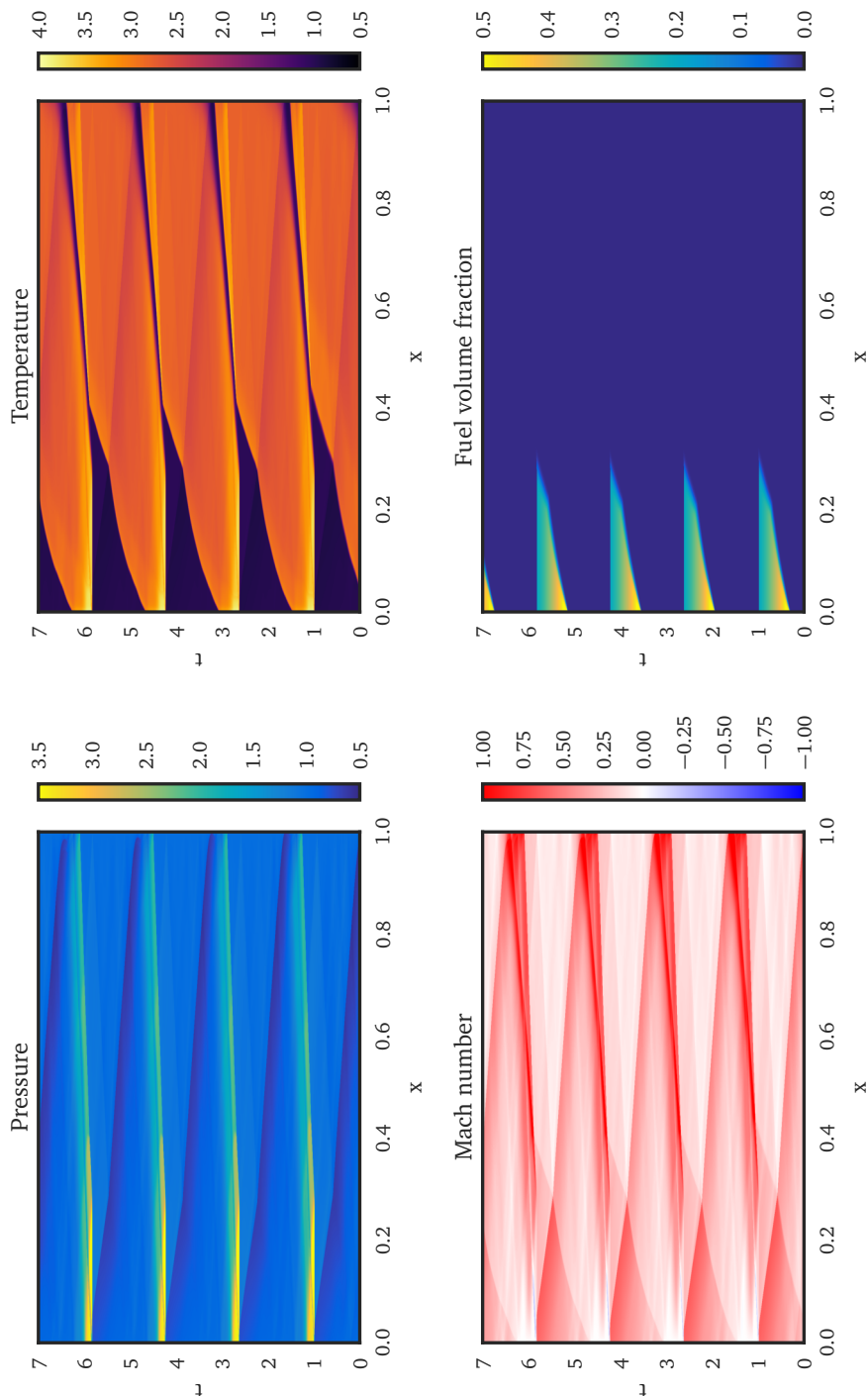


Figure 4.2.2.: Multi-cycle simulation with the single-stage ideal fuel model.

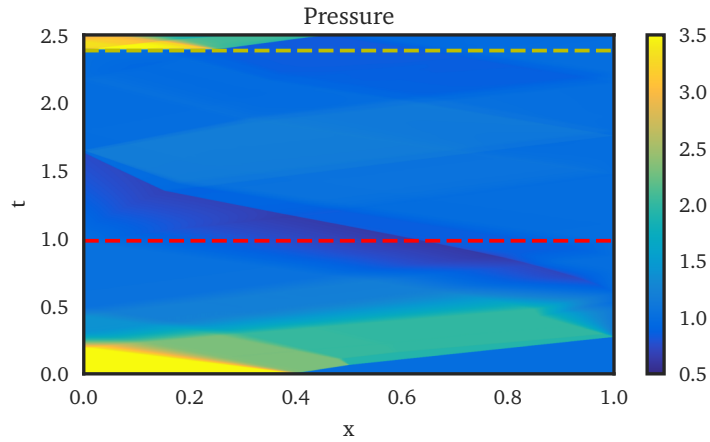


Figure 4.2.3.: Pressure for an isolated ignition, with initially homogeneous pressure, in the single-stage ideal fuel model. The red line depicts the time when pressure at the valve drops below plenum pressure, the yellow one ignition.

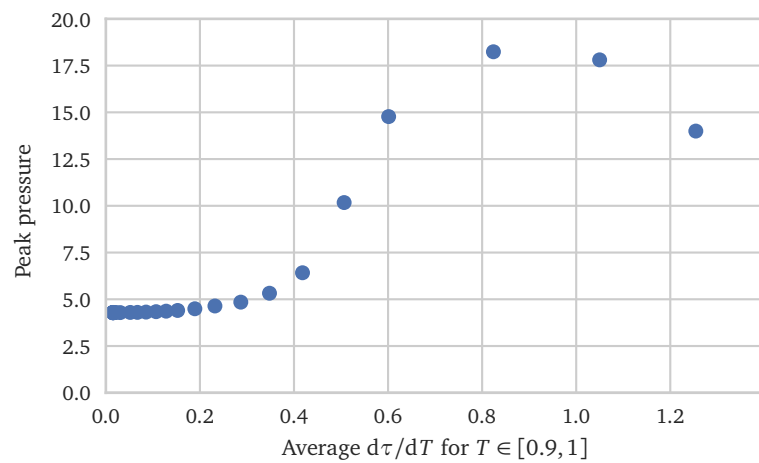


Figure 4.2.4.: Dependence of peak pressures in a SEC-ignition on the level of auto-ignition delay time dependence on initial temperature.

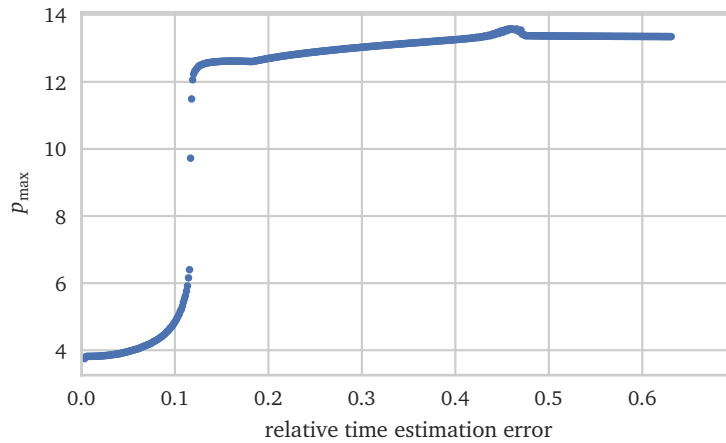


Figure 4.2.5.: Dependence of peak pressures in a SEC-ignition on the slope of auto-ignition delay time in the final stratification.

If charging velocity  $v_c$  is constant, then this results in a  $\zeta = \xi/v_c$  slope in the stratification. In [11],  $v_c$  was measured to be  $v_c \approx 0.471$  on average, and it was found that this approach is sufficient to generate the desired stratification. As in the earlier experiment, multiple runs of the SEC simulation were carried out with various values for  $\xi$ , and the peak value of the pressure field has been stored for each.

Figure 4.2.5 shows the dependence. The two most striking features are a sharp rise at  $\zeta = 0.12$  and the curve remaining constant for  $\zeta \gtrsim 0.45$ . Both values are in accordance with the findings by [35]: They predict detonations to develop as the auto-ignition wave's velocity approaches the sound speed in the unburnt mixture. The simulation has  $c = 1.14$ , so  $\zeta = v_c c^{-1} = 0.41$ , close to the observed value of 0.45. They also conjecture a lower bound below which detonations are weak, without giving an explicit formula, but hinting at a connection to the CJ velocity  $v_{cj} = 3.84$ .  $\zeta = v_c v_{cj}^{-1} = 0.12$ , which is in perfect accordance with the value from the plot.

This connection is not surprising, given that the experiment is designed to produce weak detonations and that the slowest existing weak detonation has CJ velocity (see section 3.5.7).

### Excitation Time Scale

It has already been stated that the time scale on which energy is released is of importance to the error tolerance with regard to perturbations in the auto-ignition delay time stratification. In section 4.2.1, the effect of Gaussian distributed noise has been investigated for a real fuel. The study on stratification errors regarded small, piecewise linear errors in auto-ignition delay time. In the present simulation, an extra dimension was added to the study by furthermore varying the time scale of the excitation reaction.

The rationale is as follows: If there is a hotspot, *i.e.*, a single point in the stratification

that ignites significantly early, then the combustion will locally increase the pressure. As this pressure dissipates into the unreacted fuel adjacent to the hotspot, it compresses it and thus raises temperature. Since the fuel is already very close to auto-ignition, the pressure rise might suffice to trigger a detonation. There then is a race between the time that it takes the adjacent fuel to auto-ignite as planned, which would make the hotspot unproblematic, and the time that it takes for the pressure to locally rise and then dissipate sufficiently to trigger the adjacent fuel to ignite early. The time scale with which energy is released, and thus on which pressure rises, is the excitation time scale. The larger it is, the less likely is a local hotspot to trigger a detonation.

In an experiment, the excitation time scale can be adjusted by altering the activation energy  $E_I$  of the excitation reaction (2.2.2). The original SEC simulation was again used, but a local error was introduced as a region with a discontinuous jump to a lower, variable ignition delay time. Following the study from section 4.2.1, a width corresponding to 9.7 mm was chosen for this region. Again, peak pressure was measured. Figure 4.2.6 shows how it depends on the two degrees of freedom. Compared to the original results in [11], the simulation featured an increased resolution, allowing to better distinguish the different regimes: There are sharp boundaries separating excitation times sufficiently small to cause detonation from those where no detonation occurs, with the bound being at an excitation time of about 0.005. Pressure still rises to a value higher than it would in an isochoric combustion for longer excitation times if the hotspot ignites close to the desired auto-ignition. This is due to an interaction of the pressure wave emanating from the hotspot and the auto-ignition. For small excitation times, any hotspot that ignites sufficiently early creates a detonation, but the strongest coupling happens if  $\Delta\tau$  stays relatively small, *i.e.*, the remaining fuel is very close to auto-ignition.

The  $3\sigma$  error from the single shot simulation in section 4.2.1 corresponds to a time span of 0.0185 in dimensionless coordinates. Dimensionless excitation time for the SEC fuel is 0.002. This region is not resolved in fig. 4.2.6. Figure 4.2.7 shows detailed values for this excitation time and small values of  $\Delta\tau$ . CJ pressure in the experiment is 12.83, and the pressure at  $\Delta\tau = 0.0185$  is 11 in the figure. If one uses the CJ pressure as a reference to convert to dimensional quantities, then one would expect a pressure peak of 18.86 bar in the single-shot experiment from section 4.2.1, which is close to the observed value. Though this value is not very accurate due to the kind of the simulation,  $\Delta\tau < 0.005 \equiv 2 \text{ ms}$  may be derived as a detonation limit from the plot.

### Compressor-to-Turbine Pressure Ratio

If the energy released in a SEC combustion cannot be transported away quick enough, then a mean pressure gain can be observed at the downstream end of the combustion tube. This is an issue for all pressure rising combustion processes, and one that the SEC incorporates by actively utilizing the pressure gradients in its recharging concept. If the mean pressure ratio between compressor and turbine plenum however becomes too large, the reflected low-pressure wave can become too weak to recharge the tube.

Again, a repetition of the initial SEC experiment was performed, with varying pressure in the downstream plenum. Figure 4.2.8 shows the maximal width of a fuel stratification

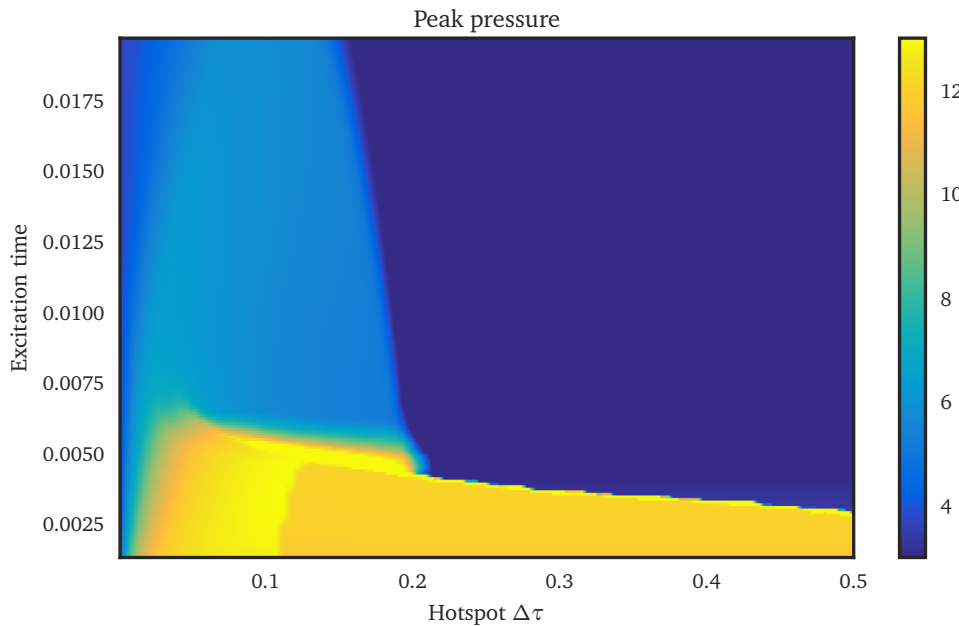


Figure 4.2.6.: Dependence of peak pressures in a SEC-ignition on the excitation time and anticipation time of hotspot that leads to ignition.

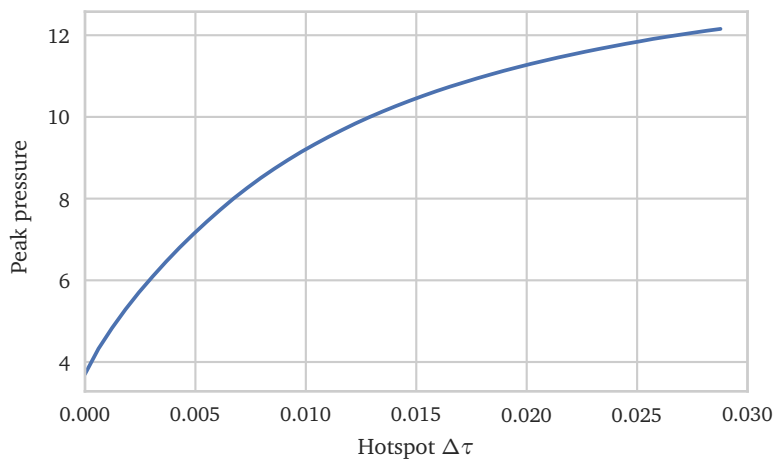


Figure 4.2.7.: Dependence of peak pressures in a SEC-ignition on the strength of a hotspot with the standard reactions from table 2.2.1.

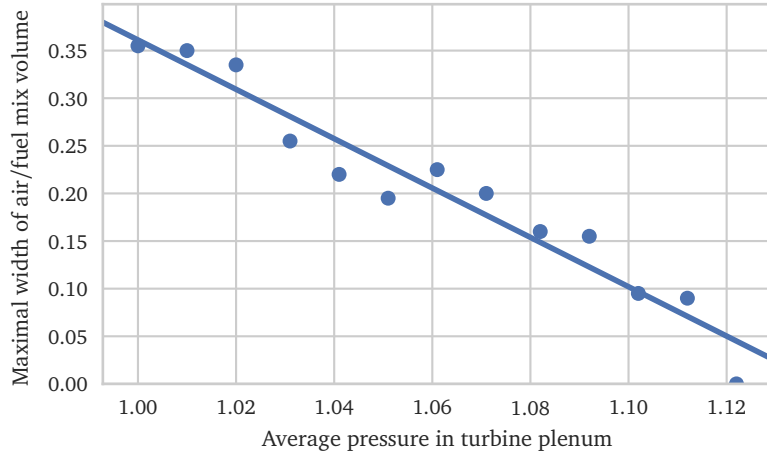


Figure 4.2.8.: Influence of turbine to compressor plenum pressure ratio on capability to maintain a SEC. Compressor output pressure is 1.0.

in each simulation for times between 3 and 10, with the lower time bound being in place to allow the system to tune itself or fail, if the downstream pressure is too large. The figure shows that a pressure gain up to about 10% is sustainable.

### 4.2.3. Multi-Cycle Simulation with the Two-Stage Ideal Fuel Model

The single-stage ideal fuel model that was investigated in section 4.2.2 has been extended to support the multi-stage ignition of DME and similar fuels in section 2.2.2. The extension works by inserting another two reactions into the system that convert the product of the first set of reactions, now dubbed the intermediate fuel, into the final product. This second reaction again has time-independent auto-ignition delay time.

The extension was published in [11], and a first numerical investigation was performed in [12]. For the present simulation, the basic test case of section 4.2.2 was repeated, adjusted to the two-stage model:

The model has two fixed decay rate constants,

$$\lambda_F = -\log(\varepsilon) \eta^{-1}, \quad (4.2.7)$$

$$\lambda_I = -\log(\varepsilon)(1-\eta)^{-1}, \quad (4.2.8)$$

where  $\eta = 3/4$  defines how much of the total auto-ignition delay time  $\tau = 1$  is spent in the first ignition stage. To have an auto-ignition delay time of  $\tau \in (1-\eta, 1]$ , hence,

$$Y_{F,\text{initial}}(\tau) = \varepsilon \exp(\lambda_F(\tau - \eta)), \quad (4.2.9)$$

$$Y = \{\text{Radical 1} = 1 - Y_{F,\text{initial}}(\tau), \text{ Fuel} = Y_{F,\text{initial}}(\tau)\} \quad (4.2.10)$$

must be set as the instantaneous boundary condition. For  $\tau \in (0, 1 - \eta]$ ,

$$Y_{I,\text{initial}}(\tau) = \varepsilon \exp(\lambda_I \tau), \quad (4.2.11)$$

$$Y = \{\text{Radical 2} = 1 - Y_{I,\text{initial}}(\tau), \text{ Intermediate} = Y_{I,\text{initial}}(\tau)\} \quad (4.2.12)$$

must be used.

A direct comparison of the two-stage simulation in fig. 4.2.9 with the single-stage simulation qualitatively gives the same results, and in detail only the small pressure rise upon ignition of the first stage shortly before the second stage ignites as a difference.

There are several things worth pointing out about the two-stage model:

- While it is numerically possible to inject fuel arbitrarily close to ignition, a real SEC fuel has a non-zero minimal auto-ignition delay time. Especially for multi-stage fuels, while it is numerically possible to inject fuel in a state between first- and second-stage ignition, this is not possible in a real world scenario.
- The energy release from the first stage must be such that the temperature after first-stage ignition is below the activation limit of the high-temperature reaction path, or the second stage will ignite early. In other words, the energy release from the first stage reduces the effective width of the temperature region where ignition-delay time is independent of temperature.
- If the energy release from the first stage is sufficient to raise pressure above the inlet plenum pressure, then charging stops as the first stage ignites. In any case, ignition of the first stage will slow down the charging process.
- Real fuels have the property that for higher initial pressures  $\eta \rightarrow 1$ , but the pressure rise becomes significant as well. E.g., for DME at 1 bar and 750 K,  $\eta = 0.06$ , and the pressure rises (in an isochoric combustion) by less than 0.3 bar. At 3 bar,  $\eta = 0.1$ , and  $\Delta p = 0.3$  bar. At 12 bar,  $\eta = 0.625$  and  $\Delta p = 3$  bar. Finally, at 30 bar,  $\eta = 0.9$  and  $\Delta p = 10$  bar. Close to the low pressure end of this range, the pressure rise may be ignored and a stratification computed as if it was not present. This is what has been done in section 4.2.1. Close to the high pressure end of this range, the time between first and second stage becomes sufficiently short to ignore, and instead a stratification may be computed as if first stage ignition was the only ignition event. In the intermediate range, one must take the two-stage ignition into account, which justifies why the two-stage model is needed.

Simulations confirm all of these points.

When the two-stage model was introduced in section 2.2.2, a curve was presented that demonstrates that the fuel can be tuned to have the same (non-constant) auto-ignition delay time as the fuel blend suggested by [18] for a range of temperatures. In [12], the computation of a multi-cycle simulation with the tuned model was conducted as well: As expected, ignition is no longer homogeneous right away for the model with temperature dependence. Instead, the stratification must be optimized to regain homogeneity.

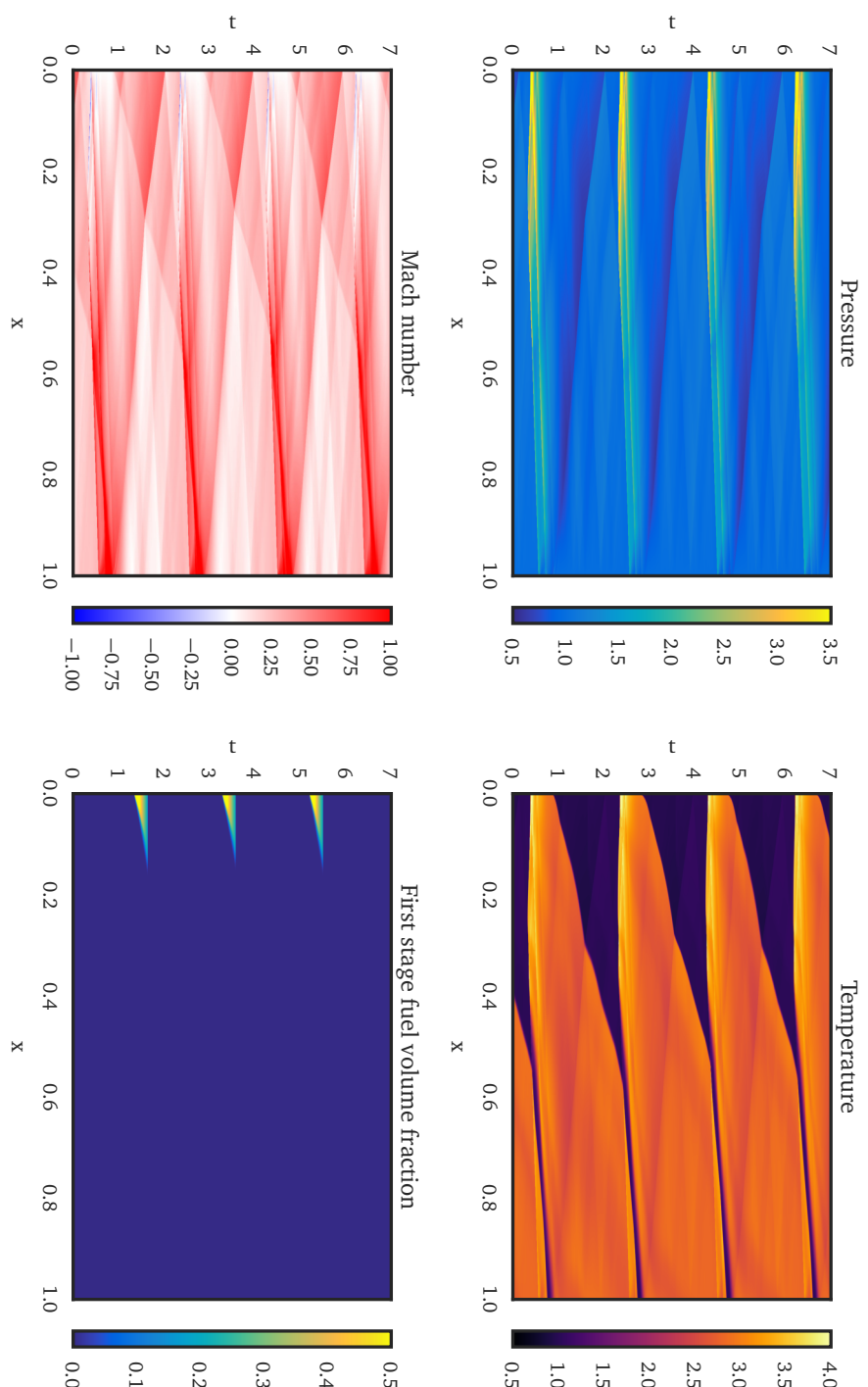


Figure 4.2.9.: Multi-cycle simulation with the two-stage ideal fuel model.

#### 4.2.4. Efficiency Limits for the Upstream Boundary Condition

In section 4.2.2, the acceptable pressure gain measured from the upstream to the downstream end has been investigated. The test case can be interpreted as a test for the efficiency of the downstream boundary condition. A similar test is advisable for the upstream boundary: If a low-pressure wave reaches the boundary, and it is partially reflected instead of creating a positive velocity, recharging the SEC might fail.

Figure 4.2.10 is an example demonstrating that this might be an issue: It shows the temperature field of a 2D simulation using the single-stage ideal fuel model, that naïvely took an under-resolved, zeroth-order representation of the fluidic diode geometry from [13] and placed it in front of the upstream boundary. The rest of the simulation is unchanged from the basic simulation carried out in section 4.2.2. All of the plots show the field after the low-pressure wave reached the upstream end, but before new fuel can be injected for the second ignition — the amount of fresh air allowed to flow downstream through the diode does not suffice to flush and thus recharge the tube.<sup>1</sup>

To quantify how efficient the upstream boundary must be, the basic SEC simulation was repeatedly conducted until time  $t = 10$  with different efficiencies and pressure rises. For each run, the mean time from opening of the upstream valve to ignition, and the mean length of each charge upon ignition was measured. A reduced flow rate means that it takes longer to create the buffer of fresh air, separating fuel from hot exhausts. To compensate for this, the buffer time was not fixed, but a flexible buffer was used instead: In addition to waiting a minimal time of 0.5 after the pressure initially fell below the inlet pressure, fuel injection was further delayed until the first 15% of the tube had a temperature below 1.2, *i.e.*, to a temperature within the region where auto-ignition delay time is temperature-independent. This leads to smaller fractions of the tube being filled as well.

To ease the modelling effort, the boundary efficiency has been defined as an efficiency for *velocity*: For an impinging low-pressure wave, the boundary condition from section 4.1.1 states that the plenum state is isentropically and isenthalpically expanded to the inner pressure. The enthalpy conservation condition accelerates the flow, which leads to a change in velocity  $\Delta u$ . If instead of by  $\Delta u$ , the velocity only changes by  $\eta \Delta u$ , then the boundary condition by definition has an efficiency of  $\eta$ .

Figure 4.2.11 shows both relations. As before, ideal values are  $\Delta t \approx 1.6$  and a mean normalized charge volume of 0.4. The practically most relevant non-dimensional pressure rises are between 3 and 5. There, velocity efficiencies of 0.5 are acceptable.

#### 4.2.5. Multi-Cycle Simulation with Real Fuels

In [11], a SEC using  $H_2$  as a fuel was simulated to demonstrate that, in theory, the process may be realized with any fuel. The temperature independence is only required because a technical realization cannot control temperature sufficiently accurate to work with

---

<sup>1</sup>The situation improves if a higher-order approximation to the boundary [46] and higher resolution are used, but the general problem that recharging fails persists.

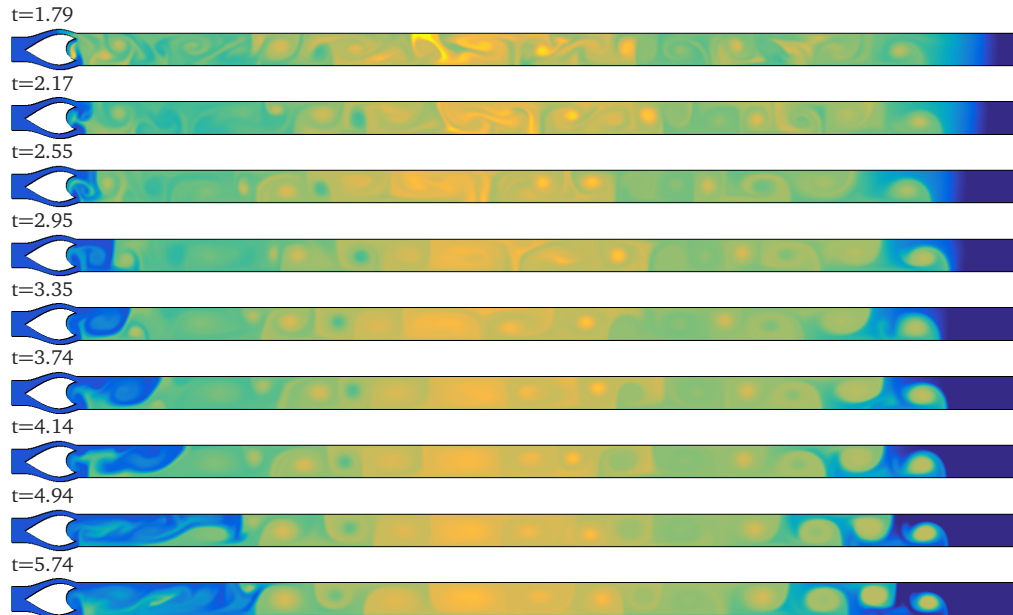


Figure 4.2.10.: Qualitative plot of the temperature field in a 2D SEC with the single-stage ideal fuel model with  $\Delta Q = 10$  and the inlet geometry suggested by [13] at different times in a single cycle. Only blue temperatures are sufficiently low to allow injection of fresh fuel. In a working SEC cycle, the first image should already show the second cycle, but in the sequence, all images are from the first one. The figure serves to show that inlet geometry might inhibit recharging.

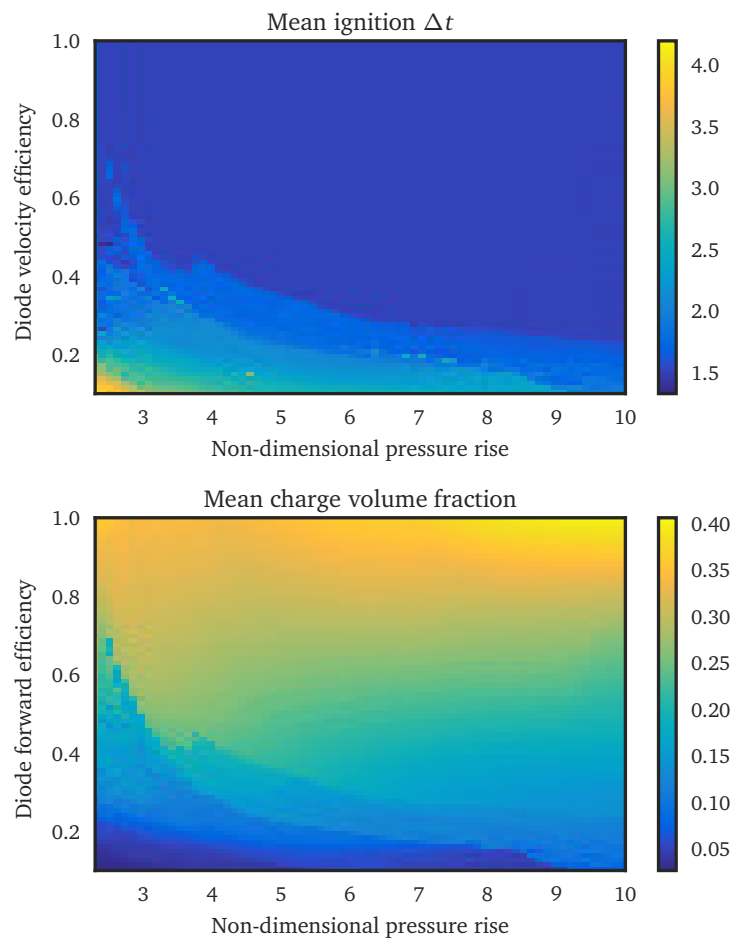


Figure 4.2.11.: Dependence of SEC performance on the diode's forward velocity efficiency and pressure rise.

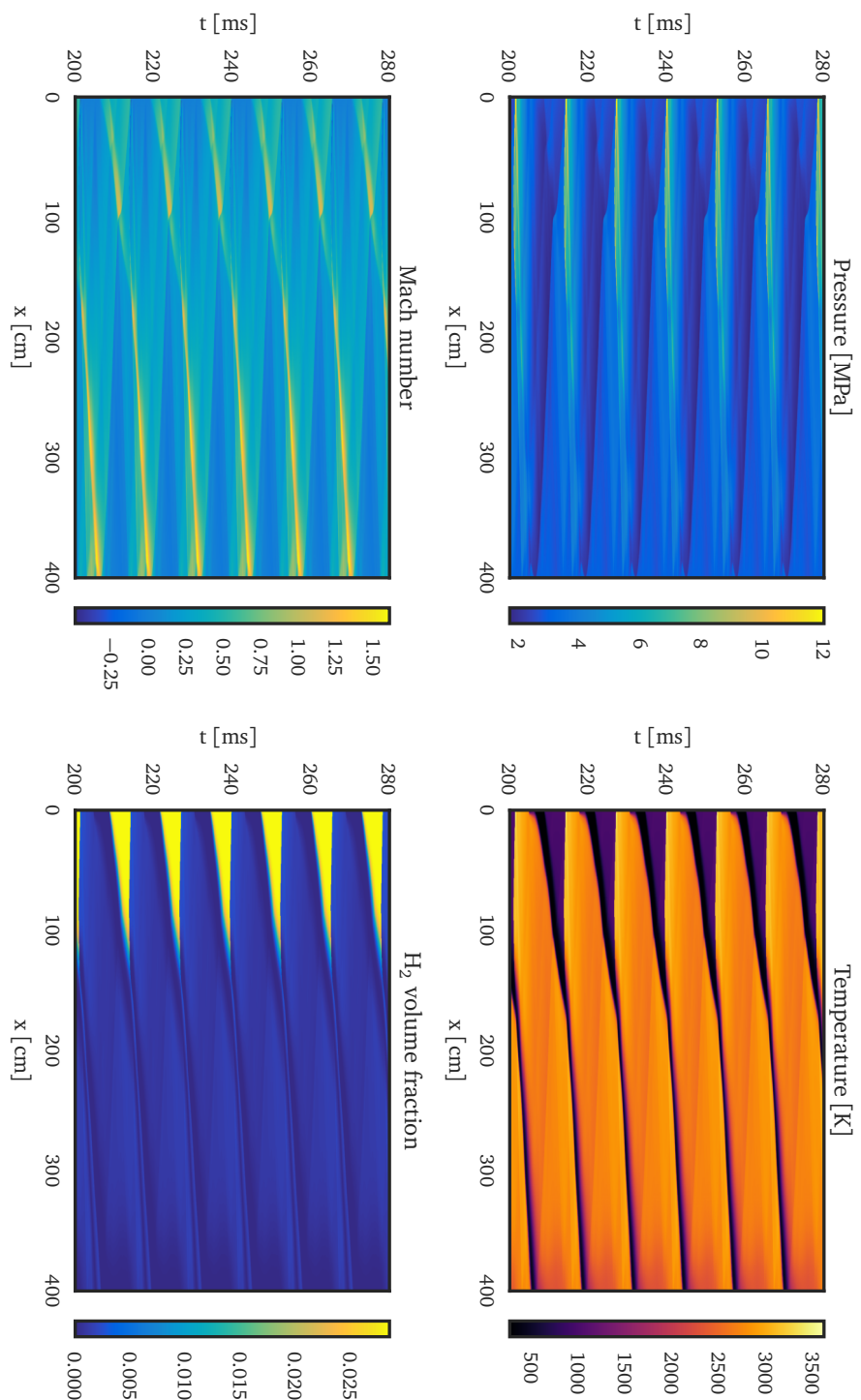


Figure 4.2.12.: Actively controlled multi-cycle simulation with  $H_2$  in air at 30bar.

such reactive fuels. By further optimization of the fuel curve, this section extends the simulation to one that reliably produces weak detonations.

Hydrogen has been chosen because it is a simple fuel for which small, yet accurate mechanisms exist. For the simulation a high pressure mechanism with 11 species was used [17]. The simulation was set up at 30 bar and 1000 K, close to the conditions that one would expect in a gas turbine. The high temperature is required to obtain auto-ignition delay times in the order of milliseconds (3.66 ms at exactly these conditions), such that the pipe and hence numerical domain can remain relatively small (4 m). A resolution of 1 cm was used. At these conditions, a CJ detonation would travel with 1979 m/s and have a CJ pressure of 150 bar.

Temperature was used instead of equivalence ratio to control auto-ignition delay times in the stratification: In a temperature range between 1000 K and 1100 K with constant equivalence ratio  $\Phi = 1$ , this allows for a greater range of auto-ignition delay times ( $\Delta\tau = 3.16$  ms) and hence a larger stratification. Since the simulation is under-resolved, developing detonations cannot be identified easily, and a larger stratification gives them more time to develop into a CJ detonation which would be identifiable by the high pressures. Since the code does not feature explicit diffusion terms, and numerically treats species diffusion and thermal diffusion in the same fashion, using a temperature stratification is not a simplification: If the process numerically works with temperature stratifications, then it would work with equivalence ratio stratifications as well.

The fuel curve has been obtained as follows: Auto-ignition delay times were sampled in 150 equidistant points for the given range of initial conditions and a fifth order polynomial was fitted for  $T_0(\tau)$ , initial temperature as a function of desired ignition delay time. An a posteriori error analysis shows that the interpolated representation is sufficient: If auto-ignition delay times are sampled for the interpolated temperatures for each of the original auto-ignition delay times, then the difference of both times has a standard deviation of  $\sigma = 5 \cdot 10^{-6}$ , which is of the order of excitation time. This has been found sufficient in section 4.2.2.

The same dynamic air buffer strategy as in section 4.2.4 was used: Fuel injection was delayed until the first 15% of the tube were flushed with fresh air, independent of how long this took. A posteriori, from the results below, a fixed buffer of 4 ms would have sufficed as well. The advantage of the dynamic strategy is that if for some reason flushing takes longer than anticipated, while the resonant behaviour is lost, a homogeneous combustion by auto-ignition is still achieved, with the associated pressure rise. With a fixed buffer time, if the buffer is not large enough to avoid mixing of hot exhausts and fresh fuel, combustion is not homogeneous, and in the worst case, the pressure rise is not sufficient to recharge the tube for the next cycle. The time when injection was started was recorded and the difference to this point in time denoted  $\Delta t$ . Fuel was then injected at a temperature

$$T_0(\tau_{\max} - \xi \Delta t), \quad (4.2.13)$$

with a variable parameter  $\xi$ . The effects of such a parameter on fuels with temperature-independent auto-ignition delay have been investigated in section 4.2.2. Here, it allows to tune the stratification to a point where, reliably, the mixture combusts weakly detonative.

A value for  $\xi$  was obtained from a parameter study, and  $\xi = 0.6$  found to be a good choice.

Figure 4.2.12 shows the results from the simulation. The cycles repeat smoothly every 12.8 ms, roughly  $4\tau$ , as expected for a weakly detonative SEC (see section 4.2.2). Pressure peaks at 94 bar before reflection of the pressure wave at the boundary (133 bar upon reflection), which is above the pressure of an isochoric combustion (83 bar), but well below CJ pressure (150 bar). The combustion waves travel with about 2040 m/s. The process hence features weakly detonative combustion.

#### 4.2.6. Axial Variations of the Tube Diameter

In section 3.5.6 on the simulation of a choked Laval nozzle, it has been shown that and how axial variations of the tube diameter have an influence on the local Mach number and pressure. This section is concerned with how they can be utilized to make the SEC process more robust. Two possible uses were contemplated in the project: The residual high-pressure wave that moves upstream before ignition can be focused and utilized in the auto-ignition process. The fuel stratification must then take the impinging wave and its effect on the ignition process into account. The other use case is to alter the acoustics within the tube, to make the recharging process more efficient. A well-known setting where the same principle is used is in the exhaust of two-stroke engines, which typically have an expansion chamber that reflects a part of the pressure back into the combustion chamber to increase cycle efficiency.

It is a challenging endeavor to focus the pressure waves such that auto-ignition delay times are significantly altered: The pressure wave must not become sufficiently high to ignite the fuel right away, because combustion would not be homogeneous then. Instead, it must only serve to lower the auto-ignition delay time by a known amount. The strength of the pressure wave and the time when it arrives at the stratification must then be known with high precision, whereas a SEC that does not focus pressure waves has a high tolerance for non-resonant operation. The focus of the investigation was hence laid on the acoustics altering effect.

The ideal fuel simulation from section 4.2.2 was carried out for multiple axial configurations. Four of them are prototypically shown in fig. 4.2.13: A diverging/converging one, a converging/diverging nozzle, and a purely diverging and purely converging configuration. The converging parts are limited such that no more than 35% of the cross-sectional area are blocked: Otherwise, the reflected pressure waves become too strong, and combustion no longer is homogeneous. See fig. 4.2.2 for the reference case with constant cross-sectional area: There, 30% of the tube are filled in each cycle, pressure peaks at a dimensionless value of 3.2, and the cycle length is  $\Delta t = 1.58$ .

In the first test case with a diverging/converging configuration, ignition is no longer homogeneous. Instead, an impinging pressure wave ignites the mixture. Cycle length is  $\Delta t = 1.7$ , and about 20% of the tube are filled with fuel upon ignition. The second test case with the nozzle manages to fill 40% of the tube, and has a cycle length of  $\Delta t = 2.25$ . In the diverging case, the entire domain up to the diffuser is filled with fuel (60%) upon ignition and cycle length is  $\Delta t = 1.9$ . Finally, the purely converging test manages to fill

30% of the tube and has a cycle length of  $\Delta t = 2.25$ .

A purely diverging configuration clearly is the most beneficial. It can be used to speed up recharging and for using larger charges in general, making the process more robust. The placement of the diverging part at 60% of the tube is optimal in the sense that placement further downstream does not further increase the volume of the charge upon ignition. On the contrary, only a smaller charge can then be injected, because the low-pressure wave that is reflected from the diffuser then needs longer to arrive at the upstream end. Different area ratios have the expected effect: For ones closer to unity, the process becomes more like the constant-area one, for ratios closer to infinity, the process becomes more like it would look like if it was a constant-area simulation with a shorter pipe.

#### 4.2.7. Fuel Injection at Multiple Axial Positions

Since in a SEC, the acoustic timescale must be comparable to the auto-ignition delay time, machines in a real-world scenario cannot be arbitrarily large, and sound speeds are always between 500 m/s and 1000 m/s for relevant temperatures, auto-ignition delay times will in a realization of the process always be in the order of a few milliseconds. The stratification must be created within this time, and since it is in a real application created by controlling the amount of fuel that enters the system, a proportional valve that can be actuated on time intervals at least one order of magnitude smaller than that must be used. Such valves are not readily available, and therefore alternatives have been discussed in the project. A solution that comes with a conceptual change is the idea to inject fuel at multiple, axially distributed positions. Each of the valves then needs only provide the fuel for a smaller, partial stratification. This concept has the additional advantage that shorter auto-ignition delay times are possible, because the fuel does not have to support a long residence time in the tube to reach its final position within the stratification.

In this section, a preliminary investigation of the concept is presented, with the aim of showing that it is in principle possible to establish a resonant, pressure gain process. Injection has been modeled as follows in the investigation: The simulation was formally extended to two dimensions, but without assigning a momentum coordinate to the second dimension and without extending the numerical domain into the new dimension. (That is, a  $n$  cell 1D domain becomes a  $n \times 1$  cell 2D domain.) Spatial operator splitting was used, as has been introduced in section 3.4.2. In the split-step solving in new direction, ghost cells according to a rigid wall slip boundary condition were added everywhere except at the inlets, where the ghost cell states were determined in the same way as for the upstream boundary condition in the one-dimensional simulation: A given state with supply pressure is isentropically, isenthalpically expanded to the pressure within the tube. Momentum in the new direction was assumed to be zero throughout the flux computation. After each time step, the resulting momentum pointing in the new direction was discarded, and the associated kinetic energy was converted to internal energy, *i.e.*, to pressure.

The simulation itself has been set up as follows: The process is assumed to take place with 1 atm surroundings and air being supplied with 1000 K. The boundary conditions in

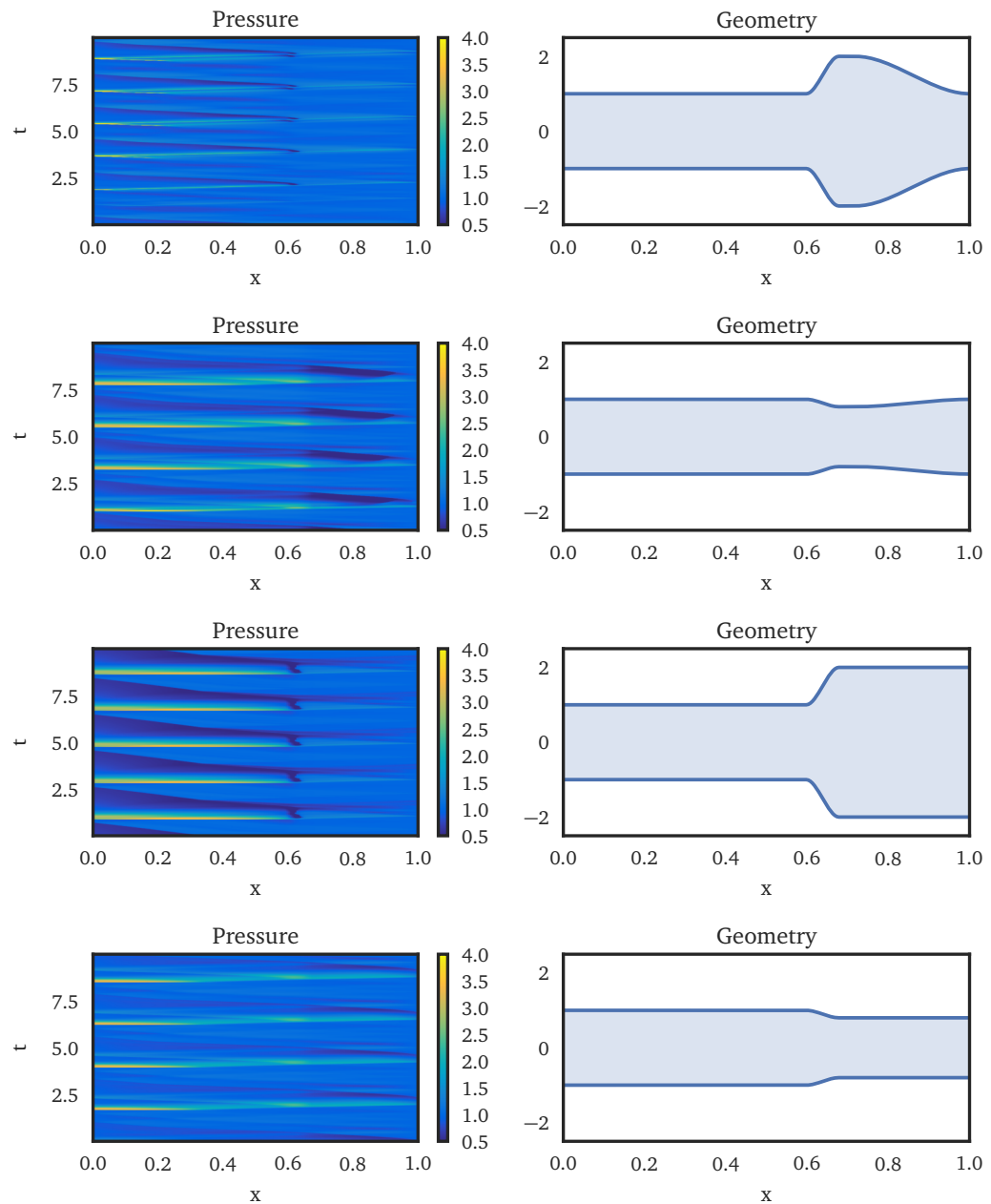


Figure 4.2.13.: Different axial variations and their effect on the SEC.

the first dimension are the same as in the earlier simulations, but no fuel is injected at the inlet. The domain is 80 cm long, and inlets are placed 5 cm, 15 cm and 25 cm from the tube's upstream end. Supply pressure for the injection is 1.1 atm, and pure hydrogen is injected at 0° C. Again, the fuel mechanism by [17] was used. Since it is a high pressure mechanism, the results of this simulation are only of qualitative nature. For this reason, and because the injection model is quite rough anyway, it was not investigated how fuel injection influences the local equivalence ratio. Instead, the value of the equivalence ratio in front of the inlet was directly used to determine whether or not to inject fuel in each time step. This way, the fuel curve could be supplied directly as a time-series of equivalence ratios. This series was the same for all inlets and fixed as a function of the time difference between opening of the upstream valve and simulation time. It has been determined as before, such that the auto-ignition delay time decreases with advancing simulation time, and then manually optimized to obtain a qualitatively homogeneous combustion.

The best way to observe both injection and ignition is in a temperature plot, which fig. 4.2.14 shows: The triangular low-temperature regions before each ignition show when and where fuel is injected. Ignition usually occurs almost simultaneously (within a few  $\mu\text{s}$ ) in three points. These ignition events appear to lead to developing detonations; at least, pressure waves with increasing strength emanate from the hotspots. Due to the small size of each of the three fuel packets, they however cannot fully develop. A peak pressure of 7 bar is reached when waves from adjacent ignitions interact. When the pressure waves reach the downstream end, they still carry a local pressure of 1.8 bar, which is sufficient to initiate a recharge.

#### 4.2.8. Multi-Dimensional Multi-Cycle Simulation

To conclude the chapter, a two-dimensional simulation of a SEC is presented. A first impression of a multi-dimensional SEC process was given in fig. 4.2.10. Here, a simulation was conducted that does not involve complex geometry. Instead, a simple rectangular domain was used. The boundary conditions were left unchanged, they have only been adjusted to the multi-dimensional case: If the average pressure at the upstream end is below the given compressor pressure, then an expansion of the inlet conditions to inner pressure is calculated and used as a boundary condition. Only the central 40% in radial direction were filled with fuel. For one, this is because a real SEC would need a buffer separating fresh fuel from the hot walls as well, for the other, this allows to observe 2D effects, which would not be as visible if the full cross-sectional area was filled with fuel.

The simulation used the ideal, single-stage fuel model, a grid resolution of  $\Delta x = 10^{-4}$ , and a  $1.0 \times 0.04$  domain in dimensionless quantities. The charging concept was the same as before.

Figure 4.2.15 shows a typical ignition in this simulation: The process runs as reliable as before in the 1D examples. There are strong residual pressure waves oscillating in radial direction though, creating turbulence that disturbs the shape of the charge. With the ideal fuel model, this effect does however not suffice to significantly disturb the auto-ignition process: Only a small fraction of the charge at its boundary ignites too late.

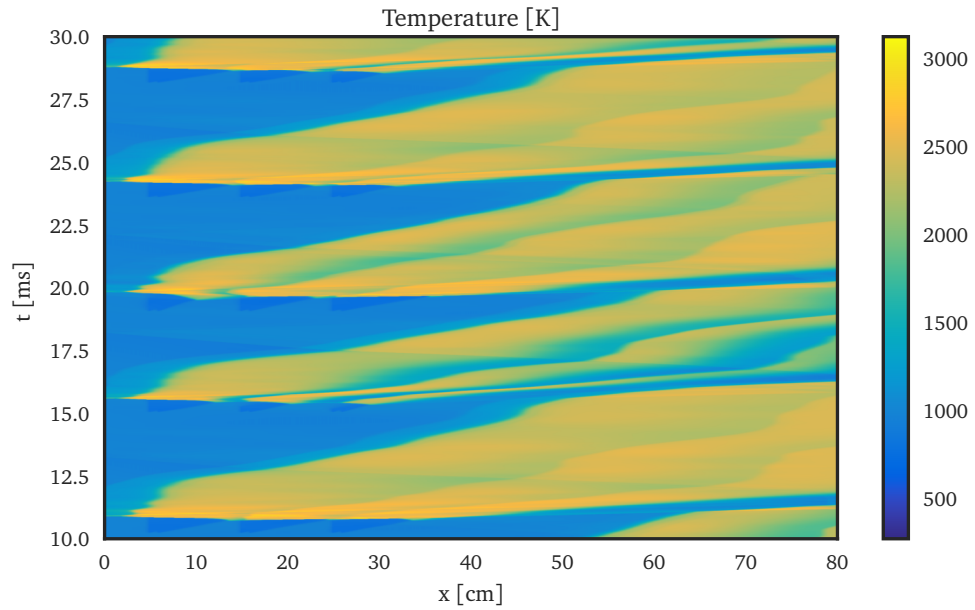


Figure 4.2.14.: Temperatures in a H<sub>2</sub>-SEC with injection at multiple axial positions. Injection may be observed through the temperature drop due to the injected fuel having a lower temperature than the air.



Figure 4.2.15.: Qualitative plot of a typical ignition in a 2D SEC without geometry.

A 3D simulation of the process, using the same concepts, showed the same complications: Since the process now involves strong pressure waves oscillating between the tube's walls, orthogonal to the axial direction, turbulent mixing can no longer be neglected. This is in particular visible in the buffer of fresh air mixing with the exhausts, necessitating a much larger buffer, which in turn reduces the charge's size and increases the cycle length. Starting ignition once the first 30 % of the tube have been cleared proved to be a good choice for obtaining a reliable process in which the charge is not deformed strongly anymore. This results in a cycle length of about  $\Delta t = 1.54$  and roughly 20 % of the tube being filled with fuel every cycle.

### 4.3. Intermediate Conclusion

The chapter started off by posing the questions whether a SEC can be achieved, both in theory and experiment, and how far from the ideal case one may operate without running into new problems. Encouraging answers have been given to all of them:

The SEC performs as expected, and its realization is predominantly a technical question. Numerically, an optimization of a stratification using (mostly) arbitrary fuels and operating conditions towards the idealized process is entirely possible.

An ideal fuel has the property that auto-ignition delay times do, over a range of about 100 K, only change on the order of one excitation time per Kelvin. If such a fuel can be found, then a SEC can very likely be realized, and is surprisingly robust. Multi-stage ignition must however be taken into account, so a control approach to the creation of suitable stratifications is still required. Perturbation of ideal fuel stratifications showed that the accuracy with which the stratification is created should be such that a spatial gradient in auto-ignition delay times never results in an auto-ignition wave that is slower than the CJ velocity. In particular, results by Gu *et al.* [35], quantifying admissible slopes of such gradients, could be reproduced. A simulation of a SEC using H<sub>2</sub>, a rather reactive fuel, concluded the one-dimensional process simulations, demonstrating that under idealized conditions, it is even possible to dispense with the fuel requirements.

The one-dimensional SEC calculations have been extended to multiple space dimensions. It has been shown that, with simple geometries, the performance is comparable to the 1D process, although turbulence might necessitate larger air buffers separating fresh fuel and exhaust gases. If complex geometries are present, then the geometry's effect must however be taken into account.

Extensions of the concept were preliminarily investigated: Influencing the charging process using axial variations is possible, but apparently does not come with large benefits. This assessment might however change once one takes off-design operation, in particular failed ignitions, into account. Injection of fuel at axially distributed inlets remains a promising concept: A first investigation produced a quite homogeneous ignition without any further optimization. It has however been conducted at high air temperatures and using a very simple injection model. Further studies should be conducted in this regard.



## 5. Concluding Remarks

Constant volume combustion in gas turbines is traditionally approximated by means of detonative combustion. While giving the benefits of (approximate) CVC, detonative processes pose new challenges: In a PDC, the initiation of a detonation requires a DDT. The longer the DDT length, the lower the efficiency. On the other hand, to achieve short DDT lengths, complex obstacles must be introduced into the main air path that require cooling and reduce mechanical integrity. Detonations generate strong shock waves that pose further stresses on the materials. They also generate much kinetic energy, and it is unclear how to convert more than a fraction of that energy to mechanical work in the turbine. The Rotating Detonation Engine mitigates these problems somewhat by maintaining a rotating detonation wave, but the principal problems associated with the strong shock wave remain.

The SEC promises to avoid these problems while still approximating CVC. Its clever recharging concept on top of that resolves the issue that one might have to charge against a positive pressure gradient if static pressure builds up at the outlet by utilizing the combustor as a resonant pipe. In the first phase of CRC 1029, the process has been investigated for the first time. This thesis contributes to its investigation.

Chapter 1 introduced the SEC as a fragile process with high demands on accuracy in its realization. It has been argued that the insights that can be gained from its simulation are crucial to recognizing, understanding and eliminating sources of failure in experiments.

Its active use of controlled auto-ignition is what makes simulations challenging: While it is mathematically easy to describe an auto-ignition event in a global reaction, resolving the detailed behaviour and interaction with gas dynamics does in general require extensive models, which makes computations expensive and creates stability issues at contact interfaces. Large models are especially required for complex fuels, and the decision to use a fuel with NTC behaviour to remove as much of the temperature dependence as possible from the problem necessitates the use of such fuels. To allow to perform quick calculations of qualitative nature, chapter 2 concerned itself with model reduction for detailed models of SEC capable fuels and introduced completely new models for fuels with ideal SEC properties: An ideal SEC fuel has an adjustable auto-ignition delay time, with the adjustable parameter such that auto-ignition delay time is user-controllable but does not change due to gas dynamics or heat transfer. The two models for such fuels are based on the insight that if ignition is independent of temperature, it must be governed by a different physical process than the reaction phase where energy is released; hence, the description of both processes may be decoupled, and the most efficient one used for each part. The models perform considerably faster than the ones obtained by traditional reduction methods while still providing an adequate description of the physical process in the case of a working SEC. For the description of off-design operation, they

are however inadequate and require adjustment. The chapter furthermore introduced a technique for obtaining optimal fuel blends for an experimental realization of the SEC, given a set of possible fuel components, and presented the ideal choices for the case of an atmospheric, single-shot SEC experiment, which has been conducted at Technische Universität Berlin.

The simulation of the gas dynamics within a mixture of different, compressible gases is a challenging task. Not only are the common pitfalls related to systems admitting shock waves present; in addition, energy transfer between gases obeying different equations of state can lead to (seemingly) unphysical pressure and temperature fluctuations. In the worst case, simulations can indeed produce entirely wrong results. The intended purpose of the present SEC simulations allowed to choose robustness over exactness: The solver developed in chapter 3 yields reliable results in all situations relevant to SEC simulations, though it introduces some amount of numerical diffusion to reach this goal. A benefit of this choice is that the resulting simulation code can, and has been, safely handed over to inexperienced users, who can use it without having to worry too much whether the results of their computations are valid. To support the claim of robustness by more than examples, the chapter gave proofs for the results that lead to the formulation of the solver. They are extensions of results that other authors gave for perfect gases only.

A benefit of the ideal fuel model is that results obtained from simulations that use it are valid for all fuels that behave sufficiently close to the model. This allows to use it to make statements that help to actually find such fuels. Chapter 4 conducted experiments using it and found several promising results. In particular, the original claim that it would suffice to find a fuel with nearly temperature-independent auto-ignition delay time over a range of 100 K has been verified. Numerical experiments using real fuel models showed that realization of the SEC is primarily a technical question: If the system's state is known exactly, then it is possible to calculate a stratification such that even with a reactive fuel like hydrogen, a reliable SEC can be achieved.

As a result of the aforesaid actions, it is now known that a SEC is realizable from a theoretical perspective, and a robust simulation code for the investigation of its behaviour is available. General strategies for determining how fuel should be injected into the primary air flow and for choosing fuel blends were introduced and can be applied once a technical realization of the process has progressed sufficiently.

The numerical investigation was concluded with a presentation of preliminary results on extensions to the concept: By replacing the cylindrical combustion tube with a solid of revolution, the acoustics within the tube can be influenced to ease recharging. While this eventually proved unnecessary in the context of the idealized investigation at hand, this change might become relevant for partial-load settings, where the magnitude of the pressure waves might otherwise be insufficient for recharging. A multi-dimensional simulation showed that charges that are not radially symmetric exhibit a more complex behaviour that necessitates further investigation as well, though the first results look promising. Fuel injection at multiple axial positions has been simulated using a simple model for orthogonally connected domains. The same model can furthermore be used to simulate networks of interconnected 1D domains, as for example a series of SEC tubes connected to an axisymmetric turbine plenum, which is one of the specified tasks of the

---

second phase of CRC 1029.

The most important step from here in the theoretical investigation is however to develop a concept for initiating the process. Consider a traditional gas turbine using the Joule cycle at rest. To start the turbine, it does not in general suffice to establish a flame within the combustion chamber. In the resting system, the pressure ratio is unity, and therefore the expanding air downstream from the flame cannot exert much force on the turbine blades. Likely, the force is insufficient to overcome friction. External means must hence be used to bring the compressor to a speed where the pressure ratio is at least such that the mechanical work exerted on the turbine suffices to maintain the speed even if the starting device is disconnected. At this point, the engine can be brought to full speed by increasing fuel mass flow.

Starting a SEC is more complex. It requires higher initial pressure ratios, because the compressor outlet temperature must be within the auto-ignition regime. The process furthermore requires higher velocities, because a stratification must be created within a short time. The initial idea is to start off with the Joule cycle. In operation, the pressure ratio already is sufficiently high. To reach the necessary velocities, fuel supply is pulsated such that a resonant pressure wave establishes within the combustion tube. Once it has sufficient strength, operation is switched to SEC mode. Whether this concept suffices is subject to investigation in the project's second phase as well.

From a theoretical point of view, a solution to this problem will, in combination with the results from this thesis, provide all the necessary ingredients for building a SEC-based gas turbine with substantially increased efficiency. The devil however is in the detail: Many aspects that can be idealized in a mathematical description or calculated from the data of a simulation in real time require smart engineering when it comes to the process's experimental realization. As of now, there are already several open questions, and it is certain that several more will come up in the future. This will probably require further theoretical investigation and refinement of the existing models. It will also raise entirely new theoretical questions.

It is safe to say that the future development of the SEC promises to be exciting.



# A. Overview Over Theoretical Prerequisites

## A.1. Thermodynamics

This section will give a brief introduction into thermodynamics. Most of what is written here is physical folklore, and the arguments are deliberately made on a basic level to simplify the presentation. For a thorough introduction, [48, 49] are recommended.

Thermodynamics is the field of physics that concerns itself with the study of heat, temperature and their relation to other physical quantities. It is a very elementary perception to “feel cold or hot”, and thus, heat as a concept has been known for a long time. A well known early explanation attempt is Empedocles four-element theory, stating that fire is one of the elementary elements that every substance is made from. The systematic study of the physical backgrounds, however, had not been possible until the advent of vacuum pumps around 1650 [59]. They allowed experimentalists to find several empirical relations:

Robert Boyle found in 1662 that the force exerted by an amount of gas at a constant temperature  $T$  is inversely proportional to its volume  $V$ . Force exerted by a volume of gas is known as *Pressure*  $p$ , measured in *Pascal* with units  $\text{N/m}^2$ , and the mathematical expression for the law is

$$p \propto \frac{1}{V}. \quad (\text{A.1.1})$$

Jacques Charles found in 1787 that if, on the other hand, pressure is kept constant, a fixed amount of a substance increases in volume as it becomes hotter. Anders Celsius had already in 1742 introduced the temperature scale that is commonly used today<sup>1</sup>, and so Charles was able to formulate his law as

$$\Delta V \propto \Delta T. \quad (\text{A.1.2})$$

Contrarily to everyday life, in science, it is customary to use Lord Kelvin’s absolute temperature scale, which scales like centigrade, but is shifted such that  $0\text{ K} = -273.15^\circ\text{ C}$ , which is the lowest possible temperature. Using this scale, the stronger statement  $V \propto T$  holds.

In parallel to these theoretical investigations, endeavors were taken to create efficient machines that could convert heat into work. The steam engine is a well-known example; the first practical one was patented in 1698. It was soon found that not all heat could

---

<sup>1</sup>Actually, Celsius introduced the scale such that water boils at  $0^\circ\text{ C}$  and freezes at  $100^\circ\text{ C}$ . It were Jean-Pierre Christin and Carolus Linnaeus who later independently reversed it.

be put to use, but that some was inevitably lost. Rudolf Clausius in 1850 introduced the concept of *entropy* to quantify the “usefulness” of heat in a system.

The mathematically most satisfactory definition of entropy was only found later, when statistical physics restated thermodynamics using a derivation from first principles: It regards thermodynamics as a statistical description of macroscopic effects of an ensemble of particles obeying (in the simplest case) Newton mechanics. A statistical description requires a density function, describing how many particles can be found in which position of the classical phase space. Denote the distribution function by  $\Gamma$ , such that  $\Gamma(V)$  is the probability to find a particle in the volume  $V$  within the phase space. By Liouville’s theorem, volumes in phase space do not change their size under time evolution, so  $\Gamma(V)$  is a conserved property. Since  $\Gamma$  is a probability distribution,  $\Gamma(V \oplus U) = \Gamma(V)\Gamma(U)$  holds, making  $\log \Gamma$  an additive function. It is known that in classical mechanics, only energy and momenta have these properties, and since momentum is already included in the phase space,  $\log \Gamma$  must depend only on energy. For convenience, one now defines

$$S = k_b \log \Gamma, \quad (\text{A.1.3})$$

where  $k_b$  is *Boltzmann’s constant*, and fixes the relation to energy  $E$  by defining temperature  $T$  as

$$dE = T \, dS. \quad (\text{A.1.4})$$

Further investigations show that these definitions coincide with the earlier definitions of entropy and temperature.

Equation (A.1.4) holds for a closed system, but in general, a system has surroundings on which it exerts a force, as Boyle’s law states above. Some energy must be used to make room for a system in the first place, and must be accounted for as well. By inserting it into the equation, one arrives at

$$dE = T \, dS - p \, dV. \quad (\text{A.1.5})$$

This is the fundamental relation of thermodynamics mentioned in the introduction.

Assume that the volume of a thermodynamic system is fixed. The amount of heat required to change its temperature by one degree may then be defined as

$$C_v = \left( \frac{\partial E}{\partial T} \right)_{V=\text{const}} = \left( T \frac{\partial S}{\partial T} \right)_{V=\text{const}}. \quad (\text{A.1.6})$$

This quantity is named the *heat capacity at constant volume*.

By means of a Legendre transformation, other energy potentials may be defined, where other quantities are held constant:

$$dH = T \, dS + V \, dp \quad (\text{A.1.7})$$

defines the *enthalpy*  $H = E + PV$  of a system, and the heat capacity that arises if  $p$  is held constant,  $C_p$ , is called the *heat capacity at constant pressure*.

If one combines Charles and Boyles observations, the formula

$$pV = \tilde{R}T \quad (\text{A.1.8})$$

arises, where  $\tilde{R}$  is an unknown, constant proportionality factor. It is called the *ideal gas law*. By combining both the ideal gas law and the fundamental relation, the value of  $\tilde{R}$  may be determined: In differential form, the ideal gas law is

$$V \, dp + p \, dV = \tilde{R} \, dT. \quad (\text{A.1.9})$$

For the difference of both formulations of the fundamental relation hence

$$dH - dE = V \, dp + p \, dV = R \, dT. \quad (\text{A.1.10})$$

Since the right hand side involves neither pressure nor volume, the heat capacity expressions may be substituted, giving

$$(C_p - C_v) \, dT = dH - dE = R \, dT. \quad (\text{A.1.11})$$

So  $\tilde{R} = C_p - C_v$ . Further research shows that

$$\tilde{R} = mR = m \frac{\hat{R}}{M} = nk_b N_a \quad (\text{A.1.12})$$

where  $m$  is the mass in the system,  $R$  is the *specific gas constant*,  $\hat{R} = 8.314 \text{ J/mol}\cdot\text{K}$  is the *universal gas constant*,  $M$  is the mass of one mole of the gas under investigation,  $n$  is the amount (in moles) of particles in the system,  $k_b$  is again Boltzmann's constant, and  $N_a$  is Avogadro's constant, defining the unit mole by fixing an amount of particles that constitute one mole.

In a common simplification, one often assumes that  $C_p = C_p(T)$ , allowing to integrate  $C_p \, dT$  directly. Fluids for which this property holds are called *thermally perfect*, and for gases it is often valid to use this approximation.  $C_p$  is then measured experimentally at a fixed pressure, normalized by mass or particle count (which one denotes by using lower case letters, *i.e.*,  $c_p$  instead of  $C_p$  and  $e$  instead of  $E$ ) and published either tabulated for various temperatures or as coefficients of an interpolation. Since  $c_v$  may be calculated from  $c_p$  using the relation derived above, all the information that is required to perform calculations is then given.

It is also customary to retain this normalization and work with *mass density*  $\rho$  instead of mass, and specific volume  $1/\rho$  instead of volume.

A further simplification is the assumption that the heat capacities are constant. Gases for which this property holds are called *calorically perfect*. The approximation usually holds only if one stays within a small temperature range. If the heat capacities are constant, then from the ideal gas law a much simpler relation of all quantities may be derived:

$$p = \rho RT = \rho (c_p - c_v) T = \rho \left( \frac{c_p}{c_v} - 1 \right) e. \quad (\text{A.1.13})$$

One typically defines  $\gamma = c_p/c_v$ , where  $\gamma$  is called *isentropic exponent*, and sometimes speaks of a  $\gamma$ -law gas.

All further thermodynamic relations that are used in the thesis may be derived from the fundamental relations.

## A.2. Finite Volume Methods

This section gives a short introduction to finite volume schemes. For detailed derivations including proofs and information on convergence and stability, see [53, 71].

Consider a one-dimensional equation in conservation form,

$$\frac{\partial q}{\partial t} + \frac{\partial}{\partial x} f(q) = 0. \quad (\text{A.2.1})$$

As has been laid out in the introduction, the natural form for such equations is their integral formulation, because it expresses directly that a quantity within a volume may only change due to some flux through the volume's boundary. It may be obtained by integrating in space and time over some test-volume  $[x_0, x_1] \times [t_0, t_1]$ :

$$\int_{x_0}^{x_1} q \, dx \Big|_{t_0}^{t_1} + \int_{t_0}^{t_1} f(q) \, dt \Big|_{x_0}^{x_1} = 0. \quad (\text{A.2.2})$$

It is clear that this formulation admits more general solutions, because it does not require differentiability of the solution  $q$ . Now consider how this formulation may be used to numerically solve the equation system:

Discretize the domain under consideration into intervals

$$[x_0, x_1], [x_1, x_2], \dots [x_{M-1}, x_M]. \quad (\text{A.2.3})$$

Define by

$$q_m(t) = \frac{1}{x_{m+1} - x_m} \int_{x_m}^{x_{m+1}} q \, dx \quad (\text{A.2.4})$$

the average of  $q$  in each test volume and use it as a numerical approximation to  $q$ . For a discrete time step  $\Delta t$ ,

$$q_m(t + \Delta t) = q_m(t) - \frac{1}{x_{m+1} - x_m} \left( \int_t^{t+\Delta t} f(q_{m+1/2}) \, dt - \int_t^{t+\Delta t} f(q_{m-1/2}) \, dt \right) \quad (\text{A.2.5})$$

then holds, where  $q_{m\pm 1/2}$  is some intermediate value at the boundary between two intervals that still needs to be defined. If the right hand side integrals can be solved, then the equation defines a numerical scheme. Such a scheme interpreting the numerical variables as averages over some volume rather than point values is called a *finite volume scheme*.

The question now is how to make sense of the integrals, and of the value of  $q$  at the boundary between two intervals. This gives rise to the study of *Riemann problems*. Such problems are initial value problems for (A.2.1) of the form

$$q(x)|_{t=0} = \begin{cases} q_\ell & \text{if } x < 0, \\ q_r & \text{if } x > 0. \end{cases} \quad (\text{A.2.6})$$

Riemann problems are exactly those problems which arise on each of the boundaries between intervals in the numerical discretization. For the special case of equations which have a hyperbolic linearization, that is, where  $\nabla f$  is diagonalizable with real eigenvalues, the solution consists of several waves originating from  $x = 0$  with finite velocities given by the eigenvalues of the matrix, each carrying a jump that is given by the associated eigenvector. Figure 3.1.1 exemplary shows such a wave structure for the Euler equations.

This has several implications: Most importantly, the finite velocity of the waves allows to choose the time step size  $\Delta t$  such that the solutions of adjacent interfaces do not interact. This time step restriction is called the CFL condition. If a general solution strategy for the Riemann problem is known, one can therefore expect a stable numerical scheme as long as this condition is fulfilled. Secondly, if  $\nabla f$  changes sufficiently slowly with  $q$ , the waves originating from  $x = 0$  will approximately maintain velocity and the jumps they carry for some time. This allows to regard the solution to the Riemann problem as a self-similar function in a single variable,  $q(x/t)$ , i.e., as constant along rays originating from  $x = 0$  that lie in between the waves. In particular, this means that the solution in  $x = 0$  is constant, simplifying the integrals in eq. (A.2.5) to a product of the step size and the flux function evaluated at the solution in  $x = 0$ .

The solution of the Riemann problem for the reactive Euler equations is discussed in section 3.1. Often, it is computationally too expensive to calculate the correct solution, and so one uses *approximate Riemann solvers* instead, that simplify the Riemann problem in some fashion to obtain an approximation to the solution. The HLLE solver introduced in section 3.2 is such an approximate solver.

The method defined above is exact in time, but only of first order in space. One may obtain a higher order approximation by, instead of regarding the Riemann problem  $q_\ell = q_m$ ,  $q_r = q_{m+1}$  to obtain  $q_{m+1/2}$ , using values interpolated from several adjacent cell averages as input to the Riemann problem. This creates issues close to discontinuities, where  $q$  does not admit an interpolation. They are resolved by detecting such situations and dynamically switching back to first order. This process is called *Limiting*. For a first order, linear approximation, the resulting scheme this is called a MUSCL method. Details are discussed in section 3.4.1.



## B. Code Documentation

The theoretical foundation of the SEC simulation code has been laid out in chapters 2 and 3. This chapter documents the use of the software, and is intended for its users. To readers with a background in computer science, the section on the technical background of some design choices may be of interest. The code can be obtained from <http://git.imp.fu-berlin.de/sfb1029/code><sup>1</sup>. Installation instructions are given in the repository.

### B.1. High-Level Usage

The SEC simulation was developed for MATLAB, with parts of the computation outsourced to C++ via the MEX interface. Key ingredients to all simulations are the *configuration*, defining which flux to use, domain size, boundary conditions, *etc.*, and the *state*, which is a contained representation of the entire simulation's state at each time level. The code is specialized for solving reactive fluid dynamics, but abstracts away from the equation of state and chemical kinetics implementation. This abstraction is contained in the configuration, and automatically set if a configuration is initialized through an appropriate wrapper function. A typical driver script for a simulation looks like this:

```
config = IgnitionDelayKinetics(); % Initialize a configuration using
                                  % the ideal, single-stage fuel model
config.grid.dx = 1e-3;           % Use 1mm grid resolution

% Set up initial conditions. States are column vectors.
reactive_state = config.kineticsif.setTPX(1, 1, 'F:1');
reacted_state = config.kineticsif.setTPX(4.7, 4.7, 'P:1');
config.iv = [ repmat(reactive_state, 1, .4 / config.grid.dx), ...
             repmat(reacted_state, 1, .6 / config.grid.dx) ];

% Use a rigid wall slip boundary condition for the left wall;
% the right one defaults to a continuous boundary condition
config.boundary(1).fn = @ReflectingBoundary;

% Run the simulation. Per default, this displays a live plot window,
% and runs until the window is closed. The final state is returned.
rest = RunSimulation(config);
```

---

<sup>1</sup>As of 2016. Should this website be unavailable, contact the author to obtain the code.

Configuration objects (`config`) are struct instances. They contain not only settings regarding the numerics, but also for output/backup control, heatmap generation, plotting and video generation, and so forth. The individual configuration options are listed and documented in the file `lib/BaseConfig.m`. The `kineticsif` substructure contains function handles to the kinetics implementation. The most important function to end-users is `setTPX`, which, given a temperature  $T$ , pressure  $P$  and volume fraction string  $X$  (in the form “`species: amount, species: amount, ...`”), returns a state vector for these conditions. Boundary conditions are assigned via the boundary structure array, in the order left, right, top, bottom, front, back, by assigning a function handle to the `fn` property. Specific boundary conditions may/might require to assign more properties to the boundary. Table B.1.1 lists the available boundary conditions, kinetics implementations and important auxiliary functions. `RunSimulation` is the main entry point into the code. It takes a configuration, an optional initial state (`rest` from an earlier simulation) and an optional callback that is invoked after each time-step, and which can cancel the simulation, as arguments.

A `rest` is a structure object, with time  $t$ , grid data `data`, and further, self-explanatory fields. The numerical domain is represented as a (multidimensional) array, with variables for a single state occupying the first dimension, and spatial extent in the following dimensions. In the first dimension, variables are stored as follows:

$$\begin{pmatrix} \rho \\ \rho \vec{u} \\ \rho E \\ \rho \vec{Y}_{1\dots(n-1)} \\ p \\ T \\ c_p \\ c_v \end{pmatrix} \quad (\text{B.1.1})$$

Named indices stored in `config.i` and `config.v` may be used to access these properties by name; this is also documented in `BaseConfig.m`.

If `FlamemasterKinetics` is used, then chemical kinetics are handled by a binary solver, available as a MEX file. Available mechanisms are the files listed in the `mex/flamemaster/reactor/mechanism` folder. If the system has Python available, then a Python module, `pyflamemaster`, is compiled together with the MEX file, which can be used to directly use the mechanisms in 0D isochoric reactors, with a syntax similar to that of the open source chemical kinetics library Cantera; it is documented separately below.

## B.2. Detailed Program Flow and Advanced Features

When a simulation is started using `RunSimulation`, the function first performs plausibility checks and initializes a `rest` state variable if none was given. It then repeatedly invokes `EulerChemTimestep` to perform a simulation time step, and afterwards performs the auxiliary tasks that were specified in the configuration. If `config.mpi.enabled` is set, it

Name	Use
<b>Kinetics implementations:</b>	
FlamemasterKinetics(filename, nDimensions)	Access to compiled, ideal gas kinetics mechanisms
IgnitionDelayKinetics(nDimensions)	The ideal fuel model from section 2.2.1
PerfectGasKinetics(gamma, nDimensions)	An unreactive, perfect EOS gas
TwoStageIgnitionDelayKinetics(nDimensions)	The ideal two-stage fuel model from section 2.2.2
<b>Boundary conditions:</b>	
ContinousBoundary	Continuous extension of the domain towards the boundary
ExpansionBoundary	Instantaneous expansion into a fixed size plenum (see section 4.1.1)
PeriodicBoundary	Periodic boundary condition (must be explicitly set on both sides)
PressureValveBoundary	A valve with fixed supply pressure, acting as a rectifier (see section 4.1.1)
PressureValveForIgnitionDelayKineticsBoundary	As PressureValveBoundary, but already specialized to provide the ideal fuel curve required for use with IgnitionDelayKinetics
ReflectingBoundary	A rigid wall slip boundary condition
<b>Auxiliary functions:</b>	
PostShock(config, downstreamState, shockSpeed)	Solve the shock conditions
SetVelocity(states, velocities)	Assign velocities to a set of states, altering kinetic energy accordingly
ZNDInitialData(config, downstreamState)	Calculate initial data for a ZND detonation
config.kineticsif.moleFractions(states)	Return the volume fractions X for a given set of states
config.kineticsif.massFractions(states)	Return the mass fractions Y for a given set of states
config.kineticsif.speciesNames()	Return the names of the species in the mechanism, in order
config.kineticsif.advance(states, 0)	Update the primitive variables from the conservative variables in a set of states

Table B.1.1.: Kinetics implementations and boundary conditions for the SEC simulation.

invokes another instance of MATLAB using `mpirun` to perform the actual calculation in a parallelized fashion using Message Passing Interface (MPI), and performs the auxiliary tasks in a callback from the calculation. The domain is, in this case, distributed in equally sized chunks along the first axis to the different nodes, and the four cells from each boundary are exchanged between the nodes before each time step. This feature does not require a license for the parallel computing toolbox, but still one license per node — see appendix B.4 for information on the implementation.

`EulerChemTimestep` first calls `TimestepSize` to obtain the step size for the next time step. `TimestepSize` uses the CFL condition from `config.cf1`, and optionally the reactivity (see `config.chem_dt_lim`) to limit the step size. It takes boundary conditions into account, and, if MPI is used, agrees with all nodes on one step size. In even time steps, a chemistry time step is then taken by calling `config.kineticsif.advance(data, dt)`. This call also updates primitive variables from the conservative ones. Since it might affect the CFL condition, it is reevaluated afterwards and a reduced step is taken instead, if necessary. In odd steps, the chemistry step is performed at the end of the function. This implements Strang splitting. If axial variations are in place, *i.e.*, a quasi-1D system is solved, with the cross-sectional areas being provided in `config.grid.A`, the system is then transformed into the equation system from section 1.2.4. The code then loops over all dimensions involved in the system, with the order permuted in each step to achieve Strang splitting. It first permutes the dimensions such that the dimension in which fluid dynamics is currently being solved is always the first spatial dimension. Then, boundary conditions due to the problem’s geometry are assigned: If `config.grid.geometry` is a level-set function, then values with positive sign are considered solid. Rigid wall slip boundary conditions are applied at the boundary. Finally, the actual boundary conditions as defined in `config.boundary` are applied, a fluid dynamics time step is taken using `EulerTimestep`, and all permutations and ghost cells are revoked. After all this has been done, axial distributed inlets that have been defined in `config.lowerBoundary` are applied similarly like they would be in a real 2D simulation; see section 4.2.7 for details.

`EulerTimestep` is the function responsible for solving the Euler equations. Depending on the value of `config.timestepping`, it uses different time marching schemes. The default is to use explicit Euler steps. It calls `Reconstruct` to reconstruct function values at all cell boundaries, and then `NumFlux` to calculate the numerical fluxes.

`Reconstruct` performs second order (or, depending on the value of the reconstruction setting `config.reconstruct`, higher order ENO) reconstruction in primitive variables. To obtain conservative state vectors from the primitive variables, the function `config.kineticsif.recSetPUTY` is used. It takes pressure, velocity, temperature and mass fractions as arguments, in a column vector.

`NumFlux` implements the different numerical flux variants that were discussed in chapter 3, depending on the value of `config.flux`. Whenever the function value of the equation’s flux function is needed, `Equation` is invoked.

### B.2.1. MEX Interface to the Kinetics Solver

The chemical kinetics interface has been constructed with the chemical kinetics tool *Flamemaster* [60] in mind. It features a tool called *ScanMan*, that is able to produce C source files from mechanism specifications containing the right hand side function of the chemical reaction system and a function to evaluate the heat capacities, energy and enthalpy functions. The signatures are as follows:

```
void ComputeProductionRates(double *cdot, double *w, double *k,
                           double *c, double *M, double T, double pressure);
void ComputeThermoData(double *h, double *cp, double T, double *s);
```

Therein, *c* are the species concentrations, *cdot* the time derivatives of the concentrations, and any variables that do not have obvious meaning should hold auxiliary memory for internal use within the function.

At the core of the kinetics solver is a class named *Reactor*, which is able to load shared libraries exporting the two symbols from above and calculate the time evolution of a 0D isochoric reactor. It does this by using an external ODE solver. Currently, *cvode* and *radau15* are implemented (see section 2.4), but extension to other solvers is straight-forward. The reactor class furthermore handles thermodynamics, *i.e.*, calculation of the thermodynamic variables from one another. The MEX interface wraps the reactor class with a layer of abstraction, to allow extension with other solvers, and exposes a single call to MATLAB, *Flamemasterif*, which is called by the functions defined in *FlamemasterKinetics.m*.

## B.3. PyFlamemaster Interface to the Kinetics Solver

The *Reactor* class from appendix B.2.1 is exposed to Python via *pyflamemaster*. In addition to the reactor interface, which is documented inline using the Python documentation system, it ships with auxiliary functions useful in the context of SEC calculation. The following is an example show case for the additional features:

```
# Initialize a reactor with the 33 species DME mechanism
reactor = pyflamemaster.Reactor("dme_ultimate.so")
reactor.set(T=800, p=1e5, X="CH3OCH3:.33,02:1,N2:3.76")
# Calculate the auto-ignition delay times for states behind shocks of
# different strength
def tau(V):
    r = reactor.clone()
    r.setVolumeHugoniot(V)           # Move state along Hugoniot
    return r.advanceAndFindMaxdT(5.) # Solve up to 5s and return tau
Vs = linspace(0.5 / reactor.getDensity(), 1 / reactor.getDensity(), 50)
taus = map(tau, Vs)
# e.g., plot the results:
plot(Vs, taus)
```

pyflamemaster ships with a module sec, which implements the functions required to perform the fuel blend investigations from section 2.3 on top of it: It allows to calculate states resulting from isenthalpic mixing of fuel and air at different temperatures, and implements a function that determined excitation times. It furthermore simplifies investigation of mixtures by automatically determining the exact amount of oxygen required for a given fuel. Again, its functionality is documented inline using the Python documentation system.

## B.4. Technical Background

This section discusses the most striking technical decisions that were made in the development of the code.

### B.4.1. Closures in MATLAB

The config variable is passed as a parameter to all functions. The alternative would be to use a global variable. It is generally considered good practise to avoid them in any paradigm that advocates encapsulation; in MATLAB, in addition, access to global variables is around 20% slower on average than if function parameters are used. MATLAB does not have variable references; any assignment or parameter is always (lazily) copied. So if one of these functions changes config, then the change does not propagate to the outside. This is an issue for some kinetics implementations that have parameters. *E.g.*, the ideal fuel model has a configurable energy release  $\Delta Q$ : If they define a parameter config.DQ, use it in a function defined inline, and return config, then any changes done by the user afterwards will not propagate back to the earlier use of config. The single exception to the pass-by-value paradigm are classes deriving from handle. They are passed by reference. struct does not derive from handle, and is a final class (*sealed* in MATLAB terminology), and hence cannot be subclassed to be a handle. A custom object deriving from handle that allows to mimic a struct exists with the dynamicprops class, but using it is twice as slow as if parameters are passed by value. The solution to this issue used in the code is enabled by MATLAB's decision to allow access to local variables of the enclosing function to inline functions. Consider the following function definition:

```
function [ myvar ] = closure_gen()
    myvar = struct();
    internal_value = 0;
    function [ x ] = getter()
        x = internal_value;
    end
    function [ ] = setter(x)
        internal_value = x;
    end
    myvar.set = @setter;
```

---

```
myvar.get = @getter;
end
```

The variable `internal_value` is a *local* variable of the function, and hence is a different variable for each invocation of the function. The functions defined inline access the variable that was defined in the invocation, and since function references are handles, *copies* of the structure still return the correct value:

```
>> a = closure_gen();
>> b = closure_gen();
>> c = a;
>> a.set(12);
>> b.set(24);
>> disp([a.get(), b.get(), c.get()])
```

```
12      24      12
```

### B.4.2. MPI Interface to MATLAB

MATLAB has two functions that (de)serialize arbitrary objects into a chunk of memory: `getByteStreamFromArray` and `getArrayFromByteStream`. With a MEX file that calls the usual MPI functions, this allowed to build a high-level MPI interface for MATLAB, where code can with simple calls share slices of array between different nodes in a simulation. Since MATLAB is usually invoked from the desktop, and not through `mpirun`, the interface adds a redirection layer: The code that first calls the MPI interface merely tells it to start other instances of MATLAB using `mpirun`, run a given function, and optionally periodically return data to the controlling MATLAB instance. This can be used, e.g., to plot a simulation's state.

Data is returned using a UNIX socket between the controller and the MPI rank 0 process. The rank 0 process must hence run on the same machine as the controlling process. It is furthermore necessary that all machines have the same endianness and address width, because no conversion is performed in the interface.

The MPI interface ships with the code and is compiled automatically if a `mpicc` is available. The SEC simulation makes use of it if the parameter `config.mpi.enabled` is set. It is easy to use it in other scopes as well: The MEX file exposes a single call, `mpi`. Subcommands are chosen by specifying a value for the first parameter. If `mpi` is invoked without parameters, it displays a description of the different subcommands. There are two possible ways to use the interface. The preferred one is the one that has been explained above. Call `mpi(1,...)` to use it. Alternatively, MATLAB may be run directly from `mpirun`. In this case, the driver script must initialize MPI by calling `[rank, world_size] = mpi(3)`. A minimal example would look like this:

```
function [ ] = test()
    % Use MPI to do some number-crunching
```

```
parameter = 1;
data = rand(2000, 2000);

% The command says: Start mpirun with parameter '-np 5' and call
% mpi_driver. Send 'parameter' to all nodes, but 'data' only to
% rank #0. Use feedback as the feedback function.
mpi(1, '-np 5', @mpi_driver, { parameter }, { data }, @feedback);

function [ ] = mpi_driver(rank, world_size, params, rank_zero_params)
% This function is executed once per rank, each in a different
% process. It could e.g. distribute rank_zero_params from rank #0
% to all other nodes, do some number crunching, and gather the
% data again. This example just sends the rank to rank #0 and
% passes it on to the controller:
if rank == 0
    result = [ rank ];
    for i = 1:(world_size-1)
        result = [ result mpi(6, i) ]; % Receive from rank #i
    end
    mpi(2, result); % Report to controller
else
    mpi(5, 0, rank); % Send the variable 'rank' to rank #0
end

function [ ] = feedback(data)
% This will output [ 0, 1, 2, 3, 4 ]
display(data)
```

The subcommands are documented in `mpi`'s help output that is displayed if the command is invoked without parameters.

It should be noted that MATLAB has a Parallel Computation Toolbox that serves the same goal. It does however try to hide the complexity of parallel computation from the user by offering `parfor` as a substitute for `for`, and tries to automate distribution among all nodes in the cluster by performing an analysis of the code in the loop. This restricts the use of several commands within such loops. For users that are already familiar with MPI, the present approach is clearly more beneficial. Both approaches however require one MATLAB license per node (not process!), which poses economic limits on possible parallelization.

#### B.4.3. MEX Kinetics Interface

Cantera is an open-source kinetics library with an existing MATLAB integration. One might hence wonder why another interface was written. The reason for this is two-fold: Cantera internally uses cvode to solve the ODE system associated with the chemistry, but

separates reactors, *i.e.*, representations of thermochemical state, from the system that is to be solved. The reason for this is that Cantera allows to solve more complex systems as well, like networks of reactors or steady 1D problems. Once a reactor enters a system, local changes to the reactor do not affect the state of the system anymore. As a consequence from this, whenever a reactor's state is updated, the system must be updated manually to reflect the update. Cantera is implemented such that, at this time, cvode is completely reinitialized, which costs time. By design, when solving the equation system from the SEC simulation, for each cell, a reactor must be updated, the system be reinitialized, and then solved. This is slow and cumbersome. The C++ interface to Cantera luckily is sophisticated enough to work around this though. The other reason for writing a new interface is that this allows to perform straight-forward, local parallelization through OpenMP. For simulations on desktop PCs, this gives a huge speed-up.

Originally, the SEC code had a Cantera interface. The Flamemaster interface was written because the mechanisms created at RWTH Aachen were made available in their custom format, and writing a new reactor implementation around it was found easier than writing a reliable converter to Cantera's format, given that they can produce a C file containing the entire right hand side of the system. Also, a precompiled, binary representation of the right hand side of a kinetics mechanism can likely be evaluated faster than any representation that requires a parser; unless great care is taken with the latter. Most users of the SEC code use Microsoft Windows, and were unable to compile the MEX interface on their own. While automatically cross-compiling the custom interface for various different MATLAB versions was very straight-forward, cross-compiling the Cantera interface was found a very complex task, and eventually the code was abandoned due to the high maintenance cost of keeping the compiler infrastructure up and running.



# List of Acronyms

<b>SEC</b>	Shockless Explosion Combustion
<b>SWACER</b>	Shock Wave Amplification by Coherent Energy Release
<b>NTC</b>	Negative Temperature Coefficient
<b>BDF</b>	Backward Differentiation Formula
<b>RK</b>	Runge-Kutta
<b>DME</b>	Dimethyl Ether
<b>QSS</b>	Quasi Steady State
<b>CFL</b>	Courant-Friedrichs-Lowy
<b>MUSCL</b>	Monotonic Upstream-Centered Scheme for Conservation Laws
<b>ENO</b>	Essentially Non-Oscillatory Scheme
<b>MC</b>	Monotonized Central-Difference
<b>DAE</b>	Differential Algebraic System
<b>HLLE</b>	An approximate Riemann solver by Harten, Lax, van Leer, and Einfeldt
<b>HLLEM</b>	An approximate Riemann solver by Harten, Lax, van Leer, and Einfeldt (with modifications)
<b>ZND</b>	A detonation model by Zel'dovich, von Neumann, and Döring
<b>CJ</b>	Chapman-Jouguet
<b>PDC</b>	Pulse Detonation Combustion
<b>ODE</b>	Ordinary Differential Equation
<b>CVC</b>	Constant Volume Combustion
<b>DDT</b>	Deflagration to Detonation Transition
<b>EOS</b>	Equation of State
<b>MPI</b>	Message Passing Interface



# Bibliography

- [1] R. Abgrall. "Generalisation of the Roe scheme for the computation of mixture of perfect gases". In: *Rech. Aéosp* 6 (1988), pp. 31–43 (cit. on p. 37).
- [2] R. Abgrall. "How to prevent pressure oscillations in multicomponent flow calculations: A quasi conservative approach". In: *Journal Of Computational Physics* 125.1 (1996), pp. 150–160 (cit. on p. 37).
- [3] R. Abgrall and S. Karni. "Computations of compressible multifluids". In: *Journal Of Computational Physics* 169 (2001), pp. 594–623 (cit. on pp. 38, 58–60).
- [4] U. E. I. Administration. "International Energy Statistics". Online; accessed 2016-05-09. 2012. URL: <http://www.eia.gov/cfapps/ipdbproject/IEDIndex3.cfm?tid=44%5C&pid=44%5C&aid=1> (cit. on p. 1).
- [5] R. F. Almgren. "High-Frequency Acoustic Waves in a Reacting Gas". In: *SIAM J. Appl. Math.* 51.2 (1991), pp. 351–373 (cit. on p. 19).
- [6] J. D. Anderson. *Modern compressible flow: with historical perspective*. Vol. 12. McGraw-Hill New York, 1990 (cit. on pp. 64, 72).
- [7] J. Barber. "A method for rising inflammable air for the purposes of producing motion and facilitating metallurgical operations". In: *British patent* 1833 (1791) (cit. on p. 1).
- [8] J. Beeckmann et al. *A reduced kinetic reaction mechanism for the autoignition of dimethyl ether*. Tech. rep. 2010 (cit. on p. 20).
- [9] A. Berkenbosh et al. "Detonation Capturing for Stiff Combustion Chemistry". In: *RANA* 95-06 (1995) (cit. on p. 25).
- [10] P. Berndt. "On the Use of the HLL-Scheme for the Simulation of the Multi-Species Euler Equations". English. In: *Finite Volumes for Complex Applications VII-Elliptic, Parabolic and Hyperbolic Problems*. Ed. by J. Fuhrmann, M. Ohlberger, and C. Rohde. Vol. 78. Springer International Publishing, 2014. Chap. Springer Proceedings in Mathematics & Statistics, pp. 809–816 (cit. on pp. 45, 47–50, 71).
- [11] P. Berndt and R. Klein. "Modeling the kinetics of the Shockless Explosion Combustion". In: *Combustion and Flame* (2016) (cit. on pp. 25, 26, 71, 79, 83, 84, 86, 89).
- [12] P. Berndt, R. Klein, and C. O. Paschereit. "A Kinetics Model For The Shockless Explosion Combustion". In: *ASME Turbo Expo 2016: Turbine Technical Conference and Exposition*. 2016 (cit. on pp. 29, 71, 86, 87).
- [13] B. Bobusch. "Fluidic Devices for Realizing the Shockless Explosion Combustion Process". PhD thesis. Technische Universität Berlin, 2014 (cit. on pp. 71, 89, 90).

- [14] B. C. Bobusch et al. “Investigation of fluidic devices for mixing enhancement for the shockless explosion combustion process”. In: *Active Flow and Combustion Control 2014*. Springer, 2015, pp. 281–297 (cit. on pp. 71, 76).
- [15] B. C. Bobusch et al. “Shockless Explosion Combustion: An Innovative Way of Efficient Constant Volume Combustion in Gas Turbines”. In: *Combustion Science And Technology* 186.10-11 (2014), pp. 1680–1689 (cit. on pp. 2, 71).
- [16] A. Burcat et al. *Combustion chemistry*. Springer Science & Business Media, 2012 (cit. on p. 10).
- [17] M. P. Burke et al. “Comprehensive H<sub>2</sub>/O<sub>2</sub> kinetic model for high-pressure combustion”. In: *International Journal of Chemical Kinetics* 44.7 (2012), pp. 444–474 (cit. on pp. 67, 93, 97).
- [18] L. Cai and H. Pitsch. “Tailoring Fuels for a Shockless Explosion Combustor”. English. In: *Active Flow and Combustion Control 2014*. Ed. by R. King. Vol. 127. Springer International Publishing, 2015. Chap. Notes on Numerical Fluid Mechanics and Multidisciplinary Design, pp. 299–315 (cit. on pp. 19, 20, 27–29, 34, 76, 87).
- [19] D. L. Chapman. “VI. On the rate of explosion in gases”. In: *The London, Edinburgh, and Dublin Philosophical Magazine and Journal of Science* 47.284 (1899), pp. 90–104 (cit. on p. 67).
- [20] S. D. Cohen and A. C. Hindmarsh. “CVODE, a stiff/nonstiff ODE solver in C”. In: *Computers in physics* 10.2 (1996), pp. 138–143 (cit. on p. 34).
- [21] H. J. Curran, S. L. Fischer, and F. L. Dryer. “The reaction kinetics of dimethyl ether. II: Low-temperature oxidation in flow reactors”. In: *International Journal of Chemical Kinetics* 32.12 (2000), pp. 741–759 (cit. on pp. 20, 21).
- [22] P. Deuflhard and F. Bornemann. *Numerische Mathematik. Band 2: Gewöhnliche Differentialgleichungen. 2. vollständige überarbeitete und erweiterte Auflage*. 2002 (cit. on pp. 34, 56).
- [23] E. W. Dijkstra. “A note on two problems in connexion with graphs”. In: *Numerische Mathematik* 1.1 (1959), pp. 269–271 (cit. on p. 23).
- [24] W. Döring. “Über den Detonationsvorgang in Gasen”. In: *Annalen der Physik* 435.6-7 (1943), pp. 421–436 (cit. on p. 66).
- [25] A. Dutt, L. Greengard, and V. Rokhlin. “Spectral Deferred Correction Methods for Ordinary Differential Equations”. In: *BIT Numerical Mathematics* 40.2 (), pp. 241–266 (cit. on pp. 34, 56).
- [26] B. Einfeldt. “On Godunov-Type Methods For Gas-Dynamics”. In: *Siam Journal On Numerical Analysis* 25.2 (1988), pp. 294–318 (cit. on pp. 38, 43, 44, 49–51).
- [27] B. Einfeldt. *Notes on a proposal*. Online, accessed in April 2016. June 2012. URL: <http://discontinuous-flow.blogspot.de/2012/06/notes-on-proposal.html> (cit. on p. 49).

- 
- [28] B. Einfeldt et al. “On Godunov-type methods near low densities”. In: *Journal of computational physics* 92.2 (1991), pp. 273–295 (cit. on pp. 44, 46).
  - [29] R. P. Fedkiw et al. “A non-oscillatory Eulerian approach to interfaces in multi-material flows (the ghost fluid method)”. In: *Journal of computational physics* 152.2 (1999), pp. 457–492 (cit. on p. 37).
  - [30] W. Ficket and W. C. Davis. *Detonation: Theory and Experiment*. 1979 (cit. on p. 67).
  - [31] S. L. Fischer, F. L. Dryer, and H. J. Curran. “The reaction kinetics of dimethyl ether. I: High-temperature pyrolysis and oxidation in flow reactors”. In: *International Journal of Chemical Kinetics* 32.12 (2000), pp. 713–740 (cit. on pp. 20, 21).
  - [32] P Graichen, M. M. Kleiner, and C. Podewils. *Die Energiewende im Stromsektor: Stand der Dinge 2015. Rückblick auf die wesentlichen Entwicklungen sowie Ausblick auf 2016*. Tech. rep. Agora Energiewende, Jan. 2016 (cit. on p. 1).
  - [33] J. Gray et al. “Thermodynamic Evaluation of Pulse Detonation Combustion for Gas Turbine Power Cycles”. In: *ASME Turbo Expo 2016*. 2016 (cit. on pp. 68, 71).
  - [34] J. Gressier, P. Villedieu, and J.-M. Moschetta. “Positivity of flux vector splitting schemes”. In: *Journal of Computational Physics* 155.1 (1999), pp. 199–220 (cit. on pp. 48, 70).
  - [35] X. J. Gu, D. R. Emerson, and D. Bradley. “Modes of reaction front propagation from hot spots”. In: *Combustion and Flame* 133.1–2 (2003), pp. 63–74 (cit. on pp. 19, 80, 83, 99).
  - [36] E. Hairer, C. Lubich, and G. Wanner. *Geometric numerical integration: structure-preserving algorithms for ordinary differential equations*. Vol. 31. Springer Science & Business Media, 2006 (cit. on p. 55).
  - [37] E. Hairer and G. Wanner. “Stiff differential equations solved by Radau methods”. In: *Journal of Computational and Applied Mathematics* 111.1–2 (1999), pp. 93–111 (cit. on p. 34).
  - [38] N. Hanraths. “Parameterstudie zur Emission bei der Simulation einer 1D-Pulsdetonationsbrennkammer mit Wasserstoff-Luft-Gemisch”. Bachelor 1068. July 2013 (cit. on pp. 68, 69).
  - [39] A. Harten, P. D. Lax, and B. van Leer. “On Upstream Differencing and Godunov-Type Schemes for Hyperbolic Conservation Laws”. In: *SIAM Review* 25.1 (1983), pp. 35–61 (cit. on pp. 38, 43).
  - [40] A. Harten et al. “Uniformly high order accurate essentially non-oscillatory schemes, III”. In: *Upwind and High-Resolution Schemes*. Springer, 1987, pp. 218–290 (cit. on p. 55).
  - [41] C. W. Hirt and B. D. Nichols. “Volume of fluid (VOF) method for the dynamics of free boundaries”. In: *Journal of computational physics* 39.1 (1981), pp. 201–225 (cit. on p. 37).
  - [42] R. J. Hunt. “The History of the Industrial Gas Turbine”. In: *IDGTE, Morpeth, United Kingdom* (2011) (cit. on p. 1).

- [43] P. Jenny, B. Müller, and H. Thomann. “Correction of Conservative Euler Solvers for Gas Mixtures”. In: *J. Comput. Phys.* 132.1 (Mar. 1997), pp. 91–107 (cit. on p. 37).
- [44] E. Jouguet. “Sur la propagation des réactions chimiques dans les gaz”. In: *Journal des Mathématiques Pures et Appliquées, série 6* (1905), pp. 347–425 (cit. on p. 67).
- [45] S. Karni. “Multicomponent Flow Calculations By A Consistent Primitive Algorithm”. In: *Journal Of Computational Physics* 112.1 (1994), pp. 31–43 (cit. on p. 37).
- [46] R. Klein, K. R. Bates, and N. Nikiforakis. “Well-balanced compressible cut-cell simulation of atmospheric flow”. In: *Philosophical Transactions of the Royal Society of London A: Mathematical, Physical and Engineering Sciences* 367.1907 (2009), pp. 4559–4575 (cit. on p. 89).
- [47] S. H. Lam and D. A. Goussis. “The CSP method for simplifying kinetics”. In: *International Journal of Chemical Kinetics* 26.4 (1994), pp. 461–486 (cit. on p. 24).
- [48] L. D. Landau and E. M. Lifshitz. “Fluid mechanics, vol. 6”. In: *Course of Theoretical Physics* (1987), pp. 227–229 (cit. on pp. 8, 105).
- [49] L. D. Landau and E. M. Lifshitz. *Statistical Physics: V. 5: Course of Theoretical Physics*. Pergamon Press, 1969 (cit. on pp. 4, 105).
- [50] B. Larroutuou. “How to Preserve the Mass Fractions Positivity when Computing Compressible Multi-component Flows”. In: *Journal of computational physics* 95 (1991), pp. 59–84 (cit. on pp. 37, 49).
- [51] B. Larroutuou and L. Fezoui. “On The Equations Of Multicomponent Perfect Of Real-Gas Inviscid Flow”. In: *Lecture Notes In Mathematics* 1402 (1989), pp. 69–98 (cit. on pp. 37, 40).
- [52] J. H. Lee, R. Knystautas, and N. Yoshikawa. “Photochemical initiation of gaseous detonations”. In: *Acta Astronautica* 5.11 (1978), pp. 971–982 (cit. on p. 19).
- [53] R. J. LeVeque. *Finite volume methods for hyperbolic problems*. Vol. 31. Cambridge university press, 2002 (cit. on pp. 8, 39, 43, 50, 54, 59, 108).
- [54] P.-L. Lions. *Mathematical Topics in Fluid Mechanics: Volume 2: Compressible Models*. Vol. 2. Oxford University Press on Demand, 1998 (cit. on p. 8).
- [55] N. M. Marinov, C. K. Westbrook, and W. J. Pitz. “Detailed and global chemical kinetics model for Hydrogen”. In: *Transport phenomena in combustion* 1 (1996), p. 118 (cit. on p. 10).
- [56] R. I. McLachlan and G. R. W. Quispel. “Splitting methods”. In: *Acta Numerica* 11 (2002), pp. 341–434 (cit. on p. 56).
- [57] A. Meyer. “The Combustion Gas Turbine: Its History, Development, and Prospects”. In: *Proceedings of the Institution of Mechanical Engineers* 141.1 (1939), pp. 197–222 (cit. on p. 1).

- [58] J. von Neumann. “Theory of detonation waves. Progress Report to the National Defense Research Committee Div. B, OSRD-549,(April 1, 1942. PB 31090)”. In: *John von Neumann: Collected Works 1957* (1942) (cit. on p. 66).
- [59] J. R. Partington. *An advanced treatise on physical chemistry*. Vol. 3. Longmans, Green, 1949 (cit. on p. 105).
- [60] H. Pitsch. “Flamemaster: A C++ computer program for 0D combustion and 1D laminar flame calculations”. No dedicated peer-reviewed publication exists. URL: <http://www.itv.rwth-aachen.de/index.php?id=128> (cit. on pp. 22, 115).
- [61] J. F. Price. “Lagrangian and eulerian representations of fluid flow: Kinematics and the equations of motion”. In: *Woods Hole Oceanographic Institution, Woods Hole, MA 2543* (2006) (cit. on p. 13).
- [62] P. Rijke. “Notiz über eine neue Art, die in einer an beiden Enden offenen Röhre enthaltene Luft in Schwingungen zu versetzen”. In: *Annalen der Physik* 183.6 (1859), pp. 339–343 (cit. on p. 7).
- [63] P. L. Roe. “Approximate Riemann solvers, parameter vectors, and difference schemes”. In: *Journal of computational physics* 43.2 (1981), pp. 357–372 (cit. on p. 44).
- [64] G. D. Roy et al. “Pulse detonation propulsion: challenges, current status, and future perspective”. In: *Progress in Energy and Combustion Science* 30.6 (2004), pp. 545–672 (cit. on p. 5).
- [65] J. Z. S. Browne and J. E. Shepherd. “Numerical Solution Methods for Shock and Detonation Jump Conditions”. In: *GALCIT Report FM2006.006* (2008) (cit. on p. 67).
- [66] A. H. Shapiro. “The dynamics and thermodynamics of compressible fluid flow”. In: *New York: Ronald Press, 1953-54* 1 (1953) (cit. on p. 16).
- [67] G. P. Smith et al. “GRI-Mech 3.0”. In: (1999). URL: [http://www.me.berkeley.edu/gri\\_mech](http://www.me.berkeley.edu/gri_mech) (cit. on p. 68).
- [68] G. A. Sod. “A survey of several finite difference methods for systems of nonlinear hyperbolic conservation laws”. In: *Journal of computational physics* 27.1 (1978), pp. 1–31 (cit. on p. 58).
- [69] G. Strang. “On the Construction and Comparison of Difference Schemes”. In: *SIAM Journal on Numerical Analysis* 5.3 (1968), pp. 506–517 (cit. on p. 55).
- [70] E. Tadmor. “Numerical Viscosity And The Entropy Condition For Conservative Difference-Schemes”. In: *Mathematics Of Computation* 43.168 (1984), pp. 369–381 (cit. on p. 48).
- [71] E. F. Toro. *Riemann solvers and numerical methods for fluid dynamics: a practical introduction*. Springer Science & Business Media, 2009 (cit. on pp. 38, 42, 54, 62, 108).

- [72] B. Van Leer. “On the relation between the upwind-differencing schemes of Godunov, Engquist-Osher and Roe”. In: *SIAM Journal on Scientific and Statistical Computing* 5.1 (1984), pp. 1–20 (cit. on p. 54).
- [73] B. Van Leer. “Towards the ultimate conservative difference scheme”. In: *Journal of Computational Physics* 32.1 (1979), pp. 101–136 (cit. on pp. 38, 54).
- [74] B. Vanleer. “Flux-vector splitting for the 1990s”. In: *NASA, Lewis Research Center, Computational Fluid Dynamics Symposium on Aeropropulsion* (1991), pp. 203–214 (cit. on p. 48).
- [75] Y. Wada. *Approximate Riemann solvers: Improvement of the HLLEM scheme and its generalization for chemically reacting flows*. Tech. rep. TR-1189. National Aerospace Laboratory Computational Sciences Division, Dec. 1992 (cit. on p. 70).
- [76] S. Welch. *Quasi one-dimensional flow*. Lecture notes at University of Colorado, Denver. 2010 (cit. on p. 16).
- [77] P. Wesseling. *Principles of computational fluid dynamics*. Vol. 29. Springer Science & Business Media, 2009 (cit. on p. 13).
- [78] F. A. Williams. *Combustion Theory: The Fundamental Theory of Chemically Reacting Flow Systems*. Combustion science and engineering series. Perseus Books Group, 1985 (cit. on p. 5).
- [79] S. Wolff, P. Berndt, and R. King. “State estimation for homogeneous 1-D Euler Equation by Unscented Kalman Filtering”. In: *ASME 2015 Dynamic Systems and Control Conference* 2 (2015), (cit. on p. 71).
- [80] H. Yoshida. “Construction of higher order symplectic integrators”. In: *Physics Letters A* 150.5 (1990), pp. 262–268 (cit. on p. 55).
- [81] S. Yungster, K. Radhakrishnan, and K. Breisacher. “Computational study of NO<sub>x</sub> formation in hydrogen-fuelled pulse detonation engines”. In: *Combustion Theory and Modelling* 10.6 (2006), pp. 981–1002 (cit. on pp. 68, 69).
- [82] Y. B. Zel'dovich. “On the theory of the propagation of detonations on gaseous system”. In: *Zh. Eksp. Teor. Fiz.* 10 (1940), pp. 542–568 (cit. on p. 66).





## Danksagung

Die vorliegende Arbeit entstand während meiner Zeit als wissenschaftlicher Mitarbeiter am Fachbereich Mathematik & Informatik an der Freien Universität Berlin im Rahmen des von der Deutschen Forschungsgemeinschaft geförderten Sonderforschungsbereiches 1029 „TurbIn — Signifikante Wirkungsgradsteigerung durch gezielte, interagierende Verbrennungs- und Strömungsinstationaritäten in Gasturbinen“.

Zuallererst einmal möchte ich an dieser Stelle meinem Doktorvater Prof. Dr.-Ing. Rupert Klein danken. Erst durch Ihn bin ich überhaupt auf den Themenkomplex Gasdynamik und Verbrennung aufmerksam geworden, den ich in den letzten Jahren mit einem enormen Maß an Freiheit und Selbstständigkeit durchdringen durfte. Dass diese Freiheit nie in Orientierungslosigkeit ausuferte, verdanke ich einer außerordentlich guten Betreuung und seiner Fähigkeit, den Zeitpunkt für kleine Stupser in die richtige Richtung perfekt wählen zu können. Dass es das SEC-Projekt in dieser Form überhaupt gibt, verdanke ich ihm und Prof. Dr.-Ing. C. Oliver Paschereit. Auch letzterem bin ich zu großem Dank verpflichtet. An seinem Heimatinstutut, dem Institut für Strömungsmechanik und Technische Akustik der TU Berlin, habe ich mich immer willkommen gefühlt. Das liegt mit Sicherheit nicht zuletzt an seinen großartigen Mitarbeitern, die mich vom ersten Tag an herzlich bei sich aufgenommen haben.

Allen voran muss ich hier Bernhard Bobusch nennen, der mit mir zusammen in den ersten Jahren das Teilprojekt A03 des SFBs bearbeitet hat. Ich habe ihn nicht nur als außerordentlich guten Wissenschaftler, sondern auch als mindestens ebenso außerordentlich lieben Menschen kennenlernen dürfen, mit dem mich Unmengen an tollen Erinnerungen auch jenseits der Arbeit verbinden. Joshua Gray und Oliver Krüger vom selben Institut muss ich das gleiche Lob aussprechen. Ihr habt mir die Zeit während meiner Promotion wahnsinnig bereichert!

Herr Prof. Dr.-Ing. Rudibert King hat als Sprecher des SFBs das Projekt überhaupt erst in dieser Form ermöglicht. Vielen Dank dafür! In einem Sonderforschungsbereich arbeiten zu dürfen war für mich ein Privileg, und die mit ihm einhergehende Interdisziplinarität eine große intellektuelle Bereicherung. Sonja Hoßbach und Nikolas Losse haben dabei durch ihren steten Einsatz dafür gesorgt, dass die Arbeit im SFB auch zwischenmenschlich eine großartige Erfahrung war. Vielen Dank Euch beiden! Auch allen anderen Kollegen, die bei den diversen Summer Schools und Konferenzen dabei waren, bin ich zu großem Dank für die tolle Zeit verpflichtet.

An der Freien Universität möchte ich meiner Arbeitsgruppe für die schöne Zeit danken, und allen voran meinem langjährigen Büronachbarn Mark Schlutow, mit dem ich zahlreiche spannende Diskussionen führen durfte; nicht nur direkt über die eigene Arbeit, sondern eigentlich über alles, was einen als wissenschaftlich orientierter Mensch so interessieren kann. Auch Feliks Nüske gilt (mal wieder) großer Dank — wir gehen zwar seit der Doktorarbeit verschiedene fachliche Wege, tauschen uns aber immer noch jede Woche beim Mittagessen über unsere Forschung aus. Mit jemandem, der ein wenig Abstand zur eigenen Arbeit hat, über selbige zu reden, war unglaublich bereichernd.

Es ist schierer Wahnsinn, wie viele tolle, intelligente, freundliche und liebe Menschen ich in meiner Zeit als Doktorand kennenlernen durfte, und wie viele Freundschaften

dabei entstanden sind. Dieses Glück kann ich auch heute noch nicht immer wirklich fassen. Allen, die ich schon erwähnt habe, und allen, die ich hier vergessen habe, an dieser Stelle nochmals: Danke!

Meiner Promotionskommission, der neben den beiden Professoren Klein und Paschereit noch Prof. Dr. Volker John und Dr. Thomas von Larcher angehörten, herzlichen Dank, dass Sie sich die Mühe gemacht haben, das Promotionsverfahren zu betreuen und durchzuführen.

Meinen Eltern und meiner Freundin Mitra Pasche bin ich zu größerem Dank verpflichtet, als ich hier zu Papier bringen könnte. Ganz speziell möchte ich an dieser Stelle deswegen Danke dafür sagen, wie viel Unterstützung Ihr mir in den letzten Monaten vor der Abgabe und bis nach der Verteidigung der Arbeit habt zukommen lassen, und wie sehr Ihr mir in dieser Zeit den Rücken freigehalten habt.

Phillip Berndt

Berlin, im Dezember 2016

## Zusammenfassung

Die stoßfreie, druckerhöhende Verbrennung (shockless explosion combustion, SEC) ist ein alternativer Betriebsmodus für Gasturbinen. Sie stellt eine Annäherung an eine Gleichraumverbrennung mit Aussicht auf eine hohe Effizienzsteigerung dar. Besonders macht sie dabei der aktive Einsatz schwacher Detonationen: Der Prozess erzeugt eine Schichtung von Luft und Treibstoff, die nach einer Weile sequentiell selbstzündet. Im Gegensatz zu den starken Stoßwellen, die eine Detonation mit sich bringen würde, erzeugt die folgende Verbrennung glatte Druckwellen. In der SEC wird die durch diese Wellen erzeugte Akustik zum Spülen und Nachladen des Brennrohrs verwendet.

Diese Arbeit dokumentiert eine erste, theoretische Untersuchung des Prozesses. Dabei wird ein Modell sowie dazugehörige numerische Verfahren für seine Simulation vorgestellt. Die Arbeit besteht aus drei Teilen:

Der erste Teil beschäftigt sich mit Treibstoffen für den SEC Prozess. Eine SEC erfordert spezielle Treibstoffe, die die Eigenschaft haben, eine im wesentlichen temperaturunabhängige Zündverzugszeit zu besitzen. Als Zündverzugszeit bezeichnet man dabei die Zeit, die zwischen der Erzeugung eines Treibstoff/Luft-Gemisches bei relativ hohen Temperaturen und seiner Selbstzündung vergeht. Treibstoffe mit dieser Eigenschaft besitzen eine komplexe Reaktionskinetik, die sich mit traditionellen Verfahren nur mit hochdimensionalen Modellen beschreiben lässt. Solche Modelle sind für qualitative Strömungssimulationen ungeeignet. In dieser Arbeit wird daher ein generisches, niedrigdimensionales Modell für derartige Treibstoffe eingeführt. Das Modell erreicht die Niedrigdimensionalität dabei, indem der Treibstoff auf das geforderte Verhalten im Fall einer funktionierenden SEC reduziert wird. Weiterhin werden Ergebnisse rund um die Modellreduktion und Optimierung eines für die SEC vorgeschlagenen Treibstoffes vorgestellt.

Der zweite Teil der Arbeit entwickelt numerische Verfahren zur Simulation einer SEC. Zur Beschreibung des strömungsmechanischen Verhaltens des Systems werden dabei die reaktiven Eulergleichungen verwendet. Da das System verschiedensten Temperaturen ausgesetzt ist, wird die ideale Gasgleichung mit temperaturabhängigen Wärmekapazitäten verwendet. Um dieses Gleichungssystem mit einem Finite-Volumen-Verfahren lösen zu können, wird zunächst die Lösung des Riemannproblems für diesen Fall diskutiert. Daraufhin führt die Arbeit die nötigen Erweiterungen für den HLLEM-Löser ein, um mit allgemeinen idealen Gasgemischen umgehen zu können. Insbesondere wird die Positivität des sich ergebenden Verfahrens bewiesen. Zusätzlich diskutiert der Teil der Arbeit das bekannte Problem von Druckschwankungen an Kontaktunstetigkeiten und stellt eine Verbindung zu einem physikalischen Phänomen her.

Der dritte Teil nutzt das entwickelte numerische Verfahren zusammen mit den Kinetikmodellen, um die SEC zu simulieren. Es wird zunächst gezeigt, dass eine SEC prinzipiell machbar ist. Durch weitere Simulationen gelangt der Teil dann zu Abschätzungen, die für die Suche nach einem SEC-Treibstoff und der experimentellen Realisierung des Prozesses von Bedeutung sind. Abschließend zeigen einige Simulationen mögliche Erweiterungen des Konzeptes auf.



## Abstract

The shockless explosion combustion (SEC) is a thermodynamic cycle for pressure gain combustion in gas turbines. It approximates constant volume combustion and promises a huge efficiency gain over traditional operation. Its use of weak detonations makes it unique among other processes approximating constant volume combustion: In the process, a stratification of fuel/air is created in a combustion tube and brought to sequential auto-ignition. The resulting combustion yields smooth pressure waves, in contrast to the strong shock waves in alternatives based on detonations. The SEC incorporates these waves into a clever recharging concept that utilizes the acoustics within the tube to create the current required for flushing and refilling the tube.

This thesis documents a first theoretical investigation of the process. In particular, it establishes models for the process and methods for their numerical simulation. It consists of three major parts:

The first one is concerned with fuels for the SEC process. A SEC requires specialized fuels with the property that their auto-ignition delay time, that is, the time that it takes for the fuel to auto-ignite at high temperatures, is largely independent of temperature. Such fuels have complex chemistry, and traditional methods from chemical kinetics lead to high dimensional mathematical descriptions that are expensive to calculate in numerical simulations. This thesis introduces a low-dimensional generic model for such fuels. The model achieves the low dimensionality by stripping the model fuel from any off-design behaviour: Rather than to describe the actual chemistry, it only describes the fuel's behaviour in the context of a working SEC. Further results concerning SEC fuels are the model reduction for and optimization of an actual prospective SEC fuel.

The second part is concerned with the creation of a numerical simulation for the process. The reactive Euler equations are used to describe the fluid dynamics of the system, and since a variety of temperatures is involved, the ideal gas equation of state with temperature-dependent heat capacities is used. To be able to solve this equation system using a finite volume framework, the part discusses the solution of the Riemann problem in this setting and extends the HLLEM approximate Riemann solver accordingly. In particular, it is proven that the resulting solver has the positivity property. In addition, the well-known issue of spurious pressure oscillations close to contact discontinuities is discussed and linked to a physical phenomenon.

The third part puts numerical code and kinetics models together to perform simulations of the process. It is shown that a SEC is viable, and several estimates relevant to the search for suitable fuel blends and the process's experimental realization are obtained. Simulations also shed a light on possible extensions of the concept and future work.

